MINIATURIZED ELECTRONIC SENSORS AND ACTUATORS FOR HEALTHCARE AND ENVIRONMENTAL MONITORING

By

AZAM GHOLIZADEH

A dissertation submitted to the

School of Graduate Studies

Rutgers, The State University of New Jersey

In partial fulfillment of the requirements

For the degree of

Doctor of Philosophy

Graduate Program in Electrical and Computer Engineering

Written under the direction of

Dr. Mehdi Javanmard

And approved by

_____

_____

_____

_____

_____

New Brunswick, New Jersey
January 2019

ABSTRACT OF THE DISSERTATION

Miniaturized Electronic Sensors and Actuators for Healthcare and Environmental Monitoring

By AZAM GHOLIZADEH

Dissertation Director:

Dr. Mehdi Javanmard

Lab on a chip is an emerging field that has the potential to fully automate small-scale biological experiments. To realize this aim, both analytical and fluid control components need to become fully miniaturized. In addition to this, high sensitivity sensors are needed to compensate for the reduction in target analyte. In this thesis, we address two key challenges in Micro Total Analysis Systems: The fabrication and characterization of 1) Highly sensitive sensors and 2) Low power magnetic based valves for microfluidic applications in lab-on-a-chip systems utilized for portable analytical methods for point-of-care healthcare applications and point-of-use environmental monitoring.

For health monitoring we focus on development of a non-invasive approach for measuring indicators of inflammation and oxidative stress in the respiratory tract by quantifying a biomarker in exhaled breath condensate. We utilize the unique properties of reduced graphene oxide to electrochemically detect nitrite content in EBC samples. Nitrite is as one of promising biomarkers of inflammation in the respiratory tract.

For environmental applications, lead contamination poses a serious public health problem considering it is one of the most dominant heavy metal present in the environment. Our sensor is capable of detecting lead in freshwater sediment samples. A sample-to-answer platform capable of on-chip sediment digestion and purification in conjunction with electrochemical quantification of lead ions is presented.

Miniaturized fluidic valves with ultra-compact instrumentation footprint are necessary to realize flow control in microfluidic channels. Here we use an electronically controlled magnetic force combined with an elastomeric membrane to fabricate micro-valves. We evaluated geometrical effects on the performance of valves using both simulation and experimental approaches with permanent magnets. Zero static power switchable valves are demonstrated using electropermanent magnets enabling use in hand-held devices.

ACKNOWLEDGMENTS

First, I would like to convey my gratefulness to my advisor, Dr. Mehdi Javanmard, for providing me the opportunity to be a member in Nanobioelectronic lab. Completing of my thesis was impossible without his patient guidance and constant encouragement.

Also, I would like to thank my committee members, Dr. Yicheng Lu, Dr. Manish Chhowalla, Dr. Leonard Feldman and Dr. Laura Fabris for their support, advice, and constructive suggestions on my thesis.

I would also like to provide a special thank you to Dr. Chhowalla, Dr. Fabris, Dr. Garfunkel, Dr. Andrew Gow, Dr. Miskewitz, Dr. Maher and Microelectronics Research Laboratory (MERL) Faculties and staffs for providing use of their equipment and materials for my research.

I am grateful for having a chance to work with all the members in NanoBioelectronic Lab. I want to thank Pengfei Xie, Sakshi Sardar and Tuan Le for their help on magnetic based microfluidic valve project and taking SEM and AFM images.

I would also thank you Dr. Damien Voiry for his help on making graphene oxide thin film and Dr. Siamak Abbaslou for his help on making electropermanent magnet circuit.

I am grateful to all electrical engineering department helpful staffs, John Scafidi, Steve Orbine, Arletta Hoscillowicz, Tea Akins, Christopher Reid, Christy Lafferty and Azam Kalantari from CAIT for their constant help.

Last but not the least, I would like to express the deepest appreciation to my parents, my sister and brother and my beloved friends who provide me constant encouragement for all through this time.

TABLE OF CONTENTS

LIST OF FIGURES

LIST OF TABLES

Chapter 1: Introduction

This chapter gives an overview of the research proposal concepts and problem statements for healthcare, environmental developed sensor and magnetic microfluidics valve. It briefly explains the background of each part of project and clarifies why these issues are worthy to attention nowadays.

1.1. Healthcare application of graphene oxide sensor

Biomarkers have enormous potential utility in assessing chronic inflammation, especially in asthma, which affects ~300 million people worldwide. Asthma, which is characterized by variable airway inflammation and airflow obstruction, is an increasingly important global health problem. In the United States alone, ~ 17.7 million adults and 6.3 million children were diagnosed with asthma in 2014 [1]. Furthermore, the cost of asthma care in the United States was estimated to be $56 billion in 2007. The currently available non-invasive methods for diagnosing and monitoring asthma, i.e., spirometry and the measurement of exhaled nitric oxide, are limited by low sensitivity and the need for expensive and bulky equipment. Moreover, existing tests have a limited ability to characterize the nature and extent of underlying airway inflammation, which is widely variable between individuals [2]. Measurement of biomarkers in exhaled breath condensate (EBC) can contribute to the molecular phenotyping of asthma, thus enabling targeted treatment and more effective disease management. Given the large and growing burden of asthma, there is an urgent need for improved, minimally invasive methods for the molecular diagnosis and monitoring of asthma.

The use of biomarkers in EBC may help to overcome the difficulties associated with obtaining airway tissue and bronchoalveolar lavage samples that have significantly hampered the study of naturally occurring exacerbations of asthma. EBC contains droplets of airway lining fluid (ALF) that are exhaled during normal tidal breathing. In addition to condensed gas-phase compounds, EBC contains non-volatile compounds that originate from ALF, including hydrogen peroxide, nitrite and nitrate, as well as larger molecules such as eicosanoids, proteins, and even nucleic acids [3]. The ability to non-invasively characterize airway tissue by repeated measurements of biomarkers in EBC would be invaluable for studying the time-course of dynamic inflammatory pathways that are involved in asthma exacerbation. Ultimately, EBC biomarkers may contribute to the assessment of different asthma phenotypes and the development of individualized rational approaches to asthma management at the point of care [4].

Recent studies have shown the promise of EBC nitrite for use as a biomarker of both oxidative stress and inflammation in asthma (figure 1-1). The primary source of nitrite in the respiratory tract is nitric oxide (NO), which is produced from L-arginine by nitric oxide synthase. In aqueous solution, NO reacts rapidly with reactive oxygen species (ROS) to form more stable nitrogen oxides, such as nitrite (NO_2^-) and nitrate (NO^-_3) [5]. Increased levels of NO are associated with inflammatory disease states such as asthma, COPD [6], and cystic fibrosis [7]. The increased level of exhaled NO in asthma has been suggested to be due to an increased expression of inducible NO synthase (iNOS) in bronchial epithelium [8]. Given the relative stability of nitrite in EBC and its promise as a biomarker of chronic respiratory inflammation, we developed a miniaturized probe-free/label-free sensor for the detection of nitrite in EBC.

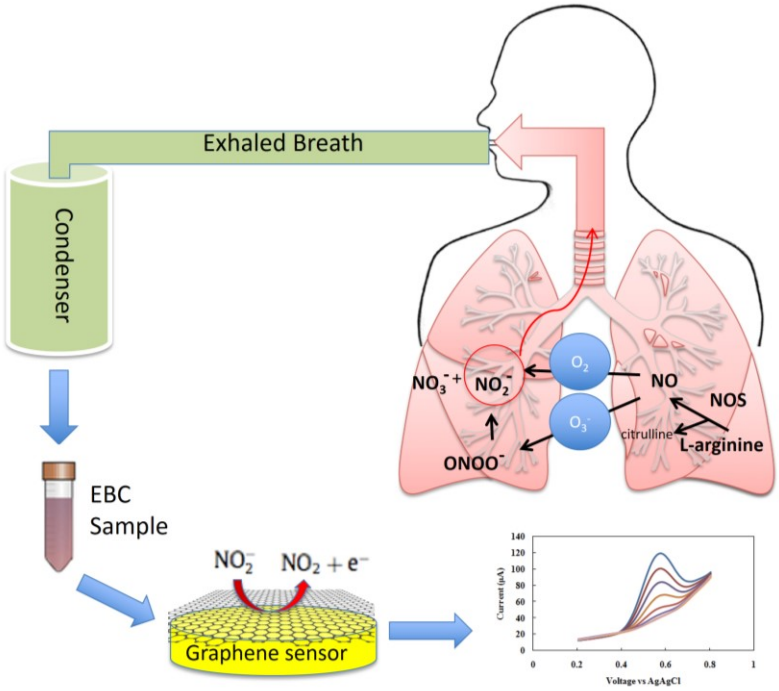

Figure 1-1. An exhaled breath condensate (EBC) sample is collected, and nitrite content is measured electrochemically [9].

Nitrite is typically detected through one of several spectro-photometric methods (Griess reaction) involving fluorimetry, chemiluminescence, or ion chromatography [10-12]. The detection limit of fluorimetric methods is 0.1 µM. Chemiluminescence has a lower detection limit (in the nM range). Nitrite concentrations in EBC are in the µM range and are compatible with these detection limits. However, despite the low detection limit provided by these methods, EBC samples are usually pretreated to induce the appropriate reaction and/or to eliminate interfering compounds, such as chlorine [13]. The benefit of using electrochemical methods is that pretreatment steps are not required; more importantly, both the sensor and the instrumentation readout can be readily miniaturized, thus enabling the development of point-of-care diagnostics and even real-time wearable health-monitoring devices. The other strong benefit of using electrochemical methods is that they can be used to detect nitrite content at a specific potential of 0.7 V in real time

without interference from other compounds in the EBC matrix. The drawbacks, however, are that these methods often do not offer the same detection limit as those provided by optical methods, and standard electrochemical cells require sample volumes of several milliliters.

The electrochemical detection of nitrite is based on either the oxidation or reduction of nitrite [14]. Nitrite oxidation-based methods with a final product of NO_3 are usually preferred because the presence of interfering molecules (such as oxygen) during reduction can be avoided [15]. However, an oxidation reaction as the basis for detecting nitrite requires a high over-potential [16]; thus, in recent years, many attempts have been made to develop novel electrode materials [17-19]. Among possible novel materials, graphene-based electrodes have been widely used due to their low over-potentials, low electron transfer resistance, small residue currents, wide potential window, excellent chemical stability and potential for chemical functionalization. Graphene has previously been explored to detect a wide range of chemical and biological species [20-22].

Here, we use graphene-based electrodes to detect nitrite in EBC. A nitrite detector is fabricated using screen- printed electrodes that are modified with electrochemically reduced graphene oxide. Another limiting factor for graphene-based electrochemical sensors is that simple drop cast methods are used to deposit graphene oxide on a metal electrode film; this method can result in device-to-device variation due to the agglomeration of graphene oxide flakes. To resolve this issue, we used a modified drop cast method that results in thinner and precisely patterned rGO electrodes. We also fabricated a micro-electrochemical cell using a polydimethyl siloxane (PDMS) membrane to enable voltammetric measurements of very small sample volumes, which is necessary

for analyzing EBC samples, where limited sample volumes are available. To the best of our knowledge, this represents the first electrochemical sensor that can directly measure nitrite content in clinical EBC samples with submicromolar detection limits.

This sensor can easily be portable however, needs further optimization to achieve detection in the nano-molar range. Moreover, standardization of new methods for clinical application is needed. Especially in EBC samples, the source of variation can be related to the technique of sample collection, processing, and analysis. The aim of presented work is two-fold. We seek to improve the sensitivity of analysis and study stability of nitrite during storage. Moreover, as with electrical detection, the conductivity and nature of matrix are very important, these parameters have been studied with variation of electrolytes and Electrochemical impedance spectroscopy.

1.2. Environmental application of graphene oxide sensor

One of the most dominant heavy metals present in the environment is lead as it is widely used in building materials, lead paints, and even lead-acid batteries. As a result of this overabundance in the environment, particularly in natural water sources and even drinking water, lead poisoning has resulted in many public health epidemics. Lead and other toxic metals that end up in natural water sources can often settle down to the bottom into the sediment. Contaminated sediment can get resuspended into natural water sources due to storms and transit of boats and vessels. The high concentration of lead in sediment (reported in the range of mg/kg [23]) when released into the water, poses risks to aquatic organisms and thus poses a serious public health problem. Based on reports, lead can

damage the human nervous (especially children), respiratory, and reproductive systems [24]. Hence, the ability to rapidly screen sediment samples for lead is necessary to identify hot-spots of contaminated areas where remediation is necessary, to thus minimize the risk of re-suspension into natural water sources. To meet this requirement, there is a need for automated, portable, ultra-compact sensing devices capable of qualitatively identifying toxic metals directly in complex environmental samples without the need for manhandling and sample preparation. Due to the detrimental health risks resulting from lead contamination, a variety of measurement methods have been developed. These methods include atomic absorption spectroscopy [25-28], inductive coupled plasma mass spectroscopy [29, 30], various optical [31-33] and electrochemical methods, which are primarily based on ion selective electrodes [34, 35] and stripping voltammetry [36-39]. Among these, because of high speed, high sensitivity, and portability, electrochemical-stripping voltammetry is a promising method for tools capable of field measurements. Stripping voltammetry works well in purified buffers, however, to the best of our knowledge, to date, there have been no reports of electrochemical platforms capable of direct measurement of lead in sediment sample.

Electrochemical based sensors utilize a variety of electrode surface modifications for increasing sensitivity of lead detection. One example involves the reaction between tin and bismuth with lead and incorporation of these materials on the surface of the electrodes [22, 40-42]. Also, a variety of other metal nanoparticles have been used, with the aim of increasing the surface area [43-46]. Other methods are based on using DNA enzymes [47, 48]. Additionally, graphene based nanomaterials due to their extraordinary electronic transport properties, large surface area, higher cathodic window thus avoiding reduction of

hydrogen, and high electrocatalytic activities are another potential class of materials for electrode surface capable of sensitive lead detection [49-52]. Among them, graphene oxide, prepared through extensive chemical exfoliation of graphite flakes, has oxygen containing functional groups such as hydroxy, carboxy, epoxy, ether, diol and ketone, which are active sites for adsorbing heavy metals such as lead [22, 53].

Various methods allow for relatively easy deposition of graphene oxide (GO) thin films on top of electrode surfaces including drop casting [49-51, 54, 55], dip coating [56], Langmuir-Blodgett based deposition [57, 58], transfer via vacuum filtration, [59, 60] and spin coating [61-63]. The method used for deposition of GO is very important to control surface morphology, film uniformity, thickness and surface coverage. Among these methods, dip coating and drop casting often result in non-uniform deposition due to aggregation of GO sheets. Also drop casting GO suspension usually results in weak adhesion to electrode substrate. The rapid evaporation of the solvent during spin coating allows a more uniform surface with minimal wrinkling and increases the adhesion between the GO thin film and the electrode surface, which is critical during electrochemical reduction of GO.

Because of the ease and low cost for manufacturing, screen printed electrodes (SPE) have great utility as a disposable device. SPEs can be used for point-of-use testing in various applications such as industrial process monitoring, environmental monitoring, and food testing. Screen-printed electrodes combined with stripping voltammetry provide a promising solution for detection of heavy metals such as lead [64-66]. Various lead sensors have been developed using SPEs. One example is disposable bismuth oxide modified SPE for detection of lead in the range of 20-300 ppb with a detection limit of 8 ppb [67]. In

other works, SPEs modified by gold films displayed very highly linear behavior in the lead concentration range of 2-16 ppb with a detection limit of 0.5 ppb [68].

The key challenge to utilizing electrochemical methods for detecting heavy metals in complex matrices such as sediment, food, and soil at point-of-use is the requirement to perform a separate pretreatment step for extraction of ions and purification of sample [69-71]. For lead, the ion extraction step is essential to convert all various chemical forms of lead to Pb^{2+} so that they can participate in the electrochemical reaction.

In this work, we present an ultra-compact sediment pretreatment module combined with a highly sensitive electrochemical graphene oxide sensor to detect lead in untreated sediment samples obtained directly from the environment (Figure 1-2). Our sediment pre-treatment module consists of a cellulose sponge, which serves as a membrane between the sediment and the active site of the sensor. Sponges have demonstrated significant ability to adsorb contamination, [72] thus making them a suitable choice of material for the porous membrane. The porous membrane adsorbs contamination of sediment preventing direct contact between solid sediment and the active graphene oxide site. Moreover, lead ions easily penetrate through the cellulose sponge membrane and thus pure solution reaches the graphene oxide surface. An additional benefit to this approach is that this set up minimizes the required acidic pretreatment to microliter levels.

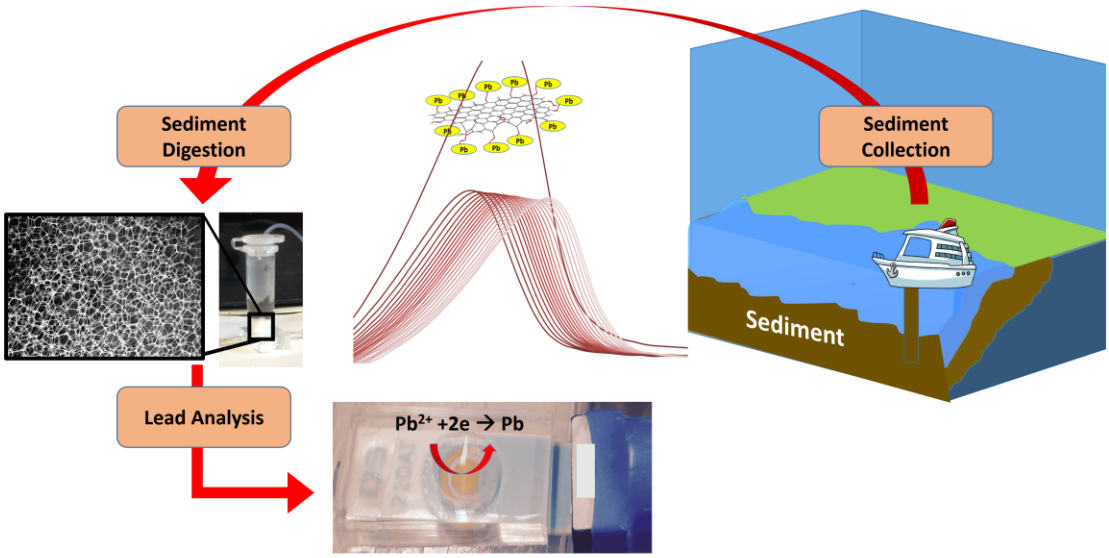

Figure 1-2. Schematic of sediment sample collection and measurement of lead

Moreover, we selectively spin-coated GO uniformly onto a screen printed gold working electrode and investigated the performance of the sensor over a wide range of parameters to optimize the performance. Gold screen-printed electrodes are high in conductivity and exhibit excellent performance of stripping voltammetry and are thus chosen as the working electrode for deposition of GO [73-75]. The surface morphology and chemical characterization of the GO film was done using scanning electron microscopy (SEM), atomic force microscopy (AFM) and Raman Spectroscopy. The analytical parameters affecting the sensor performance and the thin film fabrication were studied in terms of concentration of GO solution during spin coating, the effect of GO reduction, the supporting electrolyte, square wave anodic stripping voltammetry (SWASV) parameters such as deposition time, frequency, and pulse height. The reliability of the electrode in response to high concentrations of lead was also investigated to ensure the capacity of lead adsorption on the surface of the electrode. Furthermore, the effect of water extracted from

sediment on the supporting electrolyte was investigated both with and without adding acetate buffer solution in the range of 0 ppb to 20 ppm lead standard. This was then used to quantify the amount of lead present in digested sediment samples collected from the environment.

1.3. Magnetic based microfluidic valves

Microfluidic technology has shown significant promise in a wide range of applications including low volume high precision chemical and material synthesis platforms [76, 77], diagnostic devices [78, 79], nucleic acid amplification [80] cell sorting, and also culturing [81]. To fulfill the demands of these wide ranging applications, integrated solutions for dynamic fluidic control through micro-channels is required. The most important fluid handling components to enable fully miniaturized Micro-Total Analysis Systems (MicroTAS) are on-chip integrated valves, pumps, and mixers. In particular, the ability to reversibly open and close specific channels rapidly is an essential requirement for a wide range of analytical platforms. Integrated on-chip valves in microfluidic systems are typically categorized as passive [82, 83] and active valves. Active valves need external forces for operation. In the past few decades various active valve solutions using pneumatic [84], magnetic [85], electrostatic [86] and photonic actuation [87], hydrogel swelling [88], the movement of ferrofluids [89] and even sharp-memory alloy thermal response [90] have been reported. Among of them, the pneumatic valves developed by Unger and coworkers [91] based on soft lithography have emerged as the most widely used solution due to their versatility, ease of fabrication, high speed, and small size. Fabrication of numerous large-scale integrated fluidic systems has been possible with these kinds of valves. The difficulty,

however, in using pneumatic valves for realizing portable and even wearable fluidic analysis systems stems from the need for large numbers of tubing inserted in the channel inlets and the computer-based pneumatic actuators and pressure control system required, which makes the full system large and bulky. Thus, numerous efforts have been underway to realize valve solutions, not only with micro-scale valve geometries, but also micro-scale actuators as well, thus enabling ultra-compact Micro-Total Analysis Systems. This includes electrostatic and piezoelectric actuated valves requiring large actuation voltages [92, 93].

Among the wide variety of different micro-scale actuation mechanisms, magnetic actuation has advantages over other methods. In particular, it has been shown to produce large forces (> μN) capable of producing large displacements (100s of μm) [94]. Various magnetic micro-valves have been presented in the literature utilizing a number of magnetic materials to achieve actuation. Among the first embodiments was the use of electroplated soft magnetic materials (e.g. permalloy/NiFe). For example, a silicon-based microvalve with a permalloy-coated membrane was presented, consisting of a 7μm-thick Permalloy film on a 17μm-thick silicon membrane, capable of being deflected 23 μm via the device's integrated inductors. However, there are drawbacks for magnetic microstructures. As an example, it is not possible to generate locally restricted high magnetic field flux density inside these structures [95] magnetic hydrogels and ferrofluids are use to tackle this problem. Various groups have also suggested using magnetically modified elastomeric materials for fabrication of microfluidic valves [96]. As a result, quite a bit of effort has been undergone in obtaining suitable nanocomposite of PDMS and magnetic particle for actuation purposes [97-99]. Aside from the advantages of these composites, there are some

drawbacks for their use as actuating membrane. As an example, the synthesis of a uniform magnetic particle elastomer is difficult. Magnetic particles also cause changes in the mechanical properties of PDMS, which can vary from sample to sample so achieving consistently reliable valves from device to device is difficult. Also one cannot load magnetic particles into the PDMS beyond its solubility, which places a limit on magnetic permeability of the membrane. Thus, in most cases millimeter sized valves are required to get sufficient deformation to fully close a fluidic channel, thus large-scale integration is not feasible. Another drawback of these composites results from its optical properties, thus making the full channel opaque, making optical imaging difficult.

Magnetically actuated valves based on dispersion of nanoparticles on N-isopropylacrylamide hydrogel has also been reported but in spite of rapid on-off switching times, it has relatively large dimensions and thus has a sluggish valve response due to the cool down time of hydrogels. Ferrofluids have also been used for fabrication of microvalves. Most ferrofluid-based designs implement the ferrofluid in contact with the liquid in the channel, and thus the two liquids must be immiscible [89]. Use of a rigid iron plate in combination with PDMS membranes was reported [96, 100], however they are not suitable for miniaturization, and because of their inflexibility they can not close valves completely in low flow rates.

In this work, we present the use of magnetorheological (MR) fluids micropatterned on top of a PDMS membrane. The magnetorheological fluid is a suspension of microparticles in a carrier fluid on top layer of thin deformable PDMS layer. Because of the size of these particles, they cover and adhere to the membrane and also because they are suspended in liquid, they can rapidly become re-oriented in presence of a magnetic field and apply a

strong force to the membrane thus deforming it, closing the microfluidic channel directly beneath it. The key advantage of this approach is that the magnetic permeability of the MR fluid is significantly higher compared to magnetically doped PDMS membranes, thus significantly higher deformation can be achieved, allowing for smaller valves to be fabricated, thus making this approach more suitable for large scale biomicrofluidic integration. The other advantage of this approach is the cost effectiveness and also general compatibility with widely used soft-lithography processes for microfluidic channel fabrication.

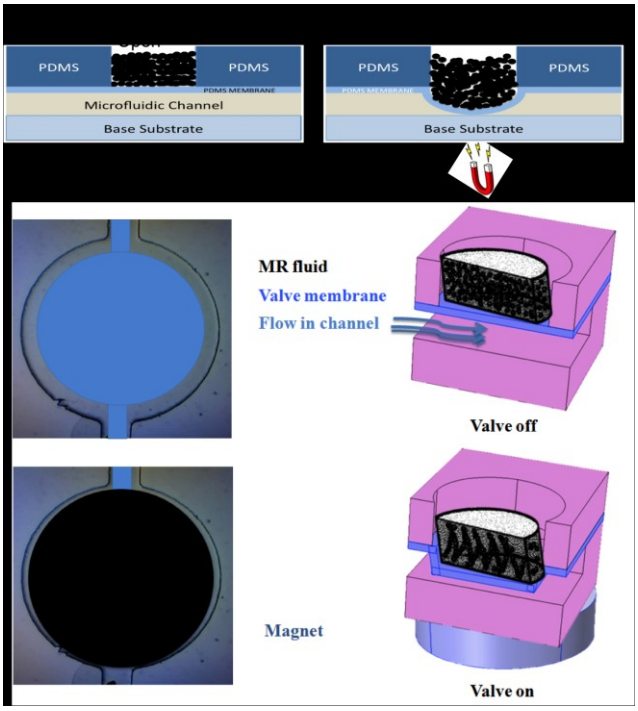

Figure 1-3. Schematic of the concept of MR fluid integrated with elastomeric PDMS membrane valves with permanent magnet. Application of magnet applies force on MR fluid and it cause deformation of thin layer of PDMS that can close the channel in push down method [101].

Figure 1-3 shows the basic concept of the MR fluid integrated with a PDMS membrane microfluidic valve. We systematically studied, both theoretically and experimentally,

various magnetic valve geometries and dimensions and compared the performance in terms of on-off cycle, response time, ability to close micro-channels, and their ability to withstand channel pressure.

For permanent magnet valve, the external motor is needed to move magnet. In addition, it is too large to create localized actuation and lack on-demand switching capability. For electrically actuated valves, such as electrostatic, piezoelectric, high voltage are usually required in order to generate enough actuation force [102]. This high voltage creates continuously large amount of heat, which can damage the device and biological samples. In electropermanent valves, as the coil dimension decreases, the resistance of the wires increases and produces significant joule heating, due to the needed of large continuous current to maintain the magnetic field.

Alternative magnetic force that provides localized actuation, stronger magnetic field and requires short current pulse to activate, is electropermanent magnet. The use of EPM to actuate the valve, allows both the strong magnetic field of permanent magnets and the ability to digitally control electromagnetic valves [103], all while maintaining low power consumption necessary for on-demand control of fluidic devices. The common application of EMPs are in industrial applications [104]. Recently, smaller versions of them provide several new applications including micromotors, programmable matter, and reconfigurable smartphones [105]. In addition, EPM actuator for droplet ferro-microfluidics was developed to sort droplets in continuous flow of microfluidic design [106]. In other work, by using supercapacitor energy buffer, wirelessly controlled electropermanent magnet microactuator was introduced that helps to integrate the control circuit platform of EPMs [107].

In the next study, we present electropermanent magnetic actuated elastomeric membrane based valve designed to store reagents and control fluid in wide-used PDMS based microfluidic systems. In this design a short current pulse switches magnetic field in microsecond time scale and the deformation of membrane actuates the valve. We assembled EPMs and characterized their magnetic behavior in different electrical condition. To demonstrate EMP as actuator for microfluidic channels, we have fabricated and tested simple and Y-shapes channels that can serve as building block of integrated multiple channels microTAS systems. The mechanism of opening and closing of valve was investigated in different flow conditions. In addition, we compared the behavior of EMP based valve with permanent magnetic one in different range of flow rates. To the best of our knowledge this is the first use of EMP to fabricate valves inside the PDMS based microfluidic channels.

The advantage of this method is, with applying negative current pulse for long period of time magnetic field can be canceled so it is highly energy efficient. As the main limitation in magnetic based valves, is magnetic force diminish exponentially with distance, in here with using micrometer thickness substrate membrane instead of glass, we could minimize the distance between EPM and elastomeric membrane. This low power, easy operated valve is suitable for long term reservoir of reagents in complex biochemical reactions inside the microfluidic systems. In addition, because of fast rate of magnetic switching, with applying square wave form and controlling its frequency, it simply can convert to micro-pump that is ongoing in our group. In distinction of existing magnetic microfluidic valves, using permanent magnet that cannot easily turn off and electromagnetic based ones which needs continuous electrical power supply, this design can actuate between ON and OFF

status with applying very short current pulse. This design, therefore, has the potential to automate the design of point-of-care systems and low-power resource settings.

Chapter 2: Results for healthcare application of graphene oxide sensor

2.1. Introduction

In this project, we present a portable non-invasive approach for measuring indicators of inflammation and oxidative stress in the respiratory tract by quantifying a biomarker in exhaled breath condensate (EBC). We discuss the fabrication and characterization of a miniaturized electrochemical sensor for detecting nitrite content in EBC using reduced graphene oxide. The nitrite content in EBC has been demonstrated to be a promising biomarker of inflammation in the respiratory tract, particularly in asthma. We utilized the unique properties of reduced graphene oxide (rGO); specifically, the material is resilient to corrosion while exhibiting rapid electron transfer with electrolytes, thus allowing for highly sensitive electrochemical detection with minimal fouling. Our rGO sensor was housed in an electrochemical cell fabricated from polydimethyl siloxane (PDMS), which was necessary to analyze small EBC sample volumes. The sensor is capable of detecting nitrite at a low over-potential of 0.7 V with respect to an Ag/AgCl reference electrode. We characterized the performance of the sensors using standard nitrite/buffer solutions, nitrite spiked into EBC, and clinical EBC samples. The sensor demonstrated a sensitivity of 0.21 $\mu A\ \mu M^{-1}\ cm^{-2}$ in the range of 20–100 μM and of 0.1 $\mu A\ \mu M^{-1}\ cm^{-2}$ in the range of 100–1000 μM nitrite concentration and exhibited a low detection limit of 830 nM in the EBC matrix. To benchmark our platform, we tested our sensors using seven pre-characterized clinical EBC samples with concentrations ranging between 0.14 and 6.5 μM. This enzyme-free and label-free method of detecting biomarkers in EBC can pave the way for the development of portable breath analyzers for diagnosing and managing changes in respiratory inflammation and disease.

2.2. Material and Methods

2.2.1. EBC sample collection

Briefly, 1–2 mL of EBC was collected during 20 min of tidal breathing from each of seven adult subjects using an EcoScreen device (Jaeger, Wurzburg, Germany), which condensed the exhaled breath at −20 °C. All surfaces were triple-rinsed with nitrite-free water prior to contacting the EBC, and the samples were frozen at −80 °C for later analysis. In the previous study, nitrite concentrations were measured using selective catalytic reduction and chemiluminescence detection (NOA 280i, GE Analytics, Boulder, CO, USA) [108]. All solutions were prepared with distilled water. For testing and calibration of the sensors, we experimented with various buffers, including sodium nitrite, acetate, and phosphate buffers (Sigma-Aldrich, St Louis, MO, USA).

2.2.2. Sensor fabrication and characterization

2.2.2.1. Drop cast method

Graphene oxide was prepared using the Hummers method [109]. Screen-printed three-electrode micro-chips consisting of Ag/AgCl reference electrodes, platinum counter electrodes, and 5-mm gold working electrodes were commercially obtained (Metrohm, Herisau, Switzerland). The morphology of the graphene oxide was characterized using field-emission scanning electron microscopy (SEM) (Zeiss leo Field emission SEM, Carl Zeiss, Inc., One Zeiss Drive, NY, USA) and atomic force microscopy (AFM) (Digital Instruments Nanoscope IV, Digital Instruments, NY, USA). The atomic force microscope was operated in tapping mode using standard cantilevers with a spring constant of 40 N m^{-}

[1] and a tip curvature of o 10 nm. FT-Raman spectra (Horiba Johin-Yvon Micro Raman Spectrometer, 532 nm excitation laser, HORIBA, NY, USA) were recorded to characterize the reduction of the graphene oxide substrates. Electrochemical measurements (PSTAT Princeton Instruments, Trenton, NJ, USA) were performed under ambient conditions. All potentials were applied with respect to the Ag/AgCl reference electrode. The steps used to fabricate the integrated reduced graphene oxide electrode/micro-electrochemical cell are shown in figure 2-1.

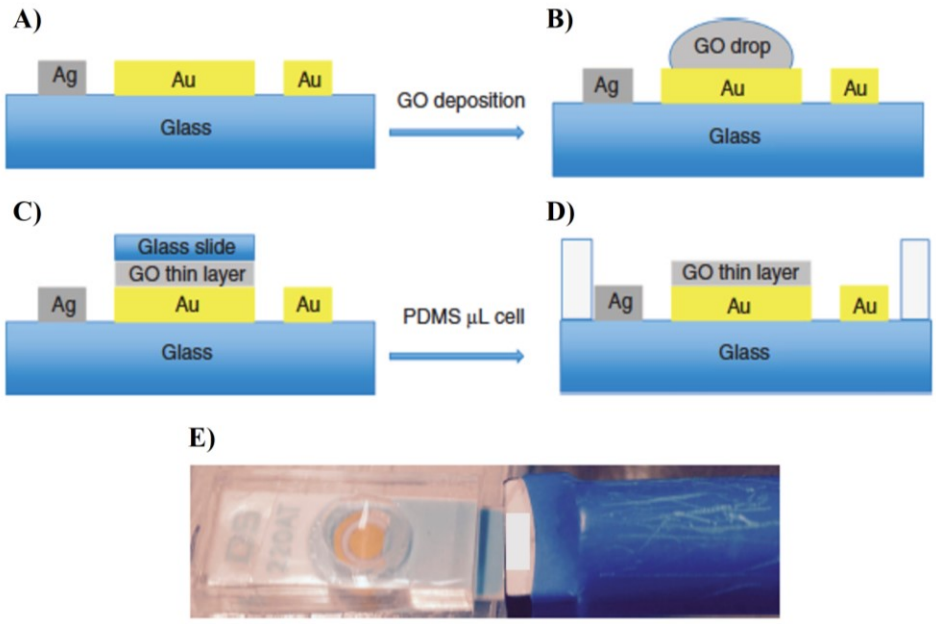

Figure 2-1. Fabrication process for the reduced graphene oxide biosensor formed in a micro-electrochemical fluidic cell. (A) Shows electrodes of screen printed electrodes and (B) Shows dropping 2 micro-litter graphene oxide solution on top of gold working electrode, creating thin layer graphene oxide layer indicates in part (C), part (D) shows how we can have small volume area with PDMS membrane and part (E) shows image of sensor we used for detection nitrite [9].

First, a 3-µL aliquot of graphene oxide suspension, which was synthesized from graphite powders using the Hummers method, was placed on the gold electrode surface. Then, a thin glass slide was placed on top of the droplet to cast the GO onto the gold electrode.

Superfluous solution was aspirated, and the surface was dried at room temperature. The GO layer was then reduced electrochemically in acetate buffer (pH 5.5) using cyclic voltammetry between −1.6 and 0 V at a scan rate of 25 mV for 30 cycles under continuous N_2 purging. The micro-electrochemical cell was fabricated by forming a thin layer of PDMS on top of the insulated layers of the SPE micro-chip. Then, a thicker PDMS layer containing an 8-mm hole was covalently bonded to the thin PDMS layer using O_2 plasma treatment. During O_2 plasma treatment, the rGO layer and the wire-bonding pads of the SPE micro-chip were protected with a glass slide.

2.2.2.2. Spin coat method

The steps required to modify the working electrode with a spin-coated layer of GO are shown in figure 2-2. First a thin PDMS membrane is spin coated onto the screen-printed electrode. This step is performed for two purposes. First, the PDMS protects the counter and reference electrode from electrical shortage during deposition of GO solution. Second, the PDMS layer serves as a substrate for microfluidic channel.

To prepare the PDMS mask, a 10:1 ratio of Sylgard PDMS with respect to the curing agent was mixed together thoroughly. After degassing and removing bubbles, the PDMS thin film was coated in a two-step process with 500 rpm for 5 seconds and 4000 rpm for 30 seconds on the SPE substrate. After curing in 80 °C for 1 hour, an approximately 20 μm thick PDMS membrane is formed on top of the electrodes. The film of PDMS on top of the working electrode was manually removed and then the solution of GO was deposited on top of the working electrode with the same coating parameters.

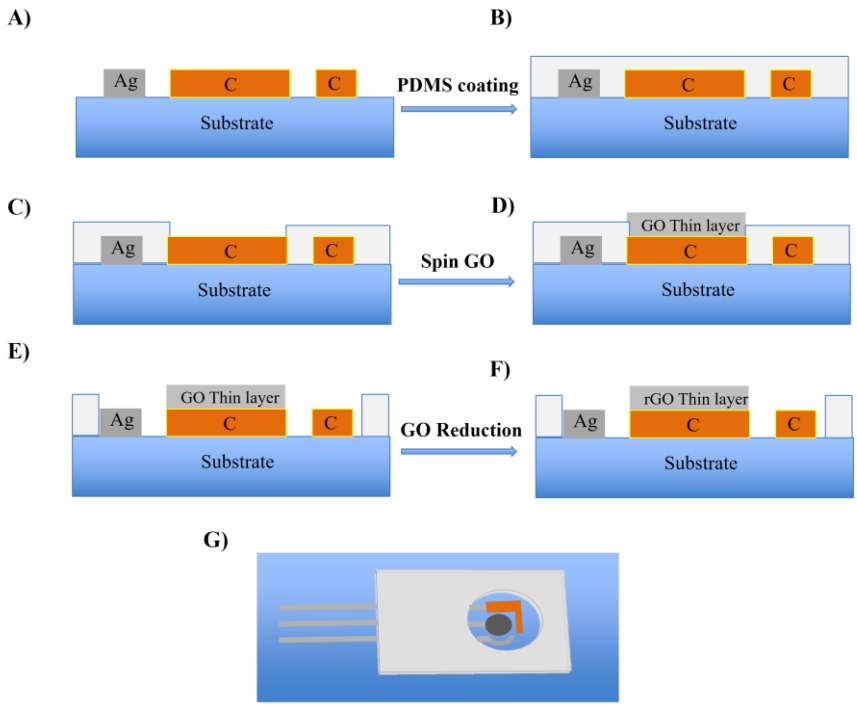

Figure 2-2. Fabrication process for spin coated GO thin film on Gold SPE electrode.

Afterwards, the PDMS membrane was removed from the counter and reference electrodes and the contact pads. The substrate is then washed with isopropyl alcohol to ensure removal of possible residue of PDMS from the surface of the electrodes. To increase conductivity of the GO sensor it converted into reduced graphene oxide (rGO), GO was reduced electrochemically with same process of drop cast method.

2.3. Results

2.3.1 Characterization of graphene oxide sensors

2.3.1.1. Drop casted thin film

Figure 2-3A shows AFM images of GO deposited on a Si/SiO_2 substrate. In most areas,

there is a uniform flat GO layer with wrinkles and areas in which agglomeration has occurred. These can be produced during vaporization of the solvent, which can perhaps be avoided by using a lower concentration of GO solution or by drying the substrate in a vacuum. However, because our focus was on the electrochemical properties of GO and the sensitivity of the nitrite sensor (rather than the intrinsic electronic properties of GO), we intentionally did not remove these defects. In addition, the electrochemical edges of GO might be more sensitive than the flat regions. The effects of these defects on sensitivity should be systematically explored in future studies but were considered beyond the scope of this work. To ensure reproducible fabrication, the same concentrations and volumes and top glass slides of equal size were used. An advantage of using electrochemical graphene sensors is that we can obtain the active surface area from the slope of a plot of the current versus the square root of the scan rate and, instead of absolute current, the data can be calibrated and reported as current density. In this way, we can neglect possible differences between the coverage of graphene on the electrode surface. In addition, this film-coated glass slide method yields more uniform coatings than the usual drop cast method and avoids agglomeration, which can cause large differences in active surface area between electrodes.

Figure 2-3B shows a representative SEM image obtained from a larger area of the GO layer that was directly deposited on a gold electrode. This image shows that we were able to fully cover the surface uniformly, even on a gold working electrode with a surface roughness of several microns. The image also indicates that the number of stacked GO layers was minimized. The modified drop-cast method presented here is thus more suitable for obtaining larger areas of GO without agglomeration than regular drop casting.

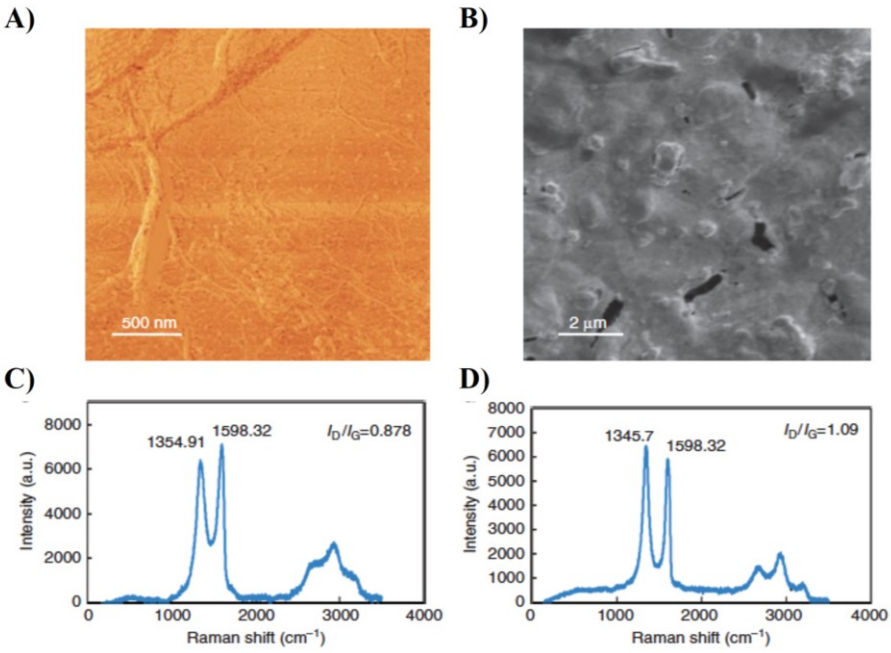

Figure 2-3. (A) Atomic force microscopy image of the GO layer on Si/SiO_2. (B) SEM of the GO thin layer on a gold electrode surface. (C) Raman spectrum of GO. (D) Raman spectrum of rGO [9].

The efficiency of the electrochemical reduction of GO was also investigated using Raman spectroscopy. Figure 2-3C shows the Raman spectrum of the GO substrate before reduction, and figure 2-3D shows the Raman spectrum of the same substrate after 30 cycles of electrochemical reduction. The data shown represent the average of three measurements that were recorded at different areas/spots on each sample.

The main features observed in Raman spectra of carbon-based materials are the G and D peaks. These peaks arise from vibrations of sp^2 carbons and appear at ~ 1580 and 1350 cm^{-1}, respectively. The overtone of the D peak appearing at ~ 2700 cm^{-1} is termed the 2D peak. Unlike mechanically exfoliated graphene, GO is more disordered; therefore, the 2D band is usually of low intensity. Thus, GO and rGO can be distinguished based on the G and D peaks and the magnitude of the ratio of their intensities. In addition, the G peak

of GO and rGO is shifted to higher frequencies (1598 cm^{-1}) with respect to graphene and graphite due to the presence of defects. During the thermal reduction of GO, I_D/I_G remains constant, although an increase in the I_D/I_G ratio of rGO after electrochemical reduction has been reported in the literature [110]. In this study, this ratio was significantly increased compared to that for GO (from 0.87 to 1.1). This shows a restoration of sp^2 carbons and a decrease in the average size of the sp^2 domains after the electrochemical reduction of GO. An increase in the magnitude of the 2D peak also suggests enhanced graphitization [111].

2.3.1.2. Spin coated thin film

Figure 2-4 shows SEM and Raman analysis of spin coated reduced graphene oxide on carbon electrode. SEM images show a representative data obtained from a larger area of the GO layer that was directly deposited on a carbon electrode. These images show that we were able to fully cover the surface uniformly, even on a carbon-working electrode with a surface roughness of several microns. Raman data show the spectrum of the GO substrate before reduction, and for the same substrate after 30 cycles of electrochemical reduction. The data shown represent the average of three measurements that were recorded at different areas/spots on each sample.

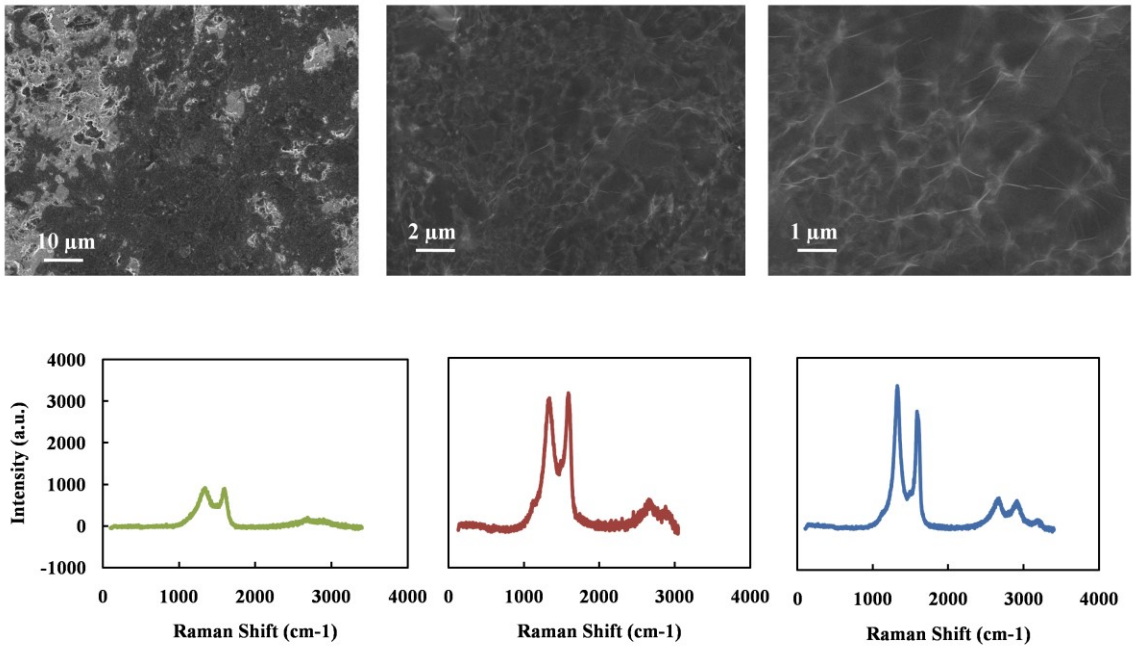

Figure 2-4. SEM of graphene oxide on Carbon electrode in different magnifications, Raman spectroscopy of Carbon working electrode (green plot), GO thin film (red plot) and rGO thin film (blue plot) on top of carbon electrode.

2.3.2. Electrochemical detection of nitrite

2.3.2.1. Using electrolyte

After fully reducing the GO electrode, we characterized the electrochemical performance of our platform for nitrite detection. Because both electrolyte identity and pH affect the sensitivity and detection limit of the sensor, we investigated the electrochemical response of the rGO sensor using cyclic voltammetry in various electrolytes. Figure 2-5A shows the oxidation peak of 5 mM nitrite in phosphate-buffered saline (PBS, pH 7.4), 0.1 M KCl, and acetate buffer (pH 6) as measured at a scan rate of 50 mV s^{-1}. Anodic peaks appeared at 0.69, 0.7, and 0.63 V for the PBS, KCl, and acetate buffers, respectively. Given that the goal of this work is to develop a portable sensing platform that can operate under ambient

conditions (in which O_2 may react with the analyte), we avoided purging O_2 in our samples. This enabled us to assess how the sensor will perform on real biological samples under ambient conditions. As seen from the voltammetric measurements conducted in EBC samples, the voltage of the oxidation peaks was shifted to positive voltages; this is more a favorable regime to use due to the lower over-potentials.

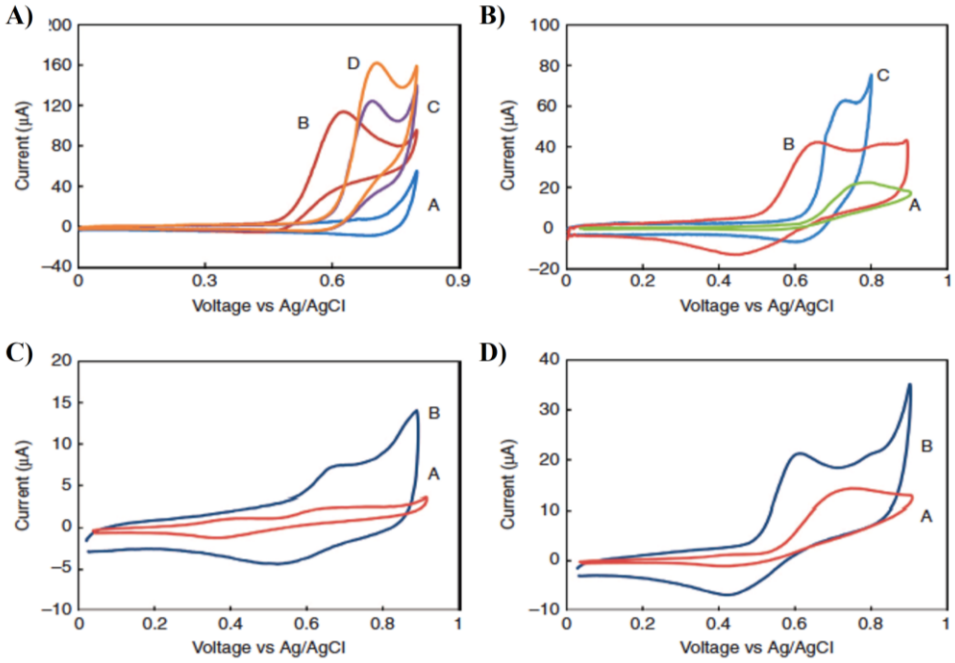

Figure 2-5. Current versus voltage curves obtained using A) cyclic voltammetry and the rGO electrode. (A) PBS after washing three times; (B) 5 mM nitrite in acetate buffer, pH 6, (C) 0.1 M KCl, and (D) PBS buffer, pH 7.4. B) Cyclic voltammetry measurements of 1 mM nitrite and (A) the gold electrode of SPE and rGO in (B) acetate buffer, pH 6, and (C) PBS buffer, pH 7.4, respectively. The voltage range is 0–0.9 V, and the scan rate is 50 mV s^{-1}. C, D) Cyclic voltammetry of (A) GO, (B) rGO in the presence of 100 μM and 1 mM nitrite. The scan rate is 25 mV s^{-1} [9].

We therefore opted to use the acetate buffer (pH 6) as the electrolyte for the remainder of the experiments. Another important factor in our deciding to use acetate was the fact that EBC samples from patients with inflammatory disease are reportedly acidic [112]. Thus, pH 6 more closely approximates the actual pH of EBC samples that would be obtained from patients with chronic inflammatory disease.

The performance of the rGO-modified electrodes was compared to those of the SPE- and GO-deposited electrodes. Figure 2-5B shows a comparison between the anodic peaks in the presence of 1 mM nitrite for rGO electrodes at pH 6 and pH 7.4 and those for the SPE electrodes at pH 6 (50 mV s^{-1} scan rate). As clearly seen from the figure, rGO has a higher current and lower over-potential than the unmodified SPE electrode. Figures 2-5C and D also show the response of both the GO- and rGO-modified electrodes in the presence of 100–1000 µM nitrite, respectively (scan rate, 25 mV s^{-1}).

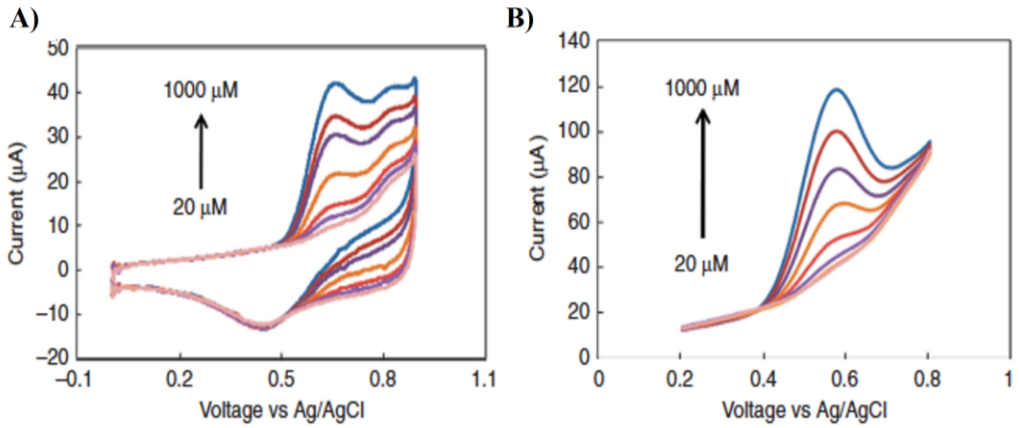

Figure 2-6. Current versus voltage curves obtained using (A) cyclic voltammetry of varying concentrations of nitrite from 20 to 1000 µM at pH 6 with a scan rate of 50mVs^{-1}. (B) Square wave voltammetry of varying concentrations of nitrite. Square wave voltammetry was also performed from 0 to 0.9 V with a step potential of 10 mV, an amplitude of 50 mV, and a frequency of 5 Hz [9].

Figure 2-6 shows the result of cyclic voltammetry (figure 2-6A) and square wave (figure 2-6B) voltammetry analysis for nitrite concentrations from 20 to 1000 µM (scan rate, 50 mV s^{-1}).

2.3.2.2. Using blank EBC

Figure 2-7 shows electrochemical performance of sensor in nitrite standard solution. As you can see acetate peaks occurs in lower voltage so it is better electrolyte for study the nitrite detection compare to PBS. EBC blanks obtained from R-tube and Eco-screen have been used as the basic matrix to have most similar electrolyte to EBC samples for comparison of results with standard electrolytes. In addition, DPV results shows the blank samples that obtained washing R-tube and Eco-screen sampling devices have enough electrical connectivity to be used as electrolyte.

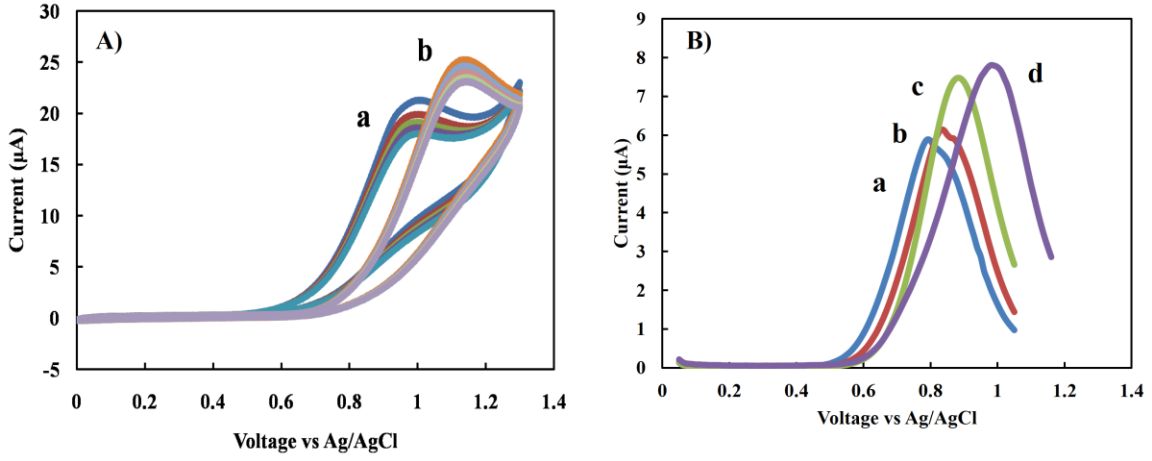

Figure 2-7. A) Cyclic Voltammetry of 1 mM nitrite in a) acetate and b) in PBS solution. B) Differential pulse voltammetry in a) R-tube bulk, b) Eco-screen bulk, c) acetate, d) PBS.

The DPV and calibration curve of spiked nitrite in EBC blank sample form R-tube and Eco-screen were shown in figure 2-8 and 2-9 respectively.

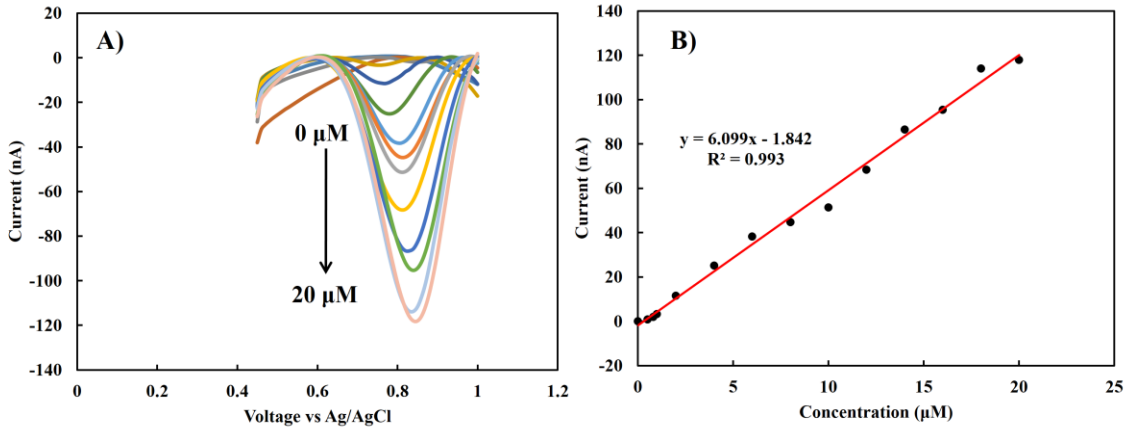

Figure 2-8. A) Differential pulse voltammetry of different nitrite concentration in R-tube EBC bulk. B) Calibration curve.

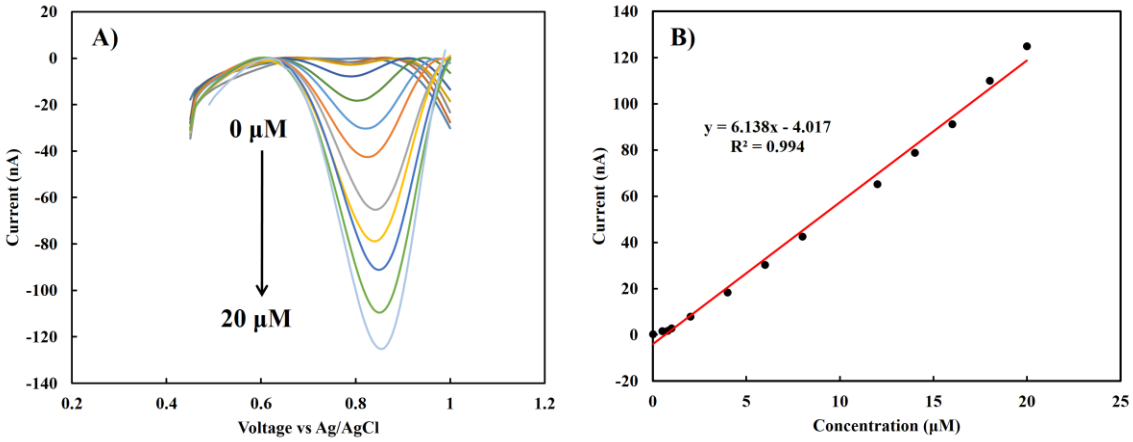

Figure 2-9. A) Differential pulse voltammetry of different nitrite concentration in Eco-screen EBC bulk. B) Calibration curve.

2.3.3. Detection of nitrite in clinical EBC samples

After the performance of the fabricated sensor was confirmed in a standard electrolyte containing various concentrations of nitrite, we proceeded to test the graphene-based

sensors in the complex biological matrix of EBC to study the effects of that biological matrix on the sensor. The results obtained provide insight into the response expected for clinical samples. Nitrite levels in EBC have been reported in the μM range [108, 113]. We used both cyclic voltammetry (CV) and square wave voltammetry (SWV) to measure the redox current resulting from spiking buffer solutions with various concentrations of nitrite into the EBC sample. Figures 2-10A and B show the voltammetric response of the sensor to solutions containing 2–1000 μM nitrite at a scan rate of 25 mV s^{-1}. The magnitude of the redox current generated for 1 mM nitrite was similar between the EBC and buffer solution matrices (figure 2-10D). However, as previously mentioned, the potential in the EBC was shifted to a higher over-potential of 0.79 V. This can occur because the presence of proteins in EBC samples can slow electron transfer. The insets shown in figures 2-10a and b are calibration curves based on CV measurements. The response of sensor is linear in the concentration range of interest. We also studied the analytical performance of the nitrite sensor by taking SWV measurements conducted in the range of 0–0.9 V. Figure 2-10C displays the square wave voltammograms of nitrite in the range from 2 to 1000 μM. The redox current peak is found at ~ 0.7 V. Figure 2-10D shows the calibration curve obtained using SWV.

To consistently compare the performance of different sensors and account for device-to-device variations, we report sensitivity based on current density, which requires a knowledge of the active surface area of the electrodes. We used the Randles–Sevcik equation to calculate current density. We performed cyclic voltammetry on 5 mM $K_3Fe(CN)_6$ and plotted the peak current versus $\nu^{1/2}$.

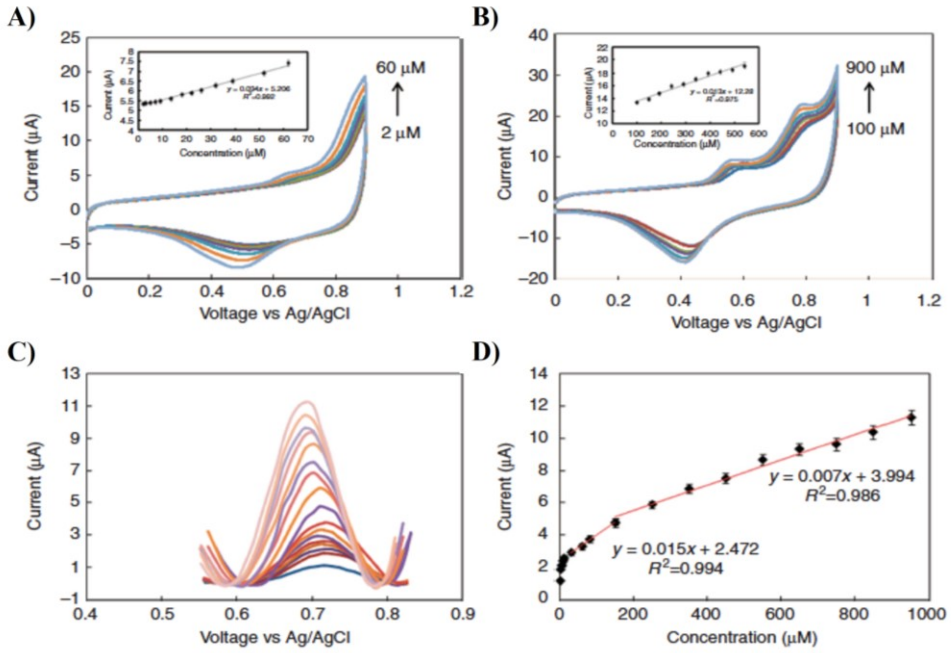

Figure 2-10. (A,B) Cyclic voltammogram of rGO electrodes at different nitrite concentrations ranging from 2 to 60 μM and 100 to 900 μM, which were spiked into the EBC samples (scan rate of 25 mV s^{-1}). (C) Square wave voltammogram of spiked (concentration range from 0 to 1000 μM) EBC samples. The pulse amplitude is 50 mV. (D) Calibration curve showing the respective slopes [9].

Based on the Randles–Sevcik equation, the relation- ship is linear, and thus the slope of the curve can be used to determine the active surface area. From the slope, we estimated the active surface area of the electrode to be ~0.07cm^2. This allows the sensitivity to be determined based on the surface area in the linear dynamic range. For EBC samples, the sensitivity is 0.21μA$μM^{-1}cm^{-2}$ in the range from 20 to 100 μM and the sensitivity is 0.1 μA $μM^{-1}$ cm^{-2} in the range from 100 to 1000 μM. We determined the detection limit to be 830 nM based on three standard deviations. The detection sensitivity of nitrite in the presence of EBC is comparable with values reported in the literature for nitrite content in various buffers [114, 115].

After validating the functionality of the rGO nitrite sensor with spiked EBC samples, we proceeded to test the accuracy of the devices using a set of seven previously characterized

clinical EBC samples. We performed SWV for each of the seven characterized samples (figure 2-11A). The slight differences in oxidation potential between samples might be due to differences in the complex EBC matrix between individuals. The nitrite concentration in each sample was calculated from the measured oxidation currents based on the calibration data obtained using the spiked standard nitrite solutions in EBC (figure 2-11B). We benchmarked the accuracy of our measurements by comparing the readings from our graphene-based sensor with measurements obtained using an ozone-based chemiluminescence technique [116]. Figures 2-11C and D show the results of this comparison. The range of measured nitrite concentrations based on the chemiluminescence experiments is 0.14–6.5 µM. For at least five of the seven samples, the relationship is linear, and strong agreement is found between the results obtained using the rGO sensor and the chemiluminescence measurements.

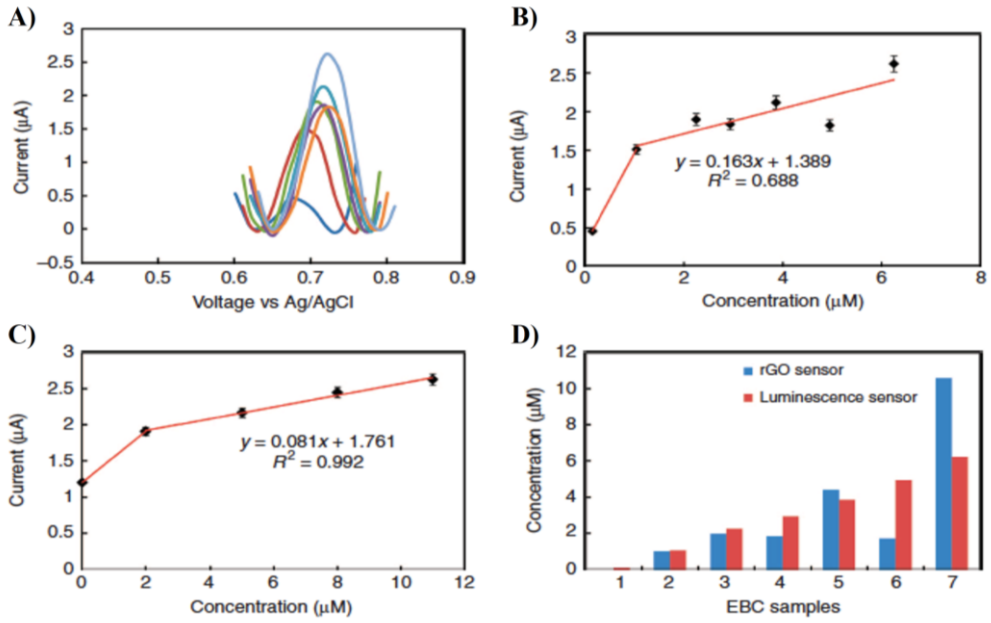

Figure 2-11. (A) Square wave voltammogram obtained for seven EBC samples. (B) The calibration curve was obtained based on results obtained using spiked samples, (C) a calibration curve based on chemiluminescence data, (D) a comparison between predicted concentration and chemiluminescence data [9].

Regarding the two outlying data points (samples 6 and 7), more experimentation is necessary to understand the possible reasons behind their deviation. One possibility relates to the fact that the EBC samples were collected, frozen, and characterized by chemiluminescence several years prior to the electrochemical characterization experiments that were performed in this current study. This opens up the possibility that the nitrite content might have degraded over time in the frozen EBC samples (due to the possible conversion of nitrite to nitrate), thus highlighting the need for methods that can be used to measure samples at point- of-use immediately upon their collection from patients. In this experiment, acetate buffer (pH 6) was added to the EBC samples in a 1:1 ratio, and we assumed that the pH and conductivity of the samples were consistent between samples; however, it is possible that this assumption was not completely valid and that pH and conductivity might have varied between samples. Because the EBC sample volumes were small, we could not use a standard- sized pH meter electrode to measure pH; thus, we were unable to independently validate the consistency of pH and conductivity among the samples. To correct this problem, the integration of a microfabricated pH sensor and conductivity sensor on the same chip might provide insights that would allow more precise comparisons between samples.

2.3.4. Study storage effect on nitrite detection

First the case study of fresh real EBC samples has been performed. Our sensor successfully distinguished between patients and blank samples with detection limit as low as nanomolar without any pretreatment. Results show this sensor can detect nitrite as low as 250 nM with high sensitivity. In addition, storage causes a decrease in the amount of

nitrite, likely due to freezing. This study demonstrates the improvement in accuracy obtained from real-time measurement of nitrite in EBC.

Figure 2-12 indicates the results for case study of fresh and stored EBC samples. Figure 2-12 A shows CV curves for fresh samples have been taken form 5 different patients. Figure 2-12 B shows DVP of the same EBC samples. Figure 2-12 C shows the DPV results we have taken after one-month storage of samples in -80 degree. As you can see in the figure 2-12 D it is obvious for most cases the freezing the samples causes reducing the amount of nitrite. These results indicates how important is to measure the nitrite exactly after collecting samples from a patient. It emphasizes the importance of point of care and portable design of biosensors for diagnosis of lung inflammation diseases.

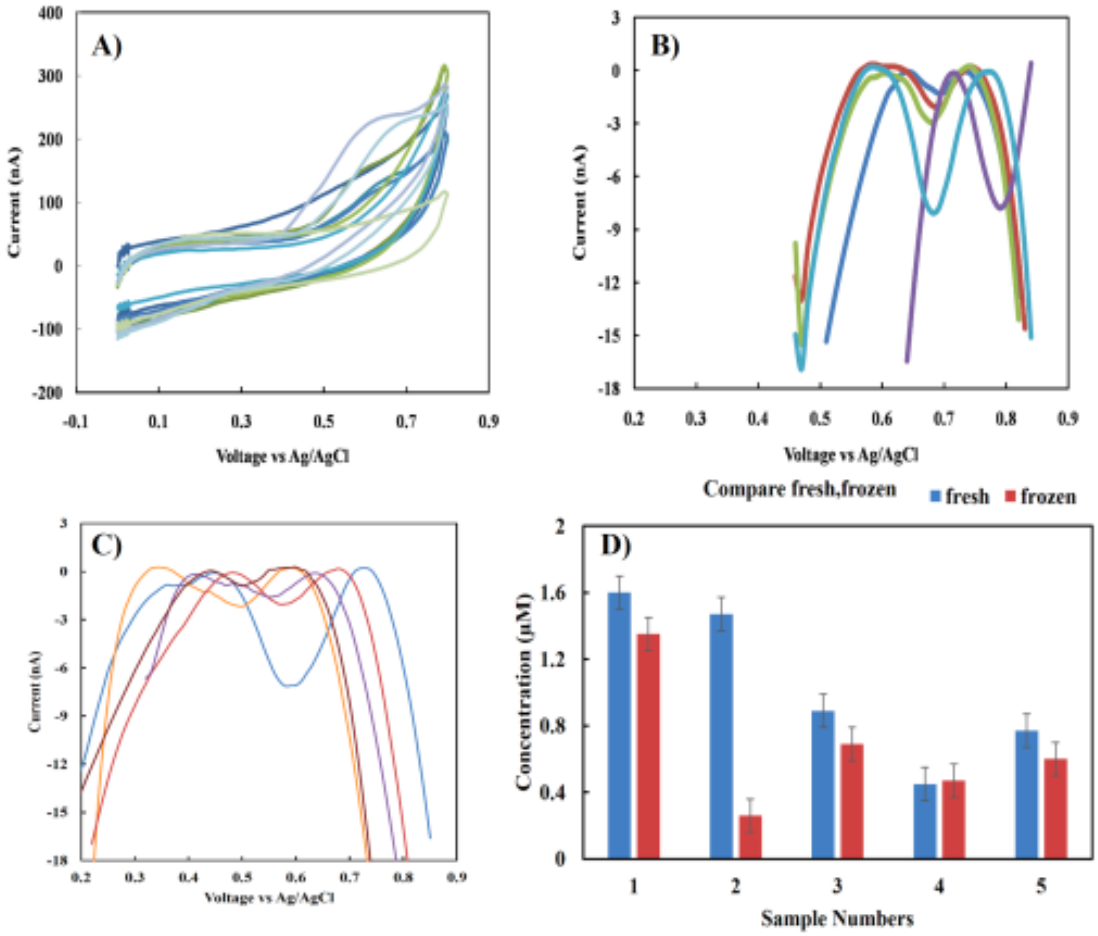

Figure 2-12. A) CV of fresh EBC samples. B) DPV of Fresh EBC samples, C) DPV of frozen EBC samples, D) Concentration of nitrite in fresh and frozen EBC samples.

2.3.5. Study electrical properties effect on nitrite detection

Electrochemical impedance spectroscopy is a powerful tool to study electrical properties of the surface and solution. EIS results of EBC samples show in figure 2-13. The results indicate the electrical differences between the EBC samples and emphasize the ionic nature of patient samples are different from each other and we need to take account of it in the prediction of nitrite from standard calibration curves.

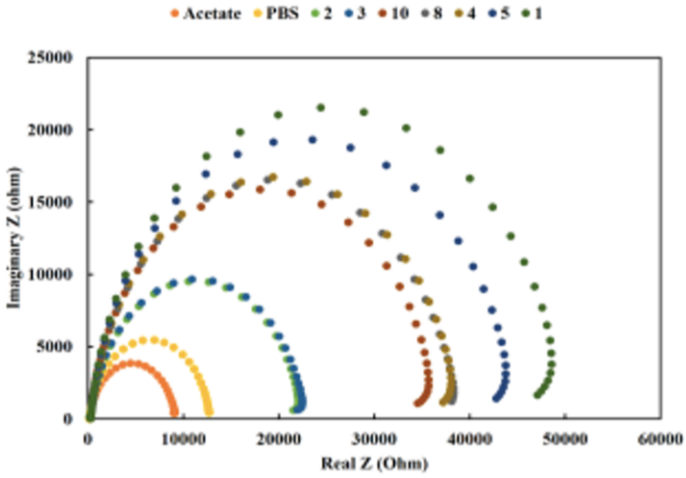

Sample	R_{ct} kohm	Rs ohm	C nF
1	49	279	748
2	22	279	821
3	22	275	762
4	38	280	771
5	44	273	775
8	38	279	846
10	36	286	812
Acetate	9	200	1044
PBS	12	188	780

Figure 2-13. Electrochemical impedance spectroscopy data of EBC samples and their circuit simulation parameters

2.3.6. Microfluidic based nitrite sensor

In the next step, we tried to detect nitrite using microfluidics chamber, so it can be used as real-time monitoring of nitrite with assembling this device to the collection system. As a proof of microfluidics-based sensor, we successfully fabricated a microfluidic chamber for previous designed graphene-based sensor and get amperometry results for nitrite in standard buffer solution (figure 2-14). With using this method, the required amount of EBC samples for analysis can be reduced into 10 µl. This can effectively decrease the time of sample collection and use as real time monitoring in situ with sample collection.

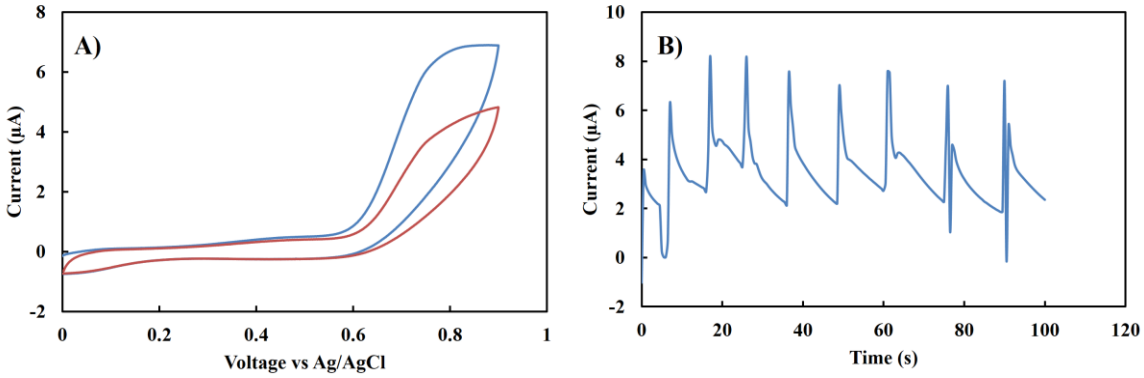

Figure 2-14. A) Cyclic Voltammetry of nitrite in microfluidic channel, B) Amperometry of 1 mM nitrite in microfluidic channel. Nitrite prepared in acetate buffer.

Table 2-1 shows the predicted concentration based on R-tube, Eco-screen and Acetate calibration curve that we previously reported in figures 2-9 and 2-10. So the predicted nitrite was calculated based on different sampling method was used for different patients. Table 2-2 shows the pH of each sample. The results indicate pH of samples is almost same in the range that can effect electrochemical measurement so it has negligible effect on predicted results. Table 2-3 shows the difference method and parameters that used for detection of nitrite.

Table 2-1. Predicted level based on different calibration curve

Fresh samples

Sample	Current (nA)	R-tube. concentration (µM)	Eco. concentration (µM)	Acetate. concentration (µM)
1	8.57	1.6	1.9	2.1
2	7.79	1.4	1.8	1.9
3	3.08	0.6	0.9	1
4	2.08	0.4	0.7	0.8
5	2.37	0.5	0.8	0.8

Frozen samples

Sample	Current (nA)	R-tube. concentration (µM)	Eco. concentration (µM)	Acetate. concentration (µM)
1	7.10	1.4	1.7	1.8
2	0.89	0.3	0.5	0.5
3	2.04	0.5	0.7	0.8
4	2.18	0.5	0.7	0.8
5	1.58	0.4	0.6	0.7

Table 2-2. pH of EBC samples

Sample	Type	pH
1	**R-tube sample**	**7.89**
2	**R-tube sample**	**7.64**
3	**EcoScreen sample**	**7.67**
4	**R-tube sample**	**7.70**
5	**EcoScreen sample**	**7.64**
8	**EcoScreen Blank**	**7.61**
10	**R-tube Blank**	**7.68**
Acetate	**0.1 M**	**6.00**
PBS	**0.1 M**	**7.00**

Table 2-3. Method and Parameters of nitrite detection

Method	**Indicator**	**Sample**	**Detection limit**	**Detection range**	**Ref**
Catalytic-spectrophotometric	Perphenazine	Water	0.07 ng/mL	0-4.5 ng/mL	[117]
Catalytic-spectrophotometric	Crystal violet	Water	0.3 ng/mL	1.0-50 ng/mL	[118]
Catalytic-spectrophotometric	Pyrogallol red	Water/Food	1 ng/mL	3-2000 ng/mL	[119]
Chemiluminescence	NO/O_3	Water	0.01 μmol/L	0.05-50 μmol/L	[120]
Chemiluminescence	Luminol/myoglobin	Urine	0.4 μmol/L	1-22000 μmol/L	[121]
Chemiluminescence	H_2O_2/carbon dots	Water/milk	0.053 μmol/L	0.1-10 μmol/L	[122]
Electrochemical	Thionine/ACNT	Food	1.12 μmol/L	3-500	[123]
Electrochemical	Au/GCE	Water	2.4 μmol/L	10-5000 μmol/L	[124]
Electrochemical	MWNT/GCE	Food	2.0 μmol/L	5-1500 μmol/L	[125]
Electrochemical	Fe2O3/rGO	PBS	0.015 μmol/L	0.05-780 μmol/L	[19]
Chromatography	Fluorescence	Biological	0.01 μmol/L	0.01-2 μmol/L	[126]
Chromatography	UV	Water	0.2 μmol/L	0-2000 μmol/L	[127]
Chromatography	Chemiluminescence	Water	0.002 μmol/L	0.002-2.5 μmol/L	[128]
Capillary electrophoresis	UV	Food	2.3 μmol/L	5-100 μmol/L	[129]
Capillary electrophoresis	Fluorescence	Plasma	0.0006 μmol/L	0.002-0.5 μmol/L	[130]
Capillary electrophoresis	Electrochemical	NA	1 μmol/L	10-250 μmol/L	[131]
Electrochemical	rGO/SPE	Exhaled breath condensate	0.25 μmol/L	0.25-1000 μmol/L	This work

2.4. Conclusion

In this study, we utilized the outstanding properties of graphene- based electrodes to fabricate and characterize an enzyme-free sensor that proved capable of detecting nitrite samples in clinical samples of exhaled breath condensate. We also formed a micro-electrochemical cell using PDMS, which allowed us to perform measurements using small sample volumes of the target material (EBC). We systematically optimized various electrochemical parameters in buffer solution, thus allowing us to accurately measure nitrite in human EBC samples. The sensitivity of the nanofabricated sensor was 0.21 μA $\mu M^{-1}\, cm^{-2}$ in the range from 20 to 100 μM and 0.1μA $\mu M^{-1}\, cm^{-2}$ in the range from 100 to 1000 μM with a detection limit of 830 nM. Most importantly, we were able to validate the performance of our sensors on clinical EBC samples that had been previously characterized using chemiluminescence. We demonstrated that the sensor exhibited high levels of precision in quantifying nitrite in the clinically relevant μM range. Future studies can be dedicated to fabricating sensors with improved detection limits using techniques, such as the use of nanoparticle-RGO composites and enzymatic modification of the electrodes, as well as improving the sensitivity of the electronic readout instrumentation. These results of important parameters reveal the importance of fabrication of portable biosensor that can detect nitrite amount in fresh samples just after the collection of them. In addition among of different properties, the method of collection samples and electrical properties of EBC samples have a more important influence on the performance of the sensor and they should be taken in account in prediction and reporting of nitrite amount in EBC samples.

Chapter 3: Results for environmental application of graphene oxide sensor

3.1. Introduction

This project presents an integrated on-chip sample-to-answer platform capable of qualitatively detecting lead ions directly in sediment samples. Sediment is one of the main sources of hazardous heavy metals in aquatic ecosystems. Rapid and real time detection of heavy metals in sediment is very crucial in the field of environmental monitoring. In-situ measurement of heavy metals with electrochemical sensors has been limited because of complicated pretreatment steps necessary to be performed on sediment. In this work, we present a sample-to-answer platform capable of on-chip sediment digestion and purification in conjunction with electrochemical quantification of lead ions. We have developed an integrated system consisting of a porous matrix for purification and extraction of Pb^{+2} on top of a graphene oxide thin film as the active sensing material. Although the proposed sensing platform is applicable to detection of a wide panel of toxic metals, we focused on platform validation using lead (Pb). First, the coated graphene oxide layer was characterized using electron microscopy, atomic force microscopy, and Raman. Then, we systematically studied optimization of various parameters affecting sensitivity and performance. Upon determining optimum experimental parameters, lead standard solution was analyzed with the optimized conditions. A linear working range with a detection limit of 4 ppb was established. After optimization of pretreatment parameters, the proposed electrochemical sensor was integrated with a 3D porous matrix for extraction and purification of lead ions for on-chip sample-to-answer analysis of complex sediment samples. The ability to detect lead directly in sediment samples with a minimum volume

of pretreatment agents and time makes this system a promising solution for in-situ detection of heavy metals for environmental monitoring.

3.2. Material and Methods

3.2.1. Reagents and Instrumentation

Pb (II) standard solution was prepared using lead nitrate stock standard solution in various supporting electrolytes. GO solutions were prepared from standard stock solution of 2 $mgmL^{-1}$ (Sigma Aldrich, MO, USA). To avoid aggregation of GO sheets, each solution underwent ultrasonication and centrifugation immediately prior to spin coating.

A potentiostat (Gamry 600, Gamry Instruments, Pennsylvania, USA) was used to perform electrochemical measurements. Screen printed electrodes with gold working (5 mm) and counter electrodes and an Ag/AgCl reference electrode was purchased from USA Metrohm. All electrochemical experiments were conducted in ambient conditions, except for reduction of GO which underwent purging using high purity nitrogen. Ambient conditions were chosen to ensure that platform is fully compatible with field-use.

The morphology of graphene oxide was characterized using field-emission scanning electron microscopy (SEM) (Zeiss Leo Field Emission SEM, Carl Zeiss) and atomic force microscopy (AFM) (Digital Instruments Nanoscope IV). The atomic force microscope was operated in tapping mode using standard cantilevers with a spring constant of 40 N m^{-1} and a tip curvature of 10 nm. FT-Raman spectra (Horiba Johin-Yvon Micro Raman Spectrometer, 532 nm excitation laser) were recorded to characterize graphene oxide substrates. The sediment sample was collected in the Arthur Kill at the mouth of Morse's

Creek in Linden NJ. It was collected using a Smith Mack box corer lowered from a boat in a depth of approximately 6 feet of water. The sample consisted of a composite of the sediments from 0 to 25 cm below the sediment water interface.

3.2.2. Sensor Fabrication

3.2.2.1. Spin coat method

The compact sensor system developed herein comprises two main components, (i) a modified electrochemical sensor with GO, and (ii) a pretreatment column consisting of a cellulose sponge. The steps required to modify the gold working electrode with a spin coated layer of GO are shown in figure 3-1.

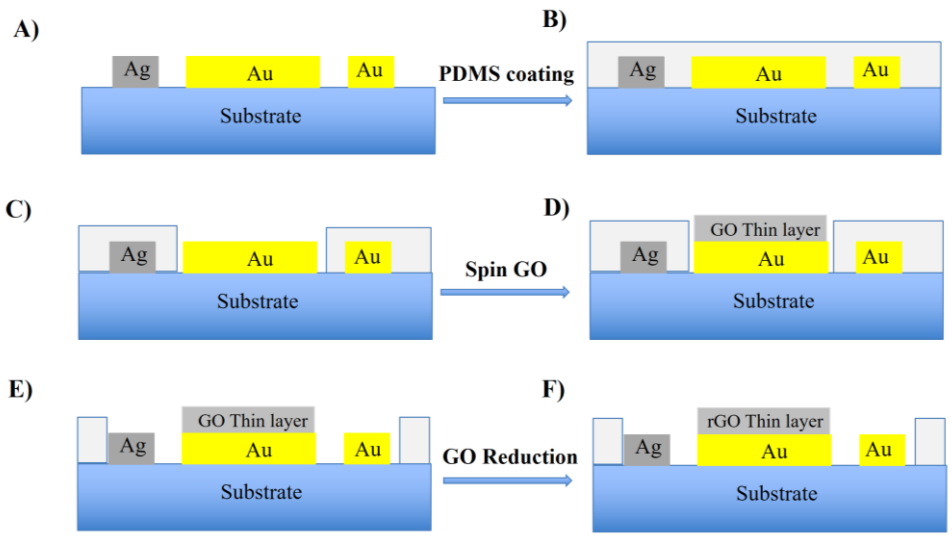

Figure 3-1. Fabrication process for spin coated GO thin film on Gold SPE electrode.

First a thin PDMS membrane is spin coated onto the screen printed electrode. This step is performed for two purposes. First, the PDMS protects the counter and reference electrode from electrical shortage during deposition of GO solution. Second, the PDMS layer serves

as a scaffold to structurally support the pretreatment column. To prepare the PDMS mask, a 10:1 ratio of Sylgard PDMS with respect to the curing agent was mixed together thoroughly. After degassing and removing bubbles, the PDMS thin film was coated in a two-step process with 500 rpm for 5 seconds and 4000 rpm for 30 seconds on the SPE substrate. After curing in 80 °C for 1 hour, an approximately 20 μm thick PDMS membrane is formed on top of the electrodes. The film of PDMS on top of the working electrode was manually removed and then the solution of GO was deposited on top of the working electrode with the same coating parameters. Afterwards, the PDMS membrane was removed from the counter and reference electrodes and the contact pads. The substrate is then washed with isopropyl alcohol to ensure removal of possible residue of PDMS from the surface of the electrodes.

To compare the performance of the GO sensor with reduced graphene oxide (rGO), GO was reduced electrochemically using cyclic voltammetry between -1.6 to 0 V in 0.3 M acetate buffer (pH 5) with a scan rate of 25 mV s^{-1} for 30 scans under continuous Nitrogen gas (N_2) purging. We used platinum as the choice of the counter electrode material to avoid damage during the reduction process.

3.2.2.2. In-situ pretreatment set up

The pretreatment column is assembled with a 5 mm PDMS layer. To connect column to sensor active site, an 8 mm hole is punched through the PDMS layer. An Eppendorf tube is used as the pretreatment column. The pretreatment column adheres on top of the hole with glue. A sponge (2 mm high) is located between the sediment sample and the hole inside the column. Syringe tips are used for inserting the required agents for pretreatment. Figure 3-2 shows the schematic and an image of the fabricated compact sensor set up. The

pretreatment column is assembled with a 5 mm thickness PDMS layer. An Eppendorf tube is used as pretreatment column. A sponge is located between sediment sample and the hole inside the column. The pretreatment column is connected on top of sensor with glue through the 8 mm hole punched on PDMS layer. Syringe tips are used for inserting required agents for pretreatment inside the setup.

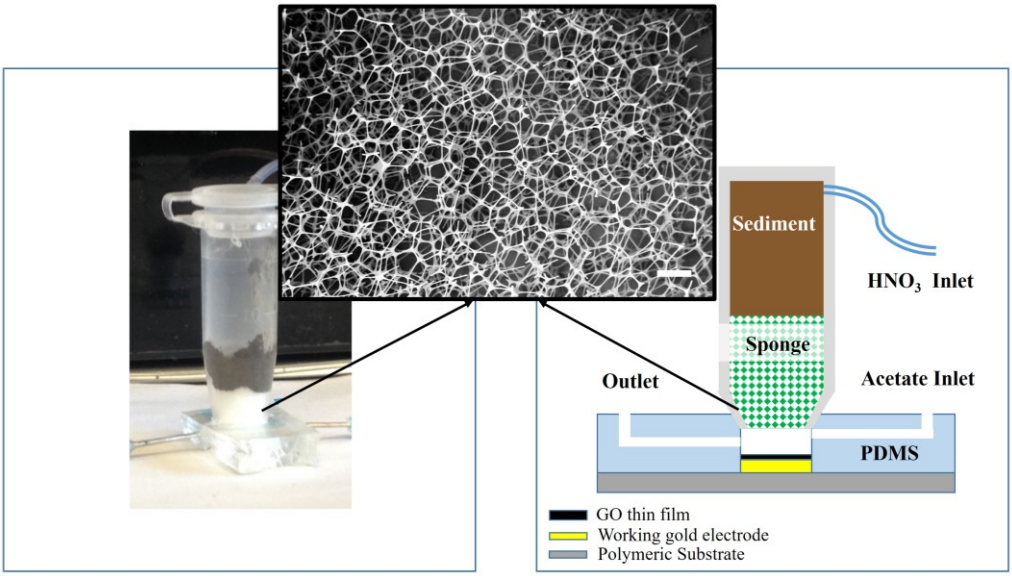

Figure 3-2. The image of compact electrochemical lead sensor. The schematic of set up design and SEM of cellulose sponge, scale bar is 200 µm.

3.3. Results

3.3.1. GO thin film characterization and optimization

The morphology of the graphene oxide film was studied using AFM and SEM. Raman spectroscopy was used to determine the extent of reduction of the graphene oxide layer. Figure 3-3A shows the SEM image taken from a spin-coated 2 mg mL^{-1} graphene oxide layer on the surface of the working gold electrode. This illustrates 50 µm of a graphene oxide large sheet that can form a uniform layer in most areas despite the roughness (micron

scale features) of the gold electrode surface. In comparison to drop-casting which is typically used in electrochemically modified electrodes, this method provides more reproducibility and enables formation of much larger areas of GO films without agglomeration. Figure 3-3B shows two-dimensional AFM images of a graphene oxide flake with wrinkles. These wrinkles can be produced during vaporization of the solvent during spin coating.

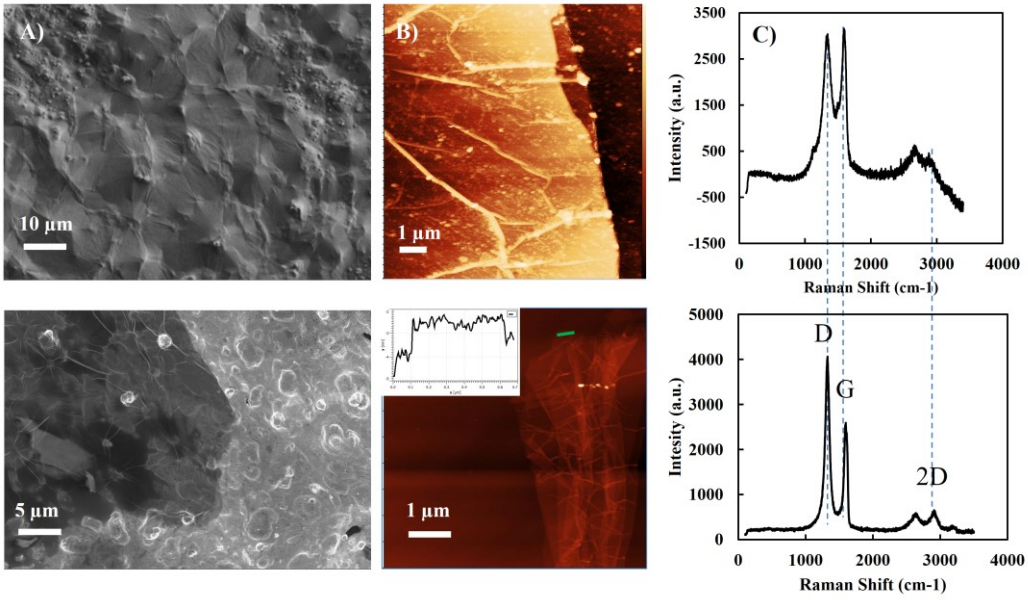

Figure 3-3. A) SEM image of GO thin film on gold electrode surface, B) 2 and 3D Atomic force microscopy images on glass slide. C) Raman spectrum of GO (top), and rGO (bottom) image.

We tested and characterized both graphene oxide and reduced graphene oxide films to determine which of the two has better performance in detection of lead. Thus, we used

electrochemical reduction of the GO films, and the quality of reduction was investigated using Raman spectroscopy. Figure 3-3C shows the Raman spectrum of graphene oxide and the electrochemically reduced film. The most important features in the Raman spectra for assessment of graphene oxide reduction are the G and D peaks. These peaks arise from vibration of sp^2 carbon and appear around 1600 and 1340 cm^{-1} respectively. The overtone of the D peak appearing around 2700 cm^{-1} is called the 2D peak. Unlike mechanically exfoliated graphene, the GO 2D band usually has low intensity because it is more disordered. Therefore, the peaks that can be used to distinguish between GO and rGO are the G and D peaks and their ratio. Also the G peak of GO and rGO with respect to graphene and graphite gets shifted into higher frequencies (1600 cm^{-1}) because of defects in the film. This ratio exhibited a significant increase compare to GO (from 0.98 to 1.57). This shows restoration of sp^2 carbon and a decrease in the average size of sp^2 domains after electrochemical reduction of GO. The increasing in intensity of the 2D peak also suggests better graphitization [132].

In order to explore the activation of the modified working electrode, the electrochemical performance was evaluated using differential pulse voltammetry (DPV). As shown in Figure 3-4A and 3-4B, an increase in concentration of spin coated GO solution increases the current intensity in response to 10 ppm of lead standard solution. Also, the current intensity exhibited from GO electrodes is higher compared to that of rGO, likely because the interaction between oxygen functionalized groups with lead ions. The data suggest that among the different working electrodes we fabricated, the spin coated GO film (concentration of 2 mg mL^{-1}) exhibits the fastest electron transfer rate for lead ions.

We electrochemically characterize the electrode film using an inner sphere redox probe,

potassium ferrocyanide. Figure 3-4C shows representative data of cyclic voltammogram obtained for an unmodified gold SPE and also various spin coated GO films. The gold SPE exhibits a pair of well-defined redox peaks, with a peak-to-peak separation of 78 mV. The peak separation can be used to determine hetero-electron transfer (HET) rate. In the case of linear mass transfer, smaller separation of the peaks indicates increasing reversibility and higher HET rate. Electrochemical characterization of the GO thin films exhibits an increasing peak separation with respect to the concentration of GO suspension. The peak separations for GO solution concentrations between 0.2-2 mg mL^{-1}, range from 82 to 176 mV. The electrochemical response of graphene based electrodes towards the ferrocyanide redox probe is influenced by the density of states near the Fermi level and more significantly by surface morphology and the presence of oxygenated species [133].

To further characterize the electrochemical performance of the device, we also performed electrochemical impedance spectroscopy (EIS). Nyquist plot for the electrodes are shown in figure 3-4D. The shape of plot depends on the applied voltage. All impedances were biased to the redox voltage of ferrocyanide, which was 0.115 V. The charge transfer resistance (R_{ct}) values (based on real part of the impedance in EIS measurements) are in agreement with the cyclic voltammograms response. With increasing GO concentration HET decreases and R_{ct} increases to higher values. Also, 2 mg mL^{-1} GO shows higher (constant phase element) CPE, indicating a rougher surface in this case.

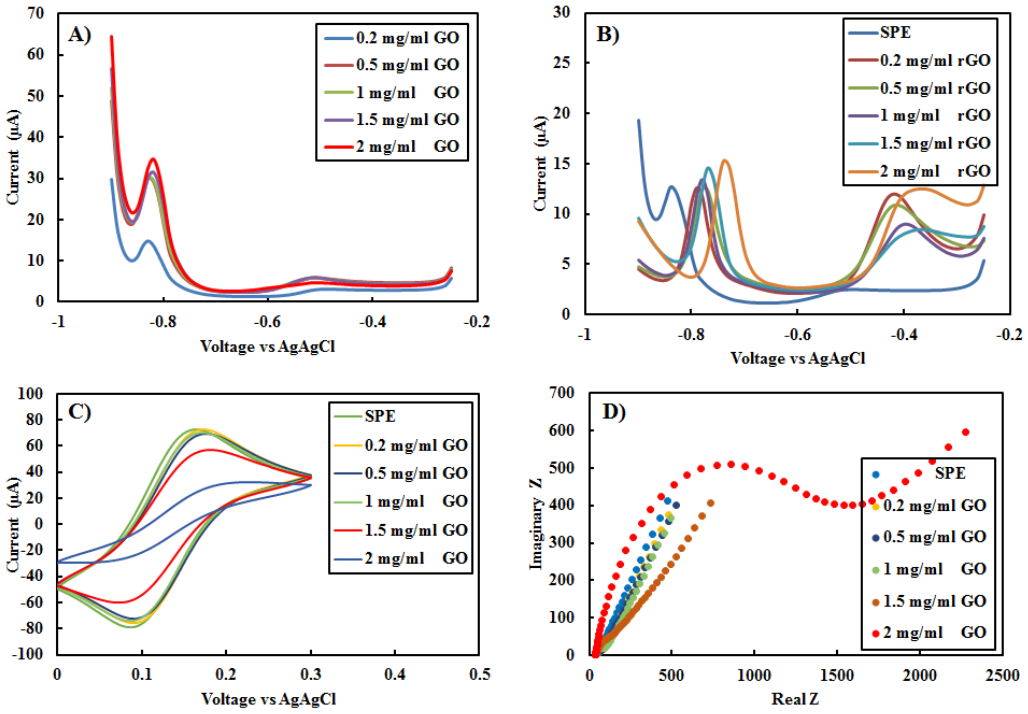

Figure 3-4. A, B) Diffirential pulse voltammograms obtained for different GO and rGO concentration electrodes respectively. DPV performed from -0.9 to -0.2 V, with step size 10 and pulse size 50 mV in 10 ppm lead in 0.1 M acetate buffer (pH 5). C) Cyclic voltammograms of different GO concentrations electrodes in 5 mM $K_3Fe(CN)_6$ in 0.1 M KCl. Scan rate is 20 mvs^{-1}. D) Electrochemical impedance curves in 5 mM $K_3Fe(CN)_6/K_4Fe(CN)_6$, 0.1 M KCl. The spectra were taken at 0.1 Hz to 1 MHz, 0.115 v dc vs Ag/AgCl.

The comparison of results from GO and rGO show the oxygen groups on the surface of GO, as expected, play an important role in detection of lead ions. Although the electron transfer of GO in ferrocyanide is lower compared to normal SPEs and rGO electrodes, a higher current response with respect to lead ions is observed. Various electrolytes were tested to find the optimal buffer for lead analysis. Among them, HCl and KCl react very aggressively with the electrodes and destroy them. Also HNO_3 has a large peak in -0.4 V that covers up the lead peak, especially in the low concentration range, and makes the detection of lead impossible. Between PBS (pH 7) and acetate (pH 5), acetate has better

performance and lower background current and as a result, 0.1 M acetate buffer with pH 5 was selected for measurement of lead concentrations.

3.3.2. Sensor Response in Lead Standard

The cyclic voltammogram (CV) of the electrodes was obtained using a lead standard solution of 100 ppm at a scan rate of 50 mV s^{-1} (figure 3-5). A redox peak corresponding to the lead ion appeared in -0.68, -0.74 V. Based on the difference between the cathodic and anodic peak location, the electrode shows a quasi-reversible response towards lead ions. When performing up to 20 scans, the peak location and intensity, after the second scan remains consistent, showing the stability of the electrode surface for lead ions even in the presence of very high concentrations of lead. Figure 3-5B shows the differential pulse voltammetry (DPV) peak increasing with the concentration of lead. This gives us confidence that this peak results from the presence of lead ions and not nitrate, which is in the lead standard solution.

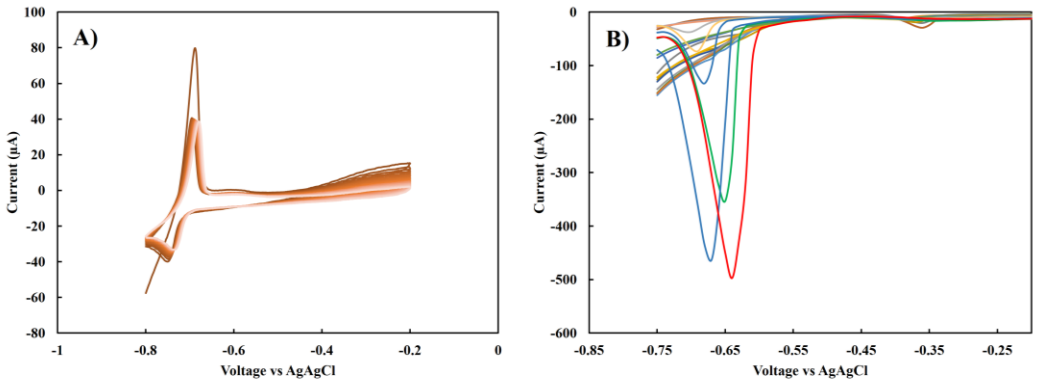

Figure 3-5. A) 20 scans of cyclic voltammograms of 100 ppm lead solution in 0.1 M acetate buffer. B) Differential pulse voltammograms in 0-100 ppm lead concentration in 0.1 M acetate buffer. Step size 10 and pulse size 50 mV.

As SWASV (Square Wave Anodic Stripping Voltammetry) has proven to be a powerful electrochemical method for sensing heavy metal ions, we selected this as our electrochemical method in this work. First, we studied the effect of the most important SWASV parameters, namely accumulation potential, time, the number of pulses, and the applied frequency.

As shown in figure 3-6, when we ramped up the pulse amplitude to 50 mV, the peak current plateaus and afterward it stays steady as the pulse amplitude is increased. Also, the peak current response of GO SPE electrode was measured at different frequencies. After 30 Hz, the peak splits into two peaks so 20 Hz is selected for the measurements. The peak current gradually increased with accumulation time until 240 s. The maximum peak current was obtained in deposition voltage of -1 V. However, because of the over-potential involved during reduction of hydrogen on the surface of the electrodes, lower voltages are desirable for the purpose of long-term usage. As our final goal is designing portable sensor in the bucket of sediment and performing the in-situ measurement, all SWASV analysis have been done in stationary and ambient condition. The response in this condition shows enough sensitivity for the low concentration range of lead detection.

After calibration of SWASV parameters, the analytical performance of the lead GO-SPE was explored by SWASV. Figure 3-7A, B show SWASV measurements conducted from -0.85 to -0.4 V vs Ag/AgCl in acetate buffer (pH 5) for a wide range of lead ion concentrations (2 ppb-20 ppm). The peak current appeared between -0.75 and -0.66 V. At low concentration levels, which are the range of interest for sediment analysis, the corresponding peak appeared at -0.75 V. The data has been corrected based on base line current.

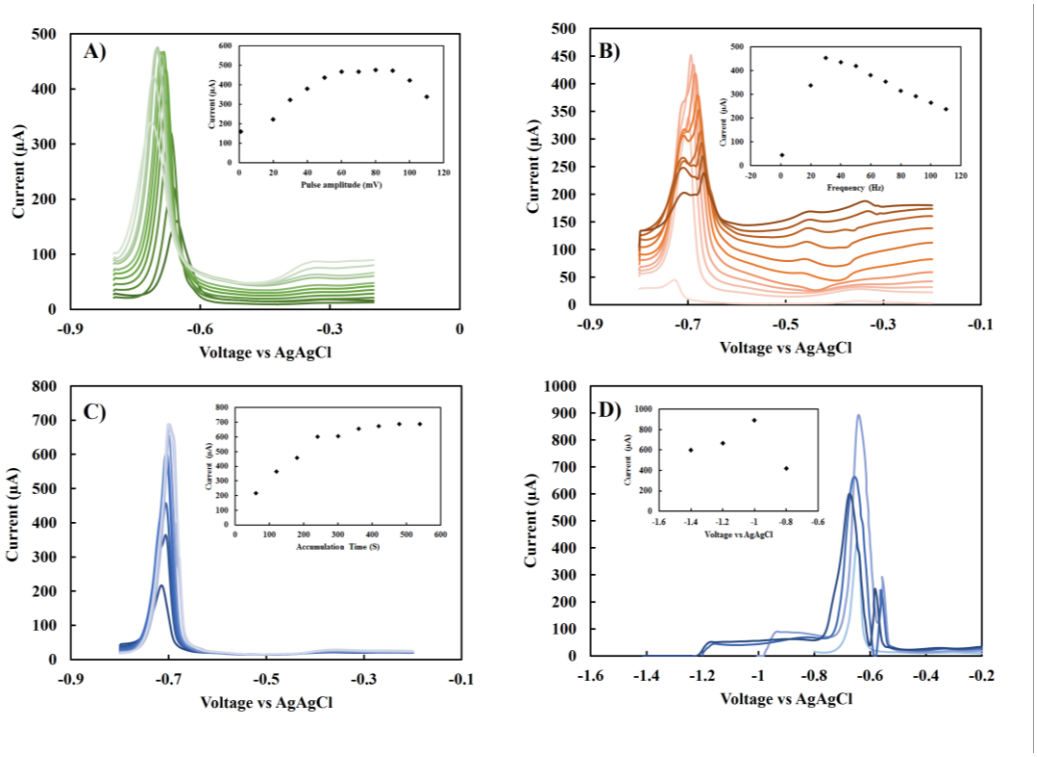

Figure 3-6. A, B, C,D) Square wave anodic stripping voltammograms of different pulse amplitude, frequency, accumulation time and accumulation voltage. Lead concentration was used is 20 ppm in 0.1 M acetate buffer (pH 5).

Figure 3-7C, D shows the calibration curves, indicating the presence of two linear ranges. To calculate the sensitivity of the sensor towards lead ions, the effective surface area was obtained using the Randles-Sevcik equation. Based on the slope of the current verses the square root of the scan rate in 5 mM $K_3Fe(CN)_6$ in 0.1 M KCl, the active surface area for spin coated 2 mg mL^{-1} of GO on top of the SPGE is equal to 0.025 cm^2. On the basis of this area, the fabricated sensor shows a sensitivity of 1.73 µA ppb^{-1} cm^{-2} in low and 1.9 µA ppb^{-1} cm^{-2} in the high concentration range with a low detection limit of 4 ppb. The steady peaks in very high concentration levels indicates that the surface of GO is not saturated so we can assume the bond between oxygen functional group on the surface of GO with lead ions is reversible and this sensor can be reused multiple times.

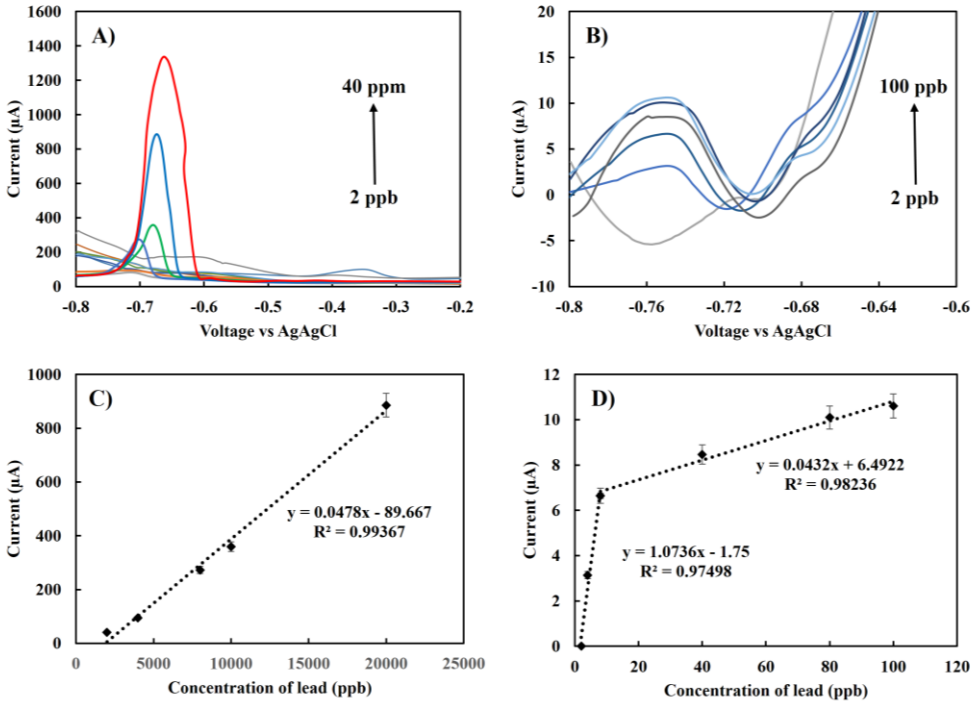

Figure 3-7. A,B) Square wave anodic stripping voltammogram of different range of lead standard solution in acetate buffer (0-40 ppm). Pulse size is 50 mV, frequency 20 Hz, accumulation time 240 s. C, D) Calibration curve for different concentration range of lead standard solutions.

3.3.3. Lead Detection in Sediment Samples

After testing the performance of the fabricated sensor on lead standard solutions, we turned our attention to characterize the ability of the sensor to detect lead concentrations in contaminated complex environmental samples.

3.3.3.1 Spiked Sediment Samples

First, we tested the sensor's ability to detect lead in water extracted from contaminated sediment. Before testing for basal levels of lead in processed environmental sample, we tested environmental samples spiked with lead to study the effect of the matrix on the

sensor. First, 10 µl of standard lead solution was spiked into untreated water extracted from the sediment, but no peak was observed, even despite adding high concentrations of lead. To resolve this issue, we added acetate buffer into the matrix. Figure 3-8 shows the SWASV response of the sensor in the range of 2 ppb-20 ppm, spiked at a 1:1 ratio of standard solution in acetate in water, which was extracted by centrifuge from the sediment samples. The magnitude of the redox current generated for 20 ppm is four times lower than the lead standard in purified acetate buffer. The results show that the water extracted from the sediment has a significant effect on inhibiting the lead redox currents. The inset shows a range of 2-1000 ppb, which is the range of interest for the lead in sediment samples. Based on the data obtained, we concluded that the presence of acetate buffer is crucial to detection of lead in sediment samples.

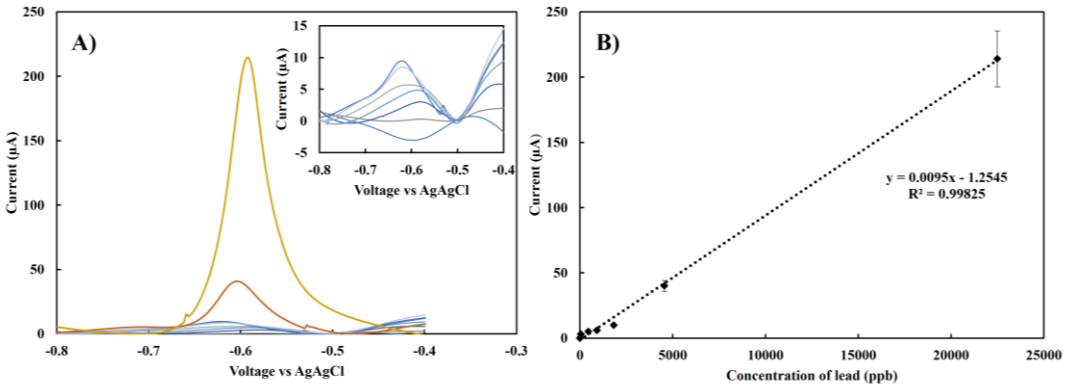

Figure 3-8. A, B) Square wave anodic stripping voltammograms of different range of lead standard solution in water extracted from sediment/acetate buffer (0-20 ppm)(1:1 ratio). C, D) Calibration curve for different concentration range of lead standard solutions

3.3.3.2. Off-Chip Sample Preparation

For measurement of basal concentrations of lead ions adsorbed to sediment, the sediment must first be digested with nitric acid to convert the various types of lead compounds to Pb (II). 1 gr Sediment (0.9 gr after water evaporation) was dispersed in nitric acid and then filtered using Whatman filter paper (Figure 3-9A). Ultrasound was used for 1 hour in 60º C in three different concentration of nitric acid. Figure 3-9B shows the SWASV peaks for lead in a 1:1 ratio of digested sediment in nitric acid/acetate buffer. Among various concentrations, 0.1 M nitric acid was chosen based on peak current intensity and the need for a less aggressive solution on the electrode surface.

To quantify the amount of lead, SWASV was performed for different lead standard solutions in the same electrolyte composition used for digestion (1:1 ratio 0.1 M nitric acid/acetate buffer). The results are shown in figure 3-9C. Finally, we performed the digestion without using ultrasound in room temperature. Figure 3-9D shows the average result for three different measurements of samples with RSD 10%. The peak intensity is significantly higher than before, which was unexpected, however this phenomenon can be explained with the concept of adding residues of sediment during ultrasonication that can passivate the surface of the electrode. Based on the calibration data, the amount of lead in this sample is approximately 21±2 mg kg^{-1} of sediment, which is comparable with the range of lead in sediment reported in previous studies [23, 134].

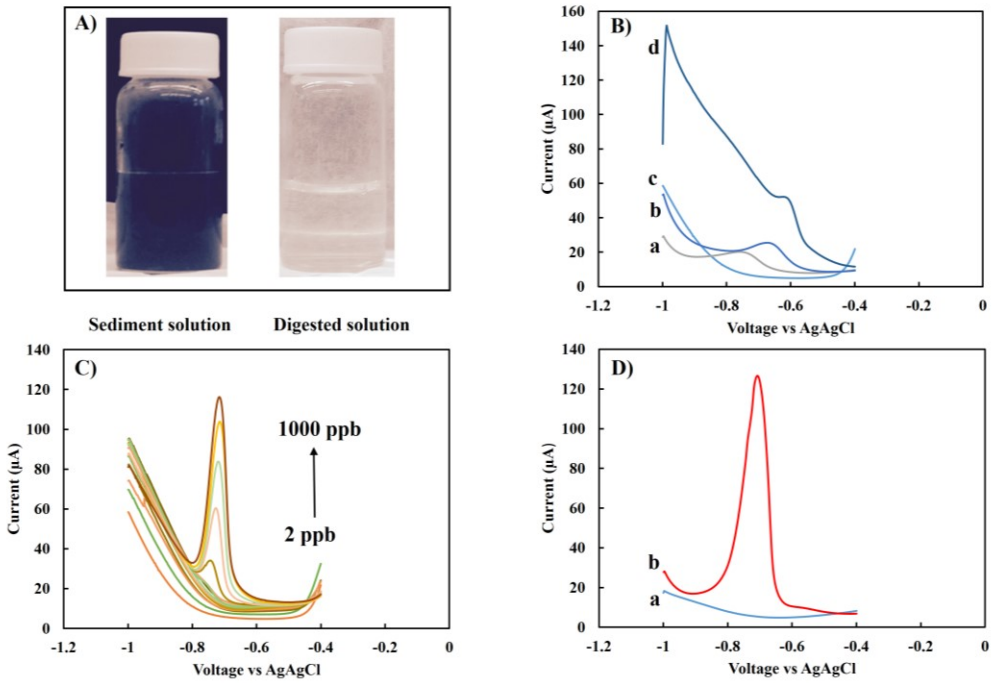

Figure 3-9. A) Solution of sediment in nitric acid before and after filtration. B) Effect of concentration of nitric oxide using ultrasound digest in 60 degrees a) digested in 0.1 M nitric acid, b) 0.2 M nitric acid. c) blank buffer solution 0.2 M nitric acid/acetate buffer, d) 0.3 M nitric acid C) SWASV peaks for different concentration of lead standard solution in 1:1 nitric acid and acetate buffer. D) SWASV peaks for a) 0.1 M nitric acid/acetate buffer blank, b) digested lead in 0.1 M nitric acid/acetate buffer.

3.3.3.3. On-chip sample preparation

After determining the appropriate reagents and conditions for sediment digestion, lead extraction, and purification, we focused our efforts on miniaturization and integration of sample-preparation on-chip. The filter paper and cellulose sponge was assembled on top of the GO sensor (figures 3-10B, C). Then amount of 0.1 grams sediment was injected onto the surface of the cellulose sponge (figure 3-10D). Nitric acid (0.1 M) was manually injected onto the sediment, thus extracting lead ions, which then diffused to the acetate buffer below the membrane. This allowed for the lead ions to be suspended in an optimal

buffer (acetate) for detection purposes. The lead ions continue to diffuse further until they reach the GO sensor and get detected. Figure 3-10D shows the average result of SWASV measurement using this integrated sample-to-answer set up. This initial result was very encouraging showing that integrated sample preparation was feasible, however, we moved towards an integrated fluidic system to minimize the need for manhandling and manual injection of reagents.

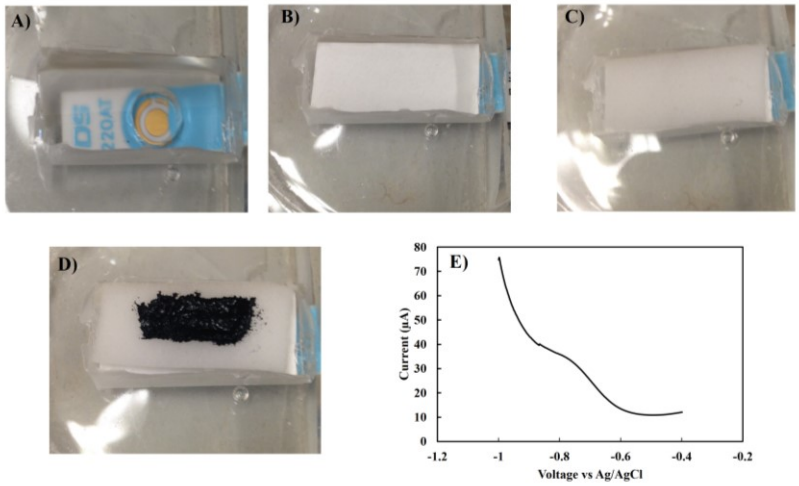

Figure 3-10. A) GO thin film on SPE electrode with PDMS membrane, B) adding filter paper C) adding sponge, D) adding sediment sample, E) the SWAVS response of sensor set up

As a result, the design was modified to incorporate precise microfluidic control to enable automation. To allow sufficient time for sediment digestion and minimize user manhandling of reagents, a column was used to introduce sediment and nitric acid to the device (figure 3-11A). In addition, this design effectively decreases the volume of nitric acid (which is hazardous) required to the microliter range. Moreover, separate inlet and outlets added to the set up that allow user to more precise control the ratio of reagents. They are located as follows: The nitric acid inlet is located at the top of the column. The outlet is located in middle of the PDMS hole. The inlet of the acetate buffer is located on

top of the hole. With this design, reagents are introduced at a (1:1) ratio to help obtain reproducible results comparable to those obtained from calibration experiments. Figure 3-11B shows the result of the lead measurement obtained with this set up for 0.45 grams of dried sediment. Results are compared with traditional pretreatment methods revealing 80 percent peak recovery (figure 3-11C,D).

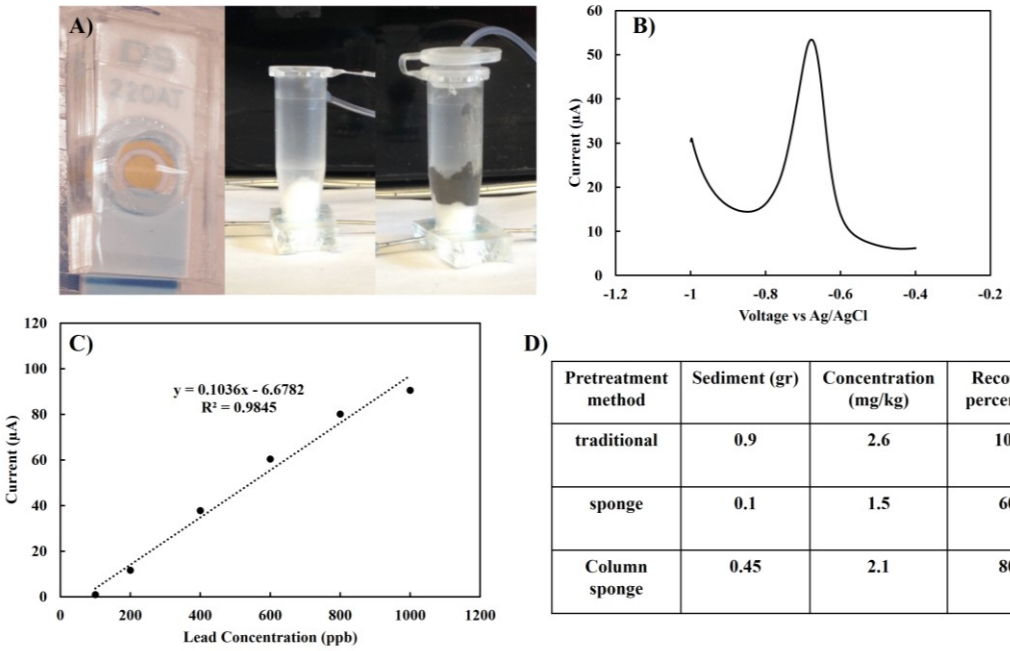

Pretreatment method	Sediment (gr)	Concentration (mg/kg)	Recovery percentage
traditional	0.9	2.6	100
sponge	0.1	1.5	60
Column sponge	0.45	2.1	80

Figure 3-11. A) column based pretreatment set up, B) SWAVS response of column based compact electrochemical lead sensor, C) Calibration curve for (1:1) nitric acid: acetate after baseline correction, D) comparing results for different pretreatment approaches based on calibration curve.

Here, we introduced an integrated sample-to-answer platform capable of analyzing heavy metal ions in complex samples like sediment. The results demonstrate that this approach shows promise for an in-situ platform capable of continuously monitoring heavy metal concentrations complex environmental samples such as sediment in natural water sources. Though we focused on sediment, we emphasize the applicability of this platform

to perform sample-to-answer analysis in other complex matrices such as soil and food [69, 70]. The approach presented in this manuscript use a considerably shorter time for digestion sediment compared to off-chip pretreatment methods. Further improvement can be made to the design presented here by incorporating a closed-feedback loop based input set up. This set up allows the sediment exposes several times to the same volume of nitric acid, thus dramatically increasing the exposure time.

3.4. Conclusions

An integrated miniaturized, sample-to-answer electrochemical sensor system based on graphene oxide has been developed, calibrated and tested in both standard lead solutions and complex sediment samples. This work shows that square wave stripping voltammetry based electrochemical detection of lead is a promising analytical tool for monitoring heavy metals in complex matrices, and this work can fill the current gap for on-line heavy metal monitoring electrochemical based system in natural water sources.

In this study, we utilized the outstanding electrochemical properties of graphene oxide thin films with respect to lead ions to fabricate a label-free method for measurement of low abundance toxic metals in sediment samples. We systematically optimized modification of the electrodes and the electrochemical measurement parameters in buffer solution, which allows us to measure the presence lead in low abundance. The sensitivity of the sensor was 1.73 $\mu A\ ppb^{-1}\ cm^{-2}$ in the range of 0-100 ppb and 1.9 $\mu A\ ppb^{-1}\ cm^{-2}$ in 100 ppb to 20 ppm with a low detection limit of 4 ppb. We tested the performance of the sensor both in environmental samples spiked with lead (to test the effect of the matrix), and we also tested basal levels of lead in digested sediment. Then we introduced a portable pretreatment set-

up as an ultra-compact fully nitrated sample-to-answer system. This sensor showed the ability to quantify low abundance heavy metals in sediment. We envision miniaturizing the potentiostat used to readout the electrochemical sensor into a portable instrument resulting in a low cost rapid field analyzer capable of sample-to-answer analysis simultaneously with collection of sediment, which can be an alternative to expensive and time-consuming methods such as atomic adsorption and Inductively Coupled Plasma Mass Spectrometry.

Chapter 4: Results for magnetic microfluidic valve

4.1. Introduction

In this research, we present a magnetically actuated microfluidic transistor (valve), an on-chip micro-valve that uses magnetorheological fluids micropatterned onto an elastomeric membrane to develop an ultra-compact solution for digital control of microfluidic circuits. We simulated the micro-valves theoretically and also characterized micro-fabricated devices experimentally. We simulated effects of channel and valve geometry on the deformability of the valve. We experimentally characterized the effects of channel and valve geometry on the ability to reversibly close channels fully. We characterized the microfabricated valves in the flow rate range of 0.02 to 1 μl/min. Among the various kinds of valves examined, for lower flow rates, circular valves with 700 μm diameter in 300 μm width channel, and in higher flow rates rectangular valves 700 μm wide in same channel show the best ability in terms of valve closure and response time. The fabrication and integration of the proposed valve is compatible with a range of polymer microfabrication technologies having the advantage of simple fabrication, small size, and no external power requirement. These valve structures can be promising solutions for pumping and active flow control for portable analytical instrumentation, point-of-care diagnostic devices, and even wearable microfluidic devices.

In addition, we present a low power and simple designed microfluidic liquid handling system, which is enabled by combining elastomeric membrane and electropermanent magnet. Placing two millimeter sized rods of hard and semi hard magnetic bars assemble electropermanent magnet with a current carrying coil around them. A short current pulse

is applied to the coil, which creates or eliminates the externally available magnetic field. The elastomeric membrane is either attracted or repelled by this magnetic field to open and close the valve. The fabricated valve consumes mJ of energy per actuation with no energy needed between actuation. Using this configuration, we demonstrate on demand controlling transportation in V-shape configuration channels. To evaluate the flow performance of the valve, internal changing in flow rate is examined by passing micrometer beads and compared the results with permanent magnet.

4.2. Permanent magnet based microfluidic valve

4.2.1. Fluidic device fabrication

A three-layer micro-magnetic valve was fabricated using the following procedure (figure 4-1). First, a layer of SU-8 with 12 μm thickness (measured with profilometer) is spun onto a 3" silicon wafer. The patterns of the desired valve structures are transferred into this layer (figure 4-1A). Then an air bubble free mixture of 10:1 weight ratio of sylgard silicon elastomer and curing agent spun onto the mold with a spin rate of 4000 rpm. The thickness of this membrane is 15±2 μm (figure 4-1B).

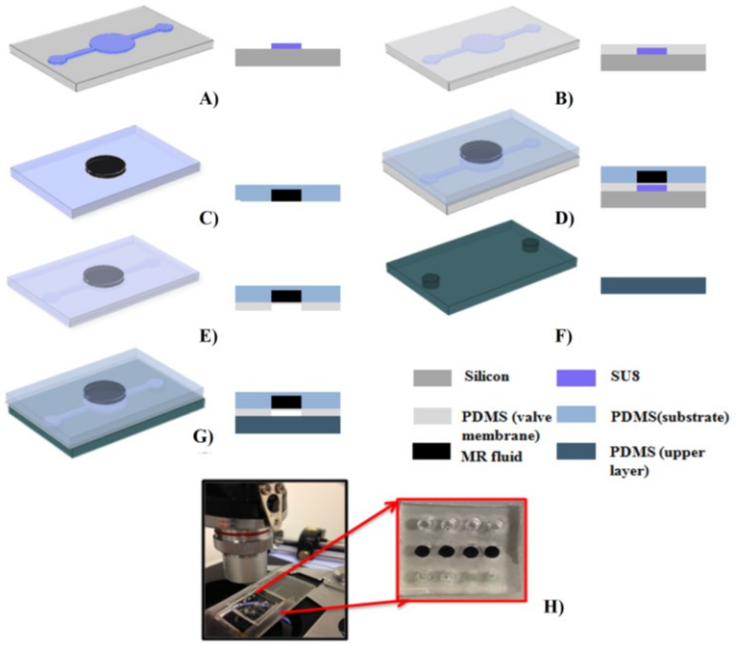

Figure 4-1. Fabrication steps of valves. A) Fabrication mold on silicon wafer, B) spin coat of PDMS on mold, C) fabrication of PDMS substrate layer contain hole to fill MR fluid, D) bonding PDMS substrate layer to spin coated PDMS membrane with activation of oxygen plasma, E) remove the mold from the structure, F) fabrication of PDMS upper layer contain inlet and outlet, G) bonding all three layers together, H) sample of fabricated device contain four different kind of valves [101].

After curing at 80°C for two hours, a substrate 2 mm layer thick PDMS layer with a through-hole for the MR fluid is bonded (figure 4-1C) to the PDMS membrane using oxygen plasma bonding (figure 4-1D). The whole PDMS structure is then peeled off from the silicon master mold wafer (figure 4-1E) and bonded using oxygen plasma to the top of a 1 mm thick PDMS layer serving as the base substrate. The 1 mm thick PDMS layer is fabricated with a 5:1 ratio of PDMS to curing agent to stiffen the layer to avoid collapsing with the PDMS membrane. The inlet and outlet is punched through the membrane and the 2mm thick layer (figures 4-1F,G). Finally, the MR fluid (please provide vendor information here), with a concentration of 10 mg/ml was injected into the miniature hole above the roof of the valve membrane. Also, an N52 permanent magnet with a 3900 Gauss magnetic flux

density was used to actuate the valve. For proof-of-concept purposes, we used a permanent magnet, however we emphasize that there are a broad variety of miniaturized electronically actuated micromagnets that can be used for valve actuation. Figure 4-1H shows the image of a microfabricated device containing four different valve structures in various opened and closed states. In order to characterize the performance of the valve and its ability to open and close microchannels and impede flow rate, we injected a suspension of 3 μm polystyrene beads into the flow channel, and optically monitored the flow rate in the channel, by acquiring images using a bright field microscope, in the channel and tracking the velocity and position of the beads. Fluid was injected into the flow layer channel and flow rate was controlled using a syringe pump.

4.2.2. Results

4.2.2.1. Valve simulation

We studied and modeled the valve actuation process using the finite element method (COMSOL Multiphysics) with the intention of gaining an understanding of the behavior of the proposed device with relation to various parameters such as valve geometry and dimensions, thus providing an approximate design space to give guidance for our microfabrication and experimental characterization efforts. We considered major factors affecting membrane deformation including (i) channel width, (ii) valve shape, and (iii) valve size.

A 3D dimensional model was created. The model contains the permanent magnet (N52 with a magnetic flux density of 3900 Gauss), three PDMS layers: Layer 1) iron particles, Layer 2: valve channel, and Layer 3: the substrate suspended in air. The magnetic

properties of the simulation elements were incorporated in the form of relative magnetic permeability. The magnetic field distribution obtained from this model was used to calculate the applied force on valve membrane and it was applied as input to the structural model formed by valve membrane and fluidic channel. The amount of deformation was obtained using the fluid structure interaction module. This model geometry consists of a horizontal flow channel a with valve membrane on top. The valve membrane, a deformable material, bends under the applied magnetic force load. The Navier-Stokes equations for incompressible laminar flow describe the flow in the channel. At the channel entrance, the flow has fully developed laminar characteristics with a speed of 100 μm/s. At the channel output, the boundary condition is zero pressure. On the solid walls, no-slip condition is imposed; also symmetry is assumed at the central vertical plane of the horizontal channel. Figure 4-2A shows the simulation result of the cross-sectional and a bird's eye view of the deformed valve membrane for two kinds of rectangular and circular shaped valves. The membrane thickness is chosen to be 15 μm, which is the same dimension we chose for the microfabricated valves. For comparison, the micrograph of the bird's eye view of the micro-fabricated valve with the same dimensions is shown (figure 4-2B). A membrane with the same thickness and length, however differing in width can result in various deflection shapes as well as sagging heights due to the applied field. Figure 4-2C shows the simulation results for two different sized (600 and 700 μm) circular and rectangular shaped valves with respect to different channel widths. The amount of deformation is higher in the case of rectangular valves compared with circular valves of the same size. The area of rectangle is larger than circle, thus the amount of MR fluid on top of the rectangle is greater, and thus a higher magnetic force is exerted for a given field, thus

making the deformation of the rectangular valve larger compared to the circle. These effects are predominant in valves of larger dimensions thus in the case of 700 μm a more noticeable difference can be seen between them.

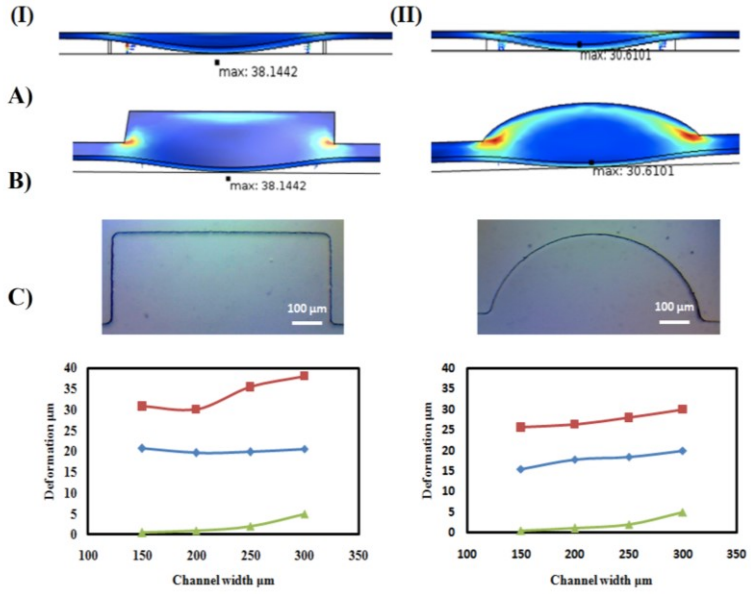

Figure 4-2. I) Rectangle based valve, II) Circle based valves A) simulation result for deformed valve B) fabricated valve, C) effect of different parameters in the amount of deformation [101].

Using the simulation results to provide design guidance for experimental efforts, valves were microfabricated and validated experimentally. Rectangular and circular shaped valves with different channel widths were fabricated and their operational performance was compared with each other. Figure 4-3 shows a series of qualitative images to visualize the ability of the microfabricated valves to open and close channels.

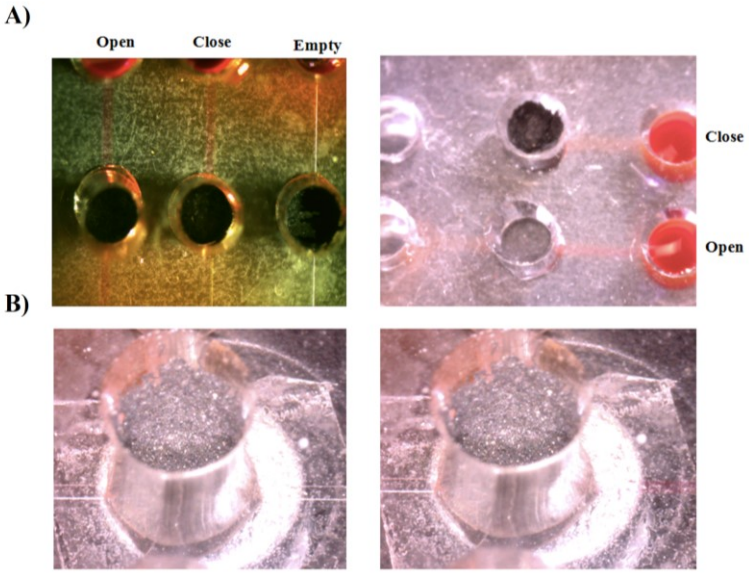

Figure 4-3. A) top view B) cross section view of different conditions of valve [101]

Valves can be closed, as seen (figure 4-3A, B), without affecting the neighboring valve. Thus, the PDMS membrane, with MR fluid on top, can be effectively magnetically closed as predicted by simulations, and can function effectively and be contactless opened and shut. The amount of membrane deformation and thus valve closing depends on membrane thickness, channel width and height, valve geometry, and concentration of the MR fluid. Among these parameters, we focused on studying the effect of channel width and valve geometry for optimizing valve performance.

4.2.2.2. Effect of shape and size of valve on its performance

We fabricated valves with various dimension including 300-150 µm width, and 1 cm length. Circular and rectangle valves (600 µm and 700 µm diameters and side width) were embedded.

To characterize the fluid flow in the channel, we injected polystyrene beads into the fluid, and monitored the channels optically, recording the video of the channel. The position of the beads was tracked optically to determine the average flow rate in the channel. The flow of beads was controlled with syringe pump and magnet was applied and removed in 30-second intervals. The difference in the speed of the beads was recorded. Then the videos were converted to image frames, and the speed of beads was calculated before and after applying the magnet. To make the data comparable with the simulation results, here we set the syringe pump flow rate to 0.02 µl/min, which is equivalent to an average fluid speed of 100±15 µm/s, which was the same assumption made in the simulation regarding the speed of the fluid at the inlet. Each of dot obtained in the figures of the experimental results is from averaging the speed of five different beads.

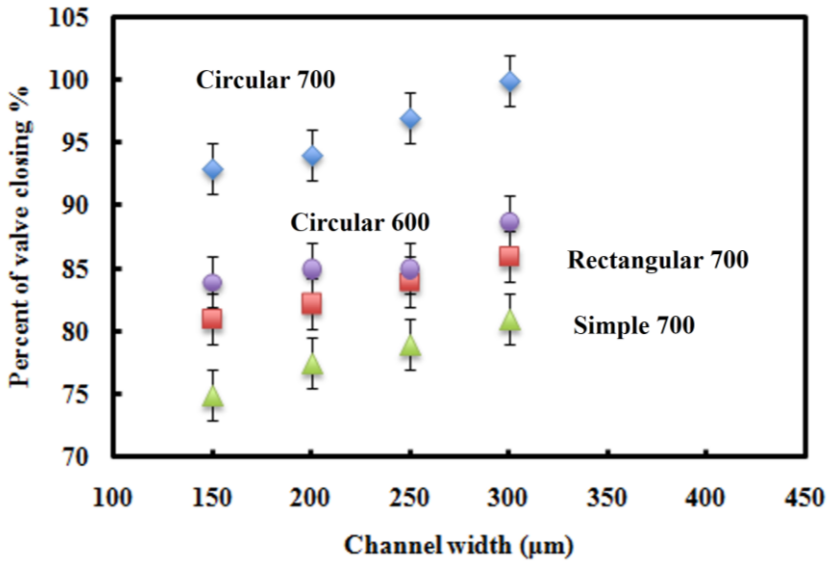

Figure 4-4. Effect of size and type of valves on the amount of closing of valve, each point was obtained from two different valves for average of five different beads speed. Diamond is for circle with 700 µm diameter, circle is for circle with 600 µm diameter, square is for rectangle with 700 µm side and triangle is for simple channels with different channel widths. The flow rate in the channels was 0.02 µl/min [101].

Figure 4-4 shows the percentage of valve closure for various configurations. We approximate valve closure by calculating the drop in fluid velocity before and after applying a magnetic field. In the case where the fluid comes to a complete stop, we assume 100% valve closure. The magnetic field applies a force on the MR fluid and causes deformation of the thin PDMS membrane layer and stops fluid flow in the channel reducing the flow rate to zero. As we expected from the simulations, simple channels (valves without a circle or square beneath the patterned MR region) have lower deformation and circular valves with a diameter of 700 μm has the greatest deformation. A decrease in channel closure with smaller channel width was also observed experimentally. However, there is an essential difference between experiment and simulation for rectangular valves. In spite of the fact that rectangular valves have highest deformation because of its geometry compared to a circle, more dead volume lies in the valve, thus it cannot become completely closed, which becomes especially apparent in low flow rate regimes. We discuss differences between circular and rectangular valves in more detail in the next section.

4.2.2.3. Response of valve versus flow rate

In order to evaluate the response of different valve structures in different flow rate regimes, the percentage of valve closure for channels with 300 μm width for three types of valves, circular and rectangle (700 μm diameter, side width) and a simple channel (meaning that the full 1 cm channel was 300 μm wide throughout) was studied.

Fig. 4-5 shows the percentage of valve closure in response to the pressure applied to the channel in the valve region. In the low flow rate regime, the circular valve can be

completely closed, however as fluid flow rate (or applied pressure) increases, its performance degraded much more rapidly compared to rectangular valves.

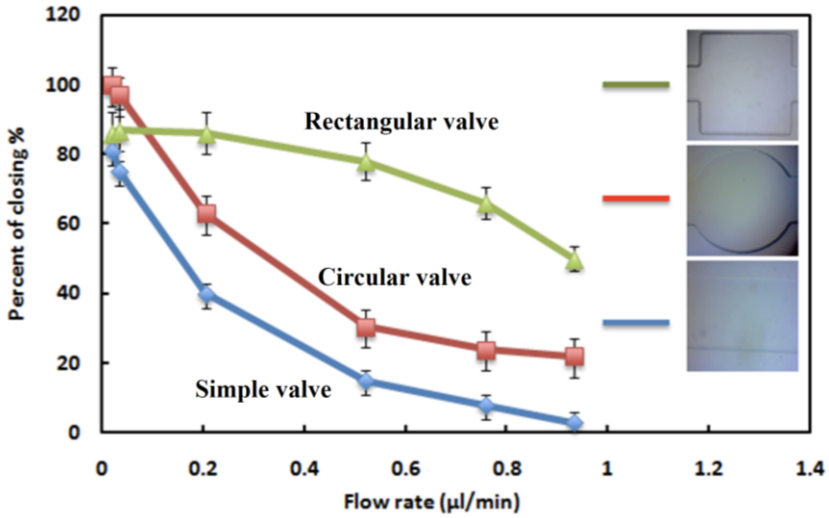

Figure 4-5. The response of different kind of valves to different pressure in channel. The amount of closing valve for circle (rectangle) and rectangle (triangle) and simple 300 µm valve (circle) [101].

The rectangular valve can operate with roughly the same performance for a wider range of flow rate. As can be seen, the rectangular channel is reduces the fluid speed by nearly 86% as the bead velocity drops from 900±50 µm/s to 220 µm/s. For the same flow rate, the circular valves and the simple valves respectively close 63% and 40%.

4.2.2.4. Analysis on-off cycles

To evaluate the ability for the valve to switch flow in the channel on and off, we tested on-off cycles of valves. In other word, the magnetic field was applied for 30 seconds closing the valves, and removed for 30 seconds allowing the valve to reopen. Here, the speed of beads was recorded for three open/close cycles. In order to obtain the precise flow rate of the fluid in the channel, we calculated flow rate based on the fluid speed, rather than

relying on the reading provided by the syringe pump, which can often be inaccurate. Figure 4-6 shows the fluid flow rate in the channel versus time for three valve On-Off cycles.

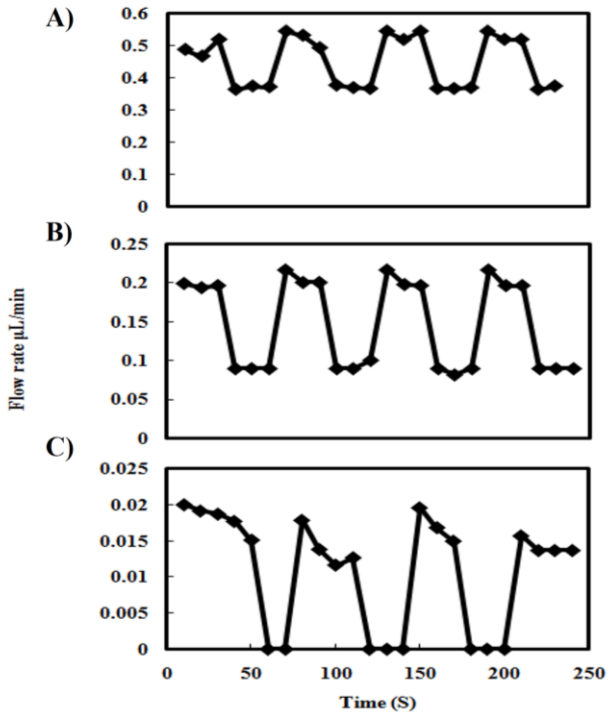

Figure 4-6. On-Off cycles for three times of operating circle type valve with 700 µm diameter. A,B,C) For flow rates of 0.5, 0.2,0.02 µl/min of channel during applying magnet respectively [101].

. When the magnet was applied, the flow rate in the channel dropped significantly with a rapid response time, and after the magnetic field was removed, returned near to its original level. For the case of 700 µm diameter circular valve with a channel width of 300 µm, the continued application of magnet for 30 second in flow rate of 0.02,0.04 µl/min, causes complete valve closure and for a flow rate of 0.2 µl/min, a valve closure of 60 percent and a flow rate drop to 0.08 µl/min.

This was repeated reproducibly over several cycles. Hence, we can expect this valve to operate effectively in applications that require repeated opening and closing over long periods of time. Various applications exist where it is important to have a system of flow

control that can exhibit instantaneous closure and rapid reopening. Thus, we believe these valves are suitable candidates for these applications.

4.3. Electropermanent magnet based microfluidic valve

4.3.1. Fluidic device fabrication

Microfluidic chips were made of three layers of PDMS (Sylgard 184, Dow Corning) using standard soft lithography (figure 4-7). The SU-8 mold was patterned on a silicon wafer and then the microfluidic channel layer (10±2 μm thickness) was casted onto the wafer by spin coating a 10:1 (v/v) ratio of base to curing agent with a spin rate of 4000 rpm and cured for 1 hours in 80˚C. The thickness of this membrane is 15±2 μm. A 2 mm top layer with an embedded tiny disc magnet (1.5 mm diameter) was bonded to the channel membrane with oxygen plasma bonding. The whole structure was then peeled off from the silicon master mold wafer and bonded to the substrate layer. The substrate polymeric layer has the thin layer part with 100 μm thickness and a width of 3 mm to minimize the distance between the EPM and the valve.

4.3.2. Electropermanent magnet assembly

We fabricated and assembled the EPM based on the design previously developed by Knaian [103]. The schematic of EPM set up shows in figure 4-8. The ferromagnetic poles were cut from a 0.014” thick Hiperco 50 coil (Ed Fagan Inc. Franklin Lakes, NJ). This Iron-Cobalt-Vanadium alloy has ideal magnetic properties such as low coercivity and low A.C. core loss that allows fast magnetic switching with minimum lost. High magnetic saturation of this material grants the poles to magnetize to the full amount of the magnetization without saturation. Two cylindrical magnets (2 mm diameter × 3 mm length)

with same remnant magnetization but different coercivity were used. Sintered Neodymium Iron Boron Magnet (NdFeB model N38SH) and cast Aluminum Nickel Cobalt (Alnico grade LNG40) (BJA Magnetics, USA) were utilized as the hard and soft magnet

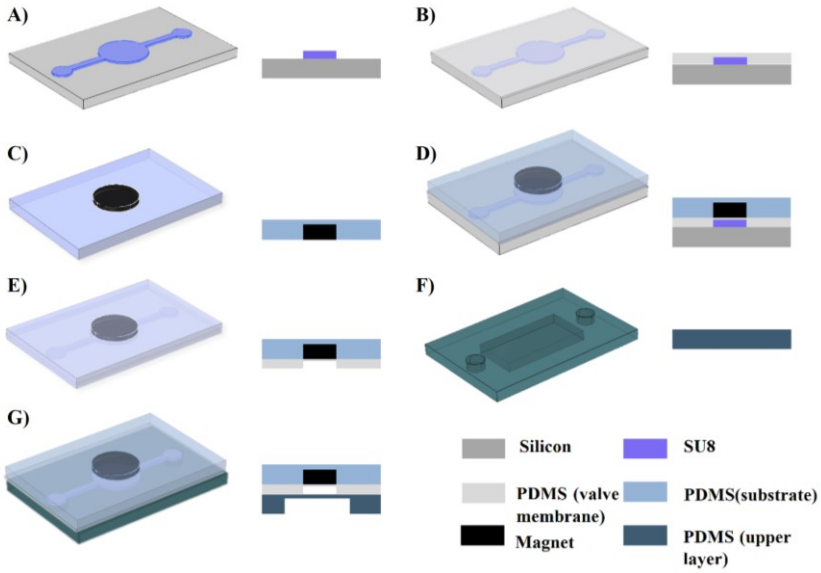

Figure 4-7. Microfluidic valve fabrication steps. A) Soft lithographic patterning of SU-8 mold (flow channel pattern) on a silicon wafer, B) Spin coating of PDMS on the mold, C) fabrication of PDMS substrate layer contains hole to embed tiny magnet, D) bonding PDMS substrate layer onto the spin coated PDMS membrane using oxygen plasma bonding, E) removing the two PDMS layers from the mold, F) fabrication base PDMS layer to hold the EPM, G) bond all three layers together with oxygen plasma.

respectively. The hard magnet has a coercivity (H_c) of 907 kA/m and a remnant magnetic field (B_r) of 1.22 T and the soft magnet has a coercivity (H_c) 44 kA/m and a remnant magnetic field (B_r) of 1.2 T. The pole pieces and the two magnets were assembled using Loctite Hysol E60-HP epoxy adhesive (Henkel, Westlake, OH). Mechanical pressure was applied over night to make fully active the bond of the EPM pieces together. A 40 AWG magnetic wire (MWS Wire Industries) was used to make the coil.

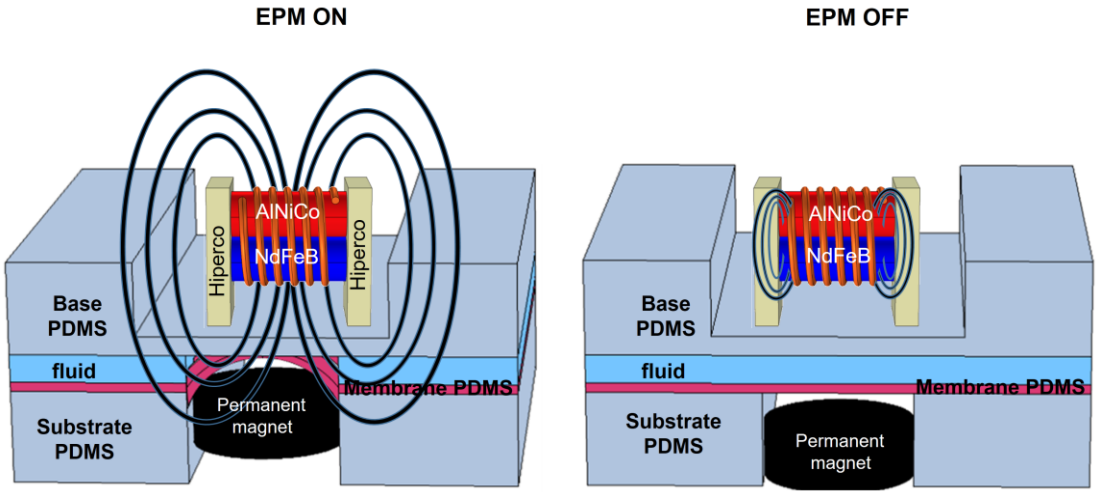

Figure 4-8. Schematic of the concept of electropermanent magnet (EPM) integrated with elastomeric membrane. Applying a short current pulse can switch ON and OFF the external magnetic field of EPM, attracting or releasing the magnet below the elastomer membrane, thus closing and opening the valve respectively.

4.3.3. Electropermanent magnet characterization

The EPM coil can be represented using an equivalent circuit consisting of an inductor in series with resistance. The resistance of the coil was measured with a digital multimeter that varies with the number of coil turns. The inductance of coil was measured by applying an AC sweep with a function generator and oscilloscope. To switch the EPM (from on to off or vice versa), a short high current pulse is required. A MOSFET H-Bridge circuit, which is commonly used to derive D.C. motors, was used to operate the circuit. The power was supplied from a D.C. power supply. The positive and negative pulse was generated from a function generator and amplified using an amplifier gain stage.

The EPM magnetic response was tested using an H-Bridge configuration circuit. A 120 µs positive current square pulse was applied and amplified to switch ON the EPM and the opposite current pulse was used to turn OFF the external magnetic field of EPM. The DC actuation voltage was applied and the current response was measured with a 0.1 Ω resistor

using the oscilloscope (figure 4-9A). The current response for a 120 turn coil EPM has a 7 μs time constant with a maximum current of 1.84 A. The maximum actuation time of the EPM, defined as $5\tau_{coil}$ [106] , is 35 μs. Figure 4-9B demonstrates the magnitude of the external magnetic field for different applied actuation voltages for the EPM (inset of figure 4-9B) coil with 120 turns. The magnetic field was measured using the Hall-Effect probe of the gaussmeter. To study the magnetic behavior of EPM, voltage was swept from 13 to 30 V. A positive current pulse was used to turn ON the magnet. It shows as blue curve in the figure. And negative current pulse was used to turn OFF the magnet (red curve in the figure 4-9A). The results indicate that between 25-30 V, the pulse has sufficient power to completely switch OFF the external magnetic field. As voltage is increased, the amplitude of the magnetic field in the ON configuration increases. A 13 volt pulse does not carry sufficient power to perform magnetic switching. The magnetic field strength (B field) for the EPM is estimated as 1.3 T and 0.02 T for the ON and OFF stages respectively when the applied switching voltage is 30 V. During the short (15 μs) switching of the EPM, it consumes 55.2 W of power (dynamic) and requires 6.6 mJ energy. The effect of the number of turns of the coil was also investigated. Table 1 shows coil resistivity and maximum current pulse for different coil turns ranging from 80 to 150 and also the corresponding magnetic field intensity for the EPM in the ON and OFF states when applying 30 V.

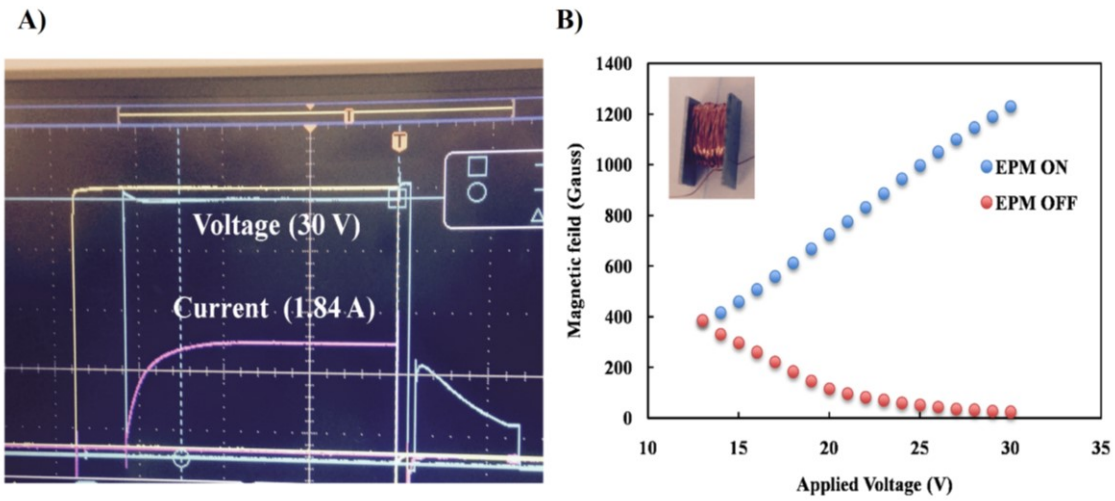

Figure 4-9. A) Oscilloscope image of pulse properties required to Switch EPM magnet. A 120 µs electrical pulse with activation voltage of 30 V is applied to switch an EPM with 120 Coil turns. B) The ON-OFF Characterization of the EPM with respect to the applied voltage. Inset shows the Image of a fabricated EPM (the distance between poles are 3 mm).

Table 4-1. Electropermanent magnet properties

EPM coil turn	EPM properties with applying 30 volt		
	Resistivity (Ohm)	EPM ON, OFF (Gauss)	Current (A)
80	6.4	1070, 97	2.36
100	7.4	1070, 76	2
120	8.2	1230, 24	1.84
150	8.4	1240, 18	1.76

4.3.4. EPM valve testing

To benchmark the performance of the microfluidic EPM valve, we built channel (Y-junction) with two identical circular shaped valves on two of the channels. Fluids of two

different colors (Green and Red food dye) are injected into the two inlets (top of the device figure 4-10). When both valves are open, both fluids flow through the junction resulting in two laminar flow streams moving parallel to each other down the single channel until reaching the outlet. When one valve is closed and the other is open, only a single color of fluid will flow all the way to the outlet. Figure 4-10 shows the steps of valve operation when switching the valve ON and OFF in the top right channel. When a negative current pulse was applied to the EPM, the magnetic force was cancelled and the valve remained open (Figure 4-10C) and upon application of a positive current pulse, the thin membrane became deflected thus closing the valve (Figure 4-10D). We experimentally determined that maximum performance is attained when the EPM is positioned vertically and the edge of the pole is located on top of the active valve area. The insets of Fig. 4-10 show the Y junction area enlarged for various valve states. The thickness of PDMS substrate is thinner on top of the valve compared to the other parts in order to minimize the distance between the EPM and the valve thus maximizing magnetic field on top of the valve area. Capillary flow was the mechanism behind driving the fluid flow in this channel (no syringe pump). We also studied the effect of flow rate and the various modes of syringe pump operation.

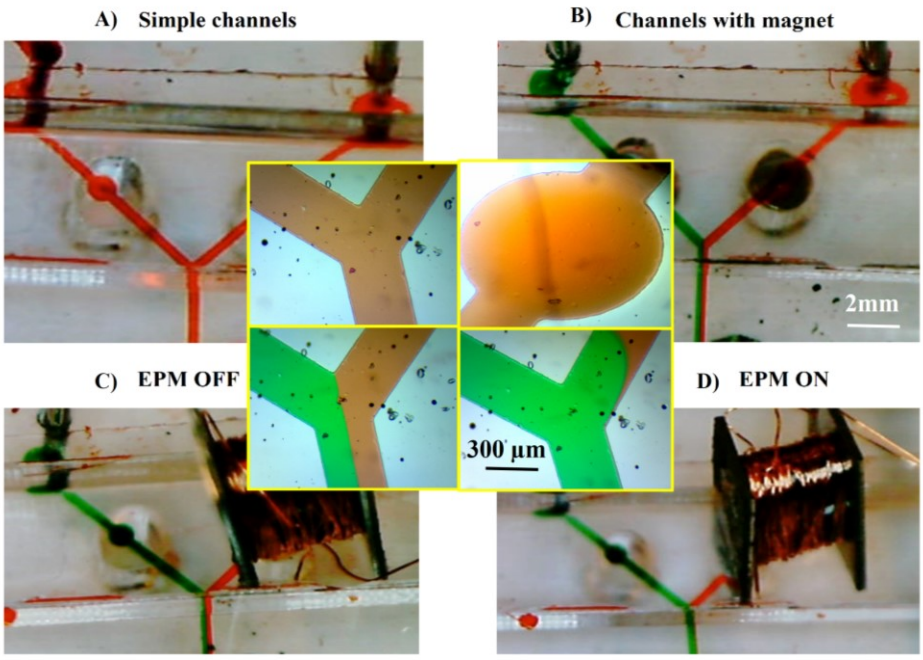

Figure 4-10. A) Image of the 300 µm wide microfluidic channel with circular valves of 700 µm diameter, B) Channels are embedded 1.5 mm magnet, C) Y-junction state when EPM is OFF and top right inlet channel (injecting red fluid) is open, D) Y-junction state when EPM is ON and top right inlet channel (injecting red fluid) is closed.

Figure 4-11 demonstrates the behavior of the valve immediately after applying a positive and negative pulse. Figure 4-11A shows the gradual injection of the green food dye into the junction as the valve in the top right channel is opened. Though the EPM response is on the order of tens of microseconds, the valve response time is on the order of several seconds. The channel width is 300 µm with a height of 12 µm. Each valve is a 700 µm diameter circle. The distance between the Y junction and the valve was 1 cm. A negative pulse was applied to actuate the EPM located on upper right channel valve (red dye) that was initially in closed state. The real time video demonstrating the opening of the valve can be found in supplementary information. For the specific geometry fabricated, the response time for fully opening the valve and allowing fluid to flow through was approximately 6 seconds. Real-time closing of the valve is also demonstrated (Figure 4-

11B). In this case, the valve was initially open and a positive current pulse was applied which turns on the magnetic field of the EPM, thus closing the membrane stopping the red fluid from being injected in, allowing the green dye to fully be injected into the bottom channel towards the outlet. The response time for closing the valve in this configuration is approximately 6 seconds, however the time required to completely evacuate red dye from the main channel (lower left) was approximately 10 seconds. The real time video demonstrating closing of the valve can be found in supplementary information. This performance characterization of valve response time can be insightful for design of chemical reactions inside the channels, particularly when multiple reagents are involved.

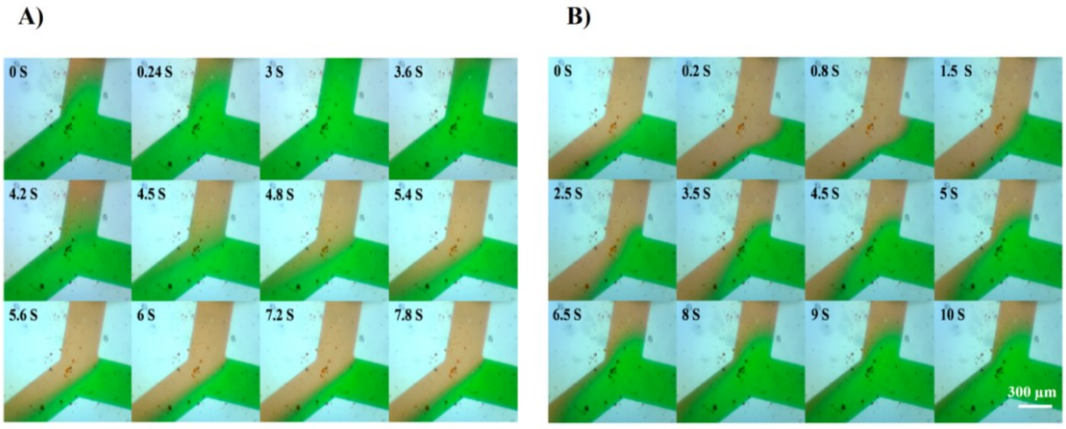

Figure 4-11. A) Time lapse image of valve immediately after applying electrical pulse to EPM controlling top inlet channel allowing red food dye to get injected into junction. B) Time lapse image of valve immediately after applying electrical pulse to EPM closing the top inlet channel preventing red food dye from getting inject. Only the green food dye getting injected from the right inlet channel is fully passing through the junction into the outlet (left channel).

4.3.5. Flow rate characterization of EPM valve

We characterized the ability of the EPM valve to withstand fluid flow in channels of varying flow rates (both fluid withdraw and infusion). The performance of EPMs for

actuating the valve was compared with that of a permanent magnets. We used particle image velocimetry (3 μm beads) to precisely measure the drop in fluid speed inside the channel. To measure the fluid velocity, the suspension of beads was injected using a syringe pump, and the beads were tracked optically. This measurement was obtained for both the ON and OFF state of the EPM (figure 4-12A). The recorded videos were converted to image frames, and the speed of the beads was calculated based on the average of five different measurements. Then the speed of the beads was converted to flow rate based on the cross sectional area of the channel. Figure 4-12B shows the channel flow rate measurements inside the channel for withdrawal mode of the syringe pump in a range of 0.001 to 3 μl/min. In this experiment, a simple rectangular channel was used (instead of Y-shaped channels) to make sure the changing of flow rate is due to the valves ability to fully withstand the applied pressure, rather than the fluid getting diverted to the adjacent channel. The measured flow rate in the channel when the valve was closed was plotted against the flow rate forced by the syringe pump. The results show that the EPM driven valve can fully withstand and completely stop flow as long as the syringe pump is injecting fluid less than 0.2 μl/min. When the syringe pump injects fluid at a flow rate of 0.4 μl/min, the valve remains 80 percent closed. The permanent magnet begins leaking at 0.05 μl/min, but leaks at a slower rate compared to the EPM valve, and can remain 96 percent closed until 3 μl/min.

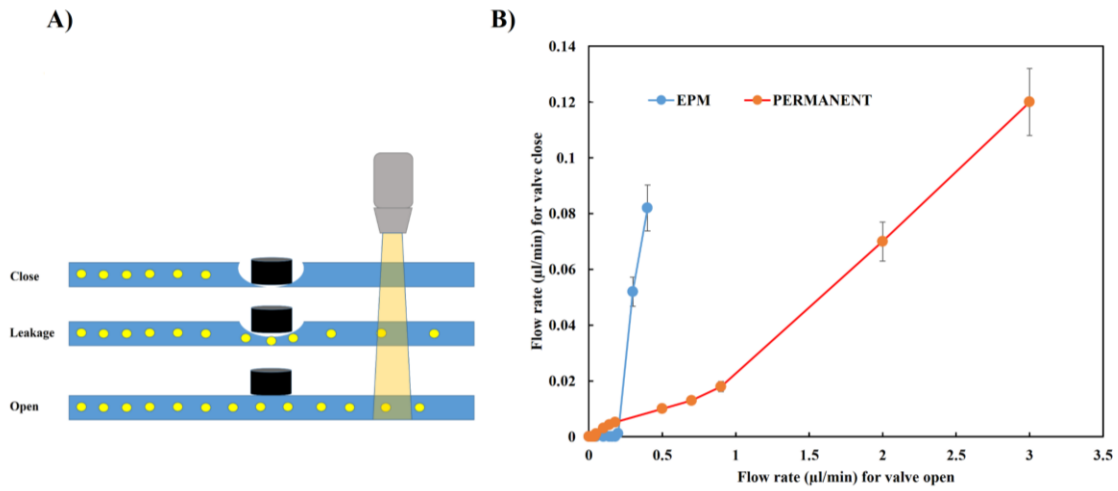

Figure 4-12. A) A schematic of the experimental setup for optically estimating the flow rate in the channel based on particle image velocimetry using 3 µm polystyrene beads. B) The y-axis shows the actual flow rate measured in the channel when the magnetic valve is closed. The x-axis is the flow rate that is being applied by the syringe pump. The performance of EPM and permanent magnet based valves are compared with each other in a simple rectangular channel structure. A syringe pump connected to the output withdraws fluid.

We also studied the Y-shaped channels using food dye in the infusion mode of the syringe pump. Figure 4-13 shows the results for applied flow rate in the range of 3 to 100 µl/min. The top right and the bottom right channels are the inlets. The left channel is the outlet. Fluid flows from right to left. The EPM valve is on in the top right channel. All images were taken after 10 seconds of applying a current pulse into the EPM. Based on these results, this valve can prevent fluid from passing until 60 µl/min, and beyond that the valve no longer withstands the fluid pressure. Most of fluid leakage stems from the edges of the valve. To minimize loss from the edge enabling operation in higher flow rates, additional traps can be fabricated on the four sides of the circular part, thus increase valve operation tolerance.

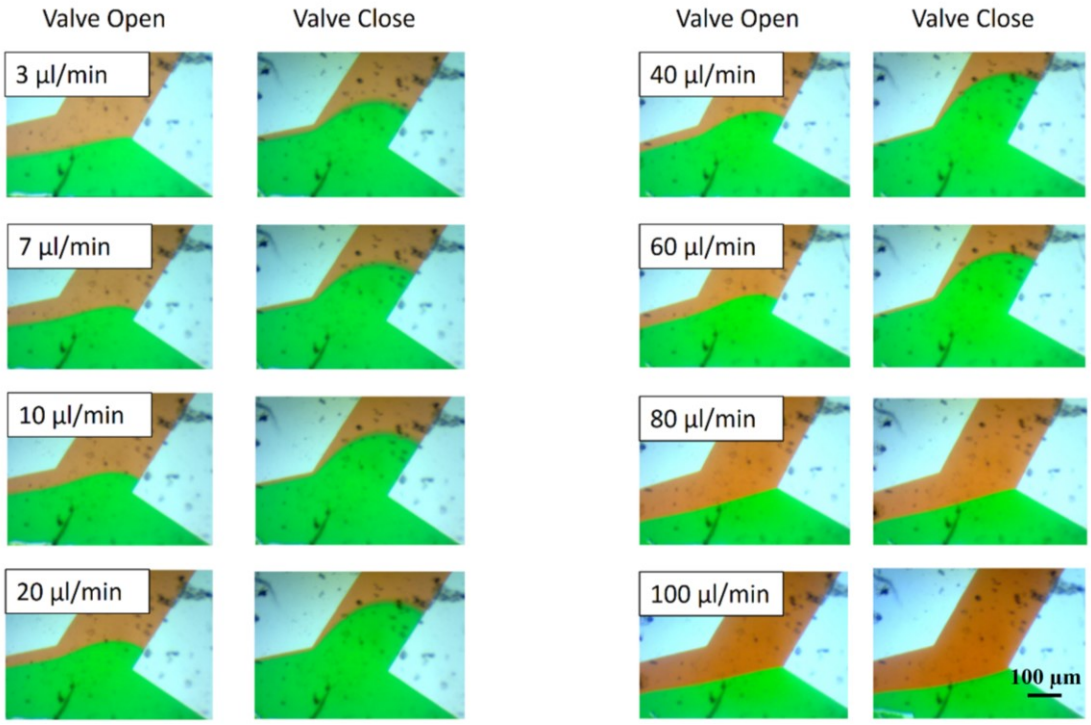

Figure 4-13. Images at different applied flow rates (3 to 100 µl/min) of Y-junction where right channels are inlets and bottom left channel is outlet. Syringe pump is in infusion mode injecting red food dye in top right channel and green food dye in bottom right channel and directing both fluids through the Y-junction to the outlet (bottom left channel). EPM valve is controlling the top channel where red food dye is being injected. For each flow rate, both the EPM ON and EPM OFF scenarios are visualized.

4.4. Conclusion

In this work, we designed, simulated, and fabricated a novel method for magnetically actuating elastomeric valves with a fast response time. Our fabrication process is advantageous because of its compatibility with standard soft-lithography processes, allowing for microfluidic users to easily integrate this technique in their design. We performed COMSOL simulations to aid with our understanding of the parameters effecting valve performance, and we validated the theory by fabricating and experimentally characterizing the proposed valve structures. In general, the operating range of flow rate

that we tested for the fabricated valves was relatively low (< 1 μl/min) because we used a 1 mm thick PDMS layer as the base substrate between the magnet and PDMS membrane.

The magnetic force exerted on the membrane decreases exponentially as the distance from the valve increases. Thus, for future work, we can overcome this limitation by using substrates that are thinner to achieve a closer distance to the membrane. Although the operating flow rate/pressure range of these valves is relatively (low it can be simply improved with using very thin layer of PDMS substrate only in active side of valve. Future work to improve the performance of these valves can include designing novel geometries with minimal amounts of dead volume, yet maintaining a high level of deformability. Also the range of active flow rate of valve can be controlled with changing the thickness of substrate PDMS and concentration of MR fluid based on our application needs. However, we emphasize, that these valves can have applicability in a wide range of applications in microfluidics requiring low fluid flow rates, such as on-chip protein and nucleic assays. Also, by fabricating several valves in the same channel, in series to each other and actuating them sequentially to enable peristaltic motion, and on-chip fluid pump can be fabricated. The contactless nature of the magnetic actuation also allows envisioning a two dimensional array of electrically controlled micro-magnets under a grid of microchannels. The micromagnetics can actuate the grid of microchannels, and move around the fluids, performing the assay as desired, and then once completed, the channel can be disposed of, and a new grid of channels can be placed on the reusable magnet array. Thus, these valves are attractive candidates not only in realizing large-scale microfluidic integration, but also miniaturizing the footprint of the instrumentation as a whole.

In addition, we designed and fabricated a low power method for electronically controlled magnetic actuation of elastomeric valves suitable for a wide range of microfluidic applications. Our fabricated process is advantageous because it is compatible with standard soft lithography processing and PDMS microfluidic channels widely used in the lab on a chip community. This allows for microfluidic designers to easily integrate this technique in their chip fabrication. Electropermanent magnets offer the electronic control of electromagnets, without the high power consumption requirements, while exhibiting the strong magnetic force of permanent magnets. As previously demonstrated, EPM control circuits with low power consumption can be realized using supercapacitors, thus making these novel valve structures suitable for integration into point-of-care microfluidic devices. To enable practical integration into a network of microfluidic channels, a 3D printed package can be developed for holding an array of electropermanent magnets, upon which the microfluidic channel substrate can be placed. Future efforts will be dedicated to building an array of EPMs and enabling on-chip peristaltic pumping and control of several channels for development of domain specific sample-to-answer systems. To enable large-scale fluidic integration, further miniaturization of the valves using micro-machining and microfabrication techniques can be explored. Integration of the magnetic actuator with the microfluidic channel by microfabrication of the EPM can enable large scale integrated systems. These valves are attractive candidates in long-term reservation and multiple reaction based microfluidic devices.

Chapter 5: Conclusion

This research proposes development of high sensitive electronic sensors to monitor trace amount of biomarkers and environmental hazardous materials using in-situ measurements.

To achieve sensitive sensor, we take advantage of graphene oxide electrochemical properties. Study of respiratory inflammation using monitoring of nitrite has been selected for healthcare application. In environmental, we focus on detection of lead in natural sediment samples. Results show outstanding properties of reduced graphene oxide are useful to fabricate enzyme-free sensor that proved capable of detecting nitrite in EBC clinical samples in the biological range. In next step, standardization of fabricated sensor performed respect to sample collection, storage and electrical parameters of EBC samples. Moreover, the fabricated sensor combined with microfluidic system to have integrated sensor with sample collection of EBC samples.

Interaction between oxygen groups of graphene oxide and lead creates sensitive sensor for detection lead in sediment samples. Less aggressive pretreatment process compare to current reported methods has been developed in this research for electrochemical detection of lead in complex sediment samples. In situ set up was developed for combining pretreatment method with sensor to fabricate device in use system for monitoring lead in natural water sources.

For further integration of fabricated sensors, microfluidic is the good candidate. One of the important fluid-handling components to enable fully miniaturized micro total analysis system (microTAS) is integrated valve. In this research, we propose magnetic low power valve design that can be combining with fabricated sensors to get fully integrated system.

Results show, MR fluid with PDMS thin membrane can act as micro-channel valve in the presence of permanent magnet. Circle with diameter of 700 μm configuration indicates better performance in opening and closing of valve. In next step, permanent magnet replaced with electropermanent magnet (EPM). EPM helps us to control opening and closing of valve with very short electrical pulse. Moreover, this valve will be integrated with microfluidic sensor for nitrite detection in EBC samples.

The results of this study have been published and presented in following journal and conferences:

Journal papers:

Gholizadeh, Azam, et al. "Toward point-of-care management of chronic respiratory conditions: Electrochemical sensing of nitrite content in exhaled breath condensate using reduced graphene oxide." *Microsystems & Nanoengineering* 3 (2017): 17022.

Gholizadeh Azam, et al. Towards point of use environmental monitoring: electrochemical detection of lead in sediment samples from natural water sources using graphene oxide submitted.

Gholizadeh, Azam, and Mehdi Javanmard. "Magnetically actuated microfluidic transistors: Miniaturized micro-valves using magnetorheological fluids integrated with elastomeric membranes." *Journal of Microelectromechanical Systems* 25.5 (2016): 922-928.

Conferences:

Azam Gholizadeh, Damien Voiry, Cliff Wiesel, Howard Kipen, Robert Laumbach, Manish Chhowalla, and Mehdi Javanmard, Measurement nitrite level in exhaled breath condensate samples using electrochemical reduced graphene oxide based sensor. Presented in Hilton head workshop 2016, South Carolina, USA, 2016.

Azam Gholizadeh, Damien Voiry, Cliff Wiesel, Howard Kipen, Robert Laumbach, Manish Chhowalla, and Mehdi Javanmard, Electrochemical Detection of Nitrite Content in Exhaled Breath Condensate Using Reduced Graphene Electrodes. Presented in Biosensors 2016, Gothenburg, Sweden, 2016.

Azam Gholizadeh, Sakshi Sardar, Kathleen Black, Clifford Weisel, Robert Laumbach, Howard Kipen, Andrew Gow, Mehdi Javanmard, Nanomolar Detection of Lung Metabolites in Exhaled Breath Condensate Using Reduced Graphene Oxide Sensor: A Study of the Effects of Sample Matrix and Storage Conditions. Presented in 2017 MRS Fall, Boston, USA, 2017.

Azam Gholizadeh, Mehdi Javanmard, Micro-magnetically controlled valves for ultra-compact integrated micro-total analysis systems, presented in microTAS 2016, Dublin, Ireland, 2016.

References:

[1] American Academy of Allergy Asthma & Immunology. *ASTHMA STATISTICS*. Available: http://www.aaaai.org/about-aaaai/newsroom/asthma-statistics

[2] S. A. Kharitonov, "Exhaled markers of inflammatory lung diseases: ready for routine monitoring?," *Swiss medical weekly,* vol. 134, pp. 175-192, 2004.

[3] G. M. Mutlu, K. W. Garey, R. A. Robbins, L. H. Danziger, and I. Rubinstein, "Collection and analysis of exhaled breath condensate in humans," *American journal of respiratory and critical care medicine,* vol. 164, pp. 731-737, 2001.

[4] I. Horvath, J. Hunt, and P. Barnes, "Exhaled breath condensate: methodological recommendations and unresolved questions," *European Respiratory Journal,* vol. 26, pp. 523-548, 2005.

[5] B. Gaston, J. M. Drazen, J. Loscalzo, and J. S. Stamler, "The biology of nitrogen oxides in the airways," *American journal of respiratory and critical care medicine,* vol. 149, pp. 538-551, 1994.

[6] P. E. Silkoff, S. C. Erzurum, J. O. Lundberg, S. C. George, N. Marczin, J. F. Hunt, *et al.*, "ATS workshop proceedings: exhaled nitric oxide and nitric oxide oxidative metabolism in exhaled breath condensate," *Proceedings of the American Thoracic Society,* vol. 3, p. 131, 2006.

[7] C. Francoeur and M. Denis, "Nitric oxide and interleukin-8 as inflammatory components of cystic fibrosis," *Inflammation,* vol. 19, pp. 587-598, 1995.

[8] Q. Hamid, D. R. Springall, J. Polak, V. Riveros-Moreno, P. Chanez, J. Bousquet, *et al.*, "Induction of nitric oxide synthase in asthma," *The Lancet,* vol. 342, pp. 1510-1513, 1993.

[9] A. Gholizadeh, D. Voiry, C. Weisel, A. Gow, R. Laumbach, H. Kipen, *et al.*, "Toward point-of-care management of chronic respiratory conditions: Electrochemical sensing of nitrite content in exhaled breath condensate using reduced graphene oxide," *Microsystems & Nanoengineering,* vol. 3, p. 17022, 2017.

[10] B. Balint, S. Kharitonov, T. Hanazawa, L. Donnelly, P. Shah, M. Hodson, *et al.*, "Increased nitrotyrosine in exhaled breath condensate in cystic fibrosis," *European Respiratory Journal,* vol. 17, pp. 1201-1207, 2001.

[11] S. Cunningham, L. Ho, A. Greening, and T. Marshall, "Measurement of inflammatory markers in the breath condensate of children with cystic fibrosis," *European Respiratory Journal,* vol. 15, pp. 955-957, 2000.

[12] R. A. Dweik, S. A. Comhair, B. Gaston, F. B. Thunnissen, C. Farver, M. J. Thomassen, *et al.*, "NO chemical events in the human airway during the immediate and late antigen-induced asthmatic response," *Proceedings of the National Academy of Sciences,* vol. 98, pp. 2622-2627, 2001.

[13] N. Adarsh, M. Shanmugasundaram, and D. Ramaiah, "Efficient reaction based colorimetric probe for sensitive detection, quantification, and on-site analysis of nitrite ions in natural water resources," *Analytical chemistry,* vol. 85, pp. 10008-10012, 2013.

[14] H. Wu, S. Fan, W. Zhu, Z. Dai, and X. Zou, "Investigation of electrocatalytic pathway for hemoglobin toward nitric oxide by electrochemical approach based on protein controllable unfolding and in-situ reaction," *Biosensors and Bioelectronics,* vol. 41, pp. 589-594, 2013.

[15] J. L. Heinecke, C. Khin, J. C. M. Pereira, S. n. A. Suárez, A. V. Iretskii, F. Doctorovich*, et al.*, "Nitrite reduction mediated by heme models. Routes to NO and HNO?," *Journal of the American Chemical Society,* vol. 135, pp. 4007-4017, 2013.

[16] S. Wang, Y. Yin, and X. Lin, "Cooperative effect of Pt nanoparticles and Fe (III) in the electrocatalytic oxidation of nitrite," *Electrochemistry communications,* vol. 6, pp. 259-262, 2004.

[17] J. Davis and R. G. Compton, "Sonoelectrochemically enhanced nitrite detection," *Analytica Chimica Acta,* vol. 404, pp. 241-247, 2000.

[18] M. A. Kamyabi and F. Aghajanloo, "Electrocatalytic oxidation and determination of nitrite on carbon paste electrode modified with oxovanadium (IV)-4-methyl salophen," *Journal of Electroanalytical Chemistry,* vol. 614, pp. 157-165, 2008.

[19] S. Radhakrishnan, K. Krishnamoorthy, C. Sekar, J. Wilson, and S. J. Kim, "A highly sensitive electrochemical sensor for nitrite detection based on Fe2O3 nanoparticles decorated reduced graphene oxide nanosheets," *Applied Catalysis B: Environmental,* vol. 148, pp. 22-28, 2014.

[20] N. Zhou, J. Li, H. Chen, C. Liao, and L. Chen, "A functional graphene oxide-ionic liquid composites–gold nanoparticle sensing platform for ultrasensitive electrochemical detection of Hg 2+," *Analyst,* vol. 138, pp. 1091-1097, 2013.

[21] N. Zhou, H. Chen, J. Li, and L. Chen, "Highly sensitive and selective voltammetric detection of mercury (II) using an ITO electrode modified with 5-methyl-2-thiouracil, graphene oxide and gold nanoparticles," *Microchimica Acta,* vol. 180, pp. 493-499, 2013.

[22] Y. Wei, C. Gao, F.-L. Meng, H.-H. Li, L. Wang, J.-H. Liu*, et al.*, "SnO2/reduced graphene oxide nanocomposite for the simultaneous electrochemical detection of cadmium (II), lead (II), copper (II), and mercury (II): an interesting favorable mutual interference," *The Journal of Physical Chemistry C,* vol. 116, pp. 1034-1041, 2011.

[23] Z. Zhang, M. Li, W. Chen, S. Zhu, N. Liu, and L. Zhu, "Immobilization of lead and cadmium from aqueous solution and contaminated sediment using nano-hydroxyapatite," *Environmental Pollution,* vol. 158, pp. 514-519, 2010.

[24] U. ATSDR, "Toxicological profile for lead (Atlanta, GA: US Department of Health and Human Services, Agency for Toxic Substances and Disease Registry (ATSDR), Public Health Service)," *US EPA (2006) Air quality criteria for lead,* 2007.

[25] M. Ghaedi, A. Shokrollahi, K. Niknam, E. Niknam, S. Derki, and M. Soylak, "A cloud point extraction procedure for preconcentration/flame atomic absorption spectrometric determination of silver, zinc, and lead at subtrace levels in

environmental samples," *Journal of AOAC International,* vol. 92, pp. 907-913, 2009.

[26] D. Citak and M. Tuzen, "Cloud point extraction of copper, lead, cadmium, and iron using 2, 6-diamino-4-phenyl-1, 3, 5-triazine and nonionic surfactant, and their flame atomic absorption spectrometric determination in water and canned food samples," *Journal of AOAC International,* vol. 95, pp. 1170-1175, 2012.

[27] M. Soylak, E. Yilmaz, M. Ghaedi, M. Montazerozohori, and M. Sheibani, "Cloud point extraction and flame atomic absorption spectrometry determination of lead (II) in environmental and food samples," *Journal of AOAC International,* vol. 95, pp. 1797-1802, 2012.

[28] R. Sitko, P. Janik, B. Feist, E. Talik, and A. Gagor, "Suspended aminosilanized graphene oxide nanosheets for selective preconcentration of lead ions and ultrasensitive determination by electrothermal atomic absorption spectrometry," *ACS applied materials & interfaces,* vol. 6, pp. 20144-20153, 2014.

[29] S. Caroli, G. Forte, A. Iamiceli, and B. Galoppi, "Determination of essential and potentially toxic trace elements in honey by inductively coupled plasma-based techniques," *Talanta,* vol. 50, pp. 327-336, 1999.

[30] S. Munro, L. Ebdon, and D. J. McWeeny, "Application of inductively coupled plasma mass spectrometry (ICP-MS) for trace metal determination in foods," *Journal of Analytical Atomic Spectrometry,* vol. 1, pp. 211-219, 1986.

[31] L. Zhao, S. Zhong, K. Fang, Z. Qian, and J. Chen, "Determination of cadmium (II), cobalt (II), nickel (II), lead (II), zinc (II), and copper (II) in water samples using dual-cloud point extraction and inductively coupled plasma emission spectrometry," *Journal of hazardous materials,* vol. 239, pp. 206-212, 2012.

[32] G. Pelossof, R. Tel-Vered, and I. Willner, "Amplified surface plasmon resonance and electrochemical detection of Pb2+ ions using the Pb2+-dependent DNAzyme and hemin/G-quadruplex as a label," *Analytical chemistry,* vol. 84, pp. 3703-3709, 2012.

[33] R. Choudhary, S. Patra, R. Madhuri, and P. K. Sharma, "Equipment-Free, Single-Step, Rapid,“On-Site” Kit for Visual Detection of Lead Ions in Soil, Water, Bacteria, Live Cells, and Solid Fruits Using Fluorescent Cube-Shaped Nitrogen-Doped Carbon Dots," *ACS Sustainable Chemistry & Engineering,* vol. 4, pp. 5606-5617, 2016.

[34] A. Malon, T. Vigassy, E. Bakker, and E. Pretsch, "Potentiometry at trace levels in confined samples: ion-selective electrodes with subfemtomole detection limits," *Journal of the American Chemical Society,* vol. 128, pp. 8154-8155, 2006.

[35] M.-R. Huang, Y.-B. Ding, X.-G. Li, Y. Liu, K. Xi, C.-L. Gao*, et al.*, "Synthesis of semiconducting polymer microparticles as solid ionophore with abundant complexing sites for long-life Pb (II) sensors," *ACS applied materials & interfaces,* vol. 6, pp. 22096-22107, 2014.

[36] S. R. Prabakar, C. Sakthivel, and S. S. Narayanan, "Hg (II) immobilized MWCNT graphite electrode for the anodic stripping voltammetric determination of lead and cadmium," *Talanta,* vol. 85, pp. 290-297, 2011.

[37] J. Li, S. Guo, Y. Zhai, and E. Wang, "High-sensitivity determination of lead and cadmium based on the Nafion-graphene composite film," *Analytica chimica acta,* vol. 649, pp. 196-201, 2009.

[38] K. C. Armstrong, C. E. Tatum, R. N. Dansby-Sparks, J. Q. Chambers, and Z.-L. Xue, "Individual and simultaneous determination of lead, cadmium, and zinc by anodic stripping voltammetry at a bismuth bulk electrode," *Talanta,* vol. 82, pp. 675-680, 2010.

[39] J. Stauber and T. Florence, "The determination of trace metals in sweat by anodic stripping voltammetry," *Science of the Total Environment,* vol. 60, pp. 263-271, 1987.

[40] Z. Wang, G. Liu, L. Zhang, and H. Wang, "A bismuth modified hybrid binder carbon paste electrode for electrochemical stripping detection of trace heavy metals in soil," *Int. J. Electrochem. Sci,* vol. 7, pp. 12326-12339, 2012.

[41] C. Kokkinos, A. Economou, I. Raptis, and T. Speliotis, "Disposable lithographically fabricated bismuth microelectrode arrays for stripping voltammetric detection of trace metals," *Electrochemistry Communications,* vol. 13, pp. 391-395, 2011.

[42] G.-J. Lee, H.-M. Lee, and C.-K. Rhee, "Bismuth nano-powder electrode for trace analysis of heavy metals using anodic stripping voltammetry," *Electrochemistry Communications,* vol. 9, pp. 2514-2518, 2007.

[43] L. Zhu, L. Xu, B. Huang, N. Jia, L. Tan, and S. Yao, "Simultaneous determination of Cd (II) and Pb (II) using square wave anodic stripping voltammetry at a gold nanoparticle-graphene-cysteine composite modified bismuth film electrode," *Electrochimica Acta,* vol. 115, pp. 471-477, 2014.

[44] M. Mahmoudian, Y. Alias, W. Basirun, P. M. Woi, M. Sookhakian, and F. Jamali-Sheini, "Synthesis and characterization of Fe 3 O 4 rose like and spherical/reduced graphene oxide nanosheet composites for lead (II) sensor," *Electrochimica Acta,* vol. 169, pp. 126-133, 2015.

[45] P. M. Lee, Z. Chen, L. Li, and E. Liu, "Reduced graphene oxide decorated with tin nanoparticles through electrodeposition for simultaneous determination of trace heavy metals," *Electrochimica Acta,* vol. 174, pp. 207-214, 2015.

[46] S. Tang, P. Tong, X. You, W. Lu, J. Chen, G. Li*, et al.*, "Label free electrochemical sensor for Pb 2+ based on graphene oxide mediated deposition of silver nanoparticles," *Electrochimica Acta,* vol. 187, pp. 286-292, 2016.

[47] J. Zhuang, L. Fu, M. Xu, Q. Zhou, G. Chen, and D. Tang, "DNAzyme-based magneto-controlled electronic switch for picomolar detection of lead (II) coupling with DNA-based hybridization chain reaction," *Biosensors and Bioelectronics,* vol. 45, pp. 52-57, 2013.

[48] S. Tang, P. Tong, H. Li, J. Tang, and L. Zhang, "Ultrasensitive electrochemical detection of Pb 2+ based on rolling circle amplification and quantum dotstagging," *Biosensors and Bioelectronics,* vol. 42, pp. 608-611, 2013.

[49] R. Seenivasan, W.-J. Chang, and S. Gunasekaran, "Highly Sensitive Detection and Removal of Lead Ions in Water Using Cysteine-Functionalized Graphene Oxide/Polypyrrole Nanocomposite Film Electrode," *ACS applied materials & interfaces,* vol. 7, pp. 15935-15943, 2015.

[50] J.-T. Zhang, Z.-Y. Jin, W.-C. Li, W. Dong, and A.-H. Lu, "Graphene modified carbon nanosheets for electrochemical detection of Pb (II) in water," *Journal of Materials Chemistry A,* vol. 1, pp. 13139-13145, 2013.

[51] C. Gao, X.-Y. Yu, R.-X. Xu, J.-H. Liu, and X.-J. Huang, "AlOOH-reduced graphene oxide nanocomposites: one-pot hydrothermal synthesis and their enhanced electrochemical activity for heavy metal ions," *ACS applied materials & interfaces,* vol. 4, pp. 4672-4682, 2012.

[52] N. Promphet, P. Rattanarat, R. Rangkupan, O. Chailapakul, and N. Rodthongkum, "An electrochemical sensor based on graphene/polyaniline/polystyrene nanoporous fibers modified electrode for simultaneous determination of lead and cadmium," *Sensors and Actuators B: Chemical,* vol. 207, pp. 526-534, 2015.

[53] G. Aragay, J. Pons, and A. Merkoçi, "Recent trends in macro-, micro-, and nanomaterial-based tools and strategies for heavy-metal detection," *Chemical reviews,* vol. 111, pp. 3433-3458, 2011.

[54] D. Cai and M. Song, "Preparation of fully exfoliated graphite oxide nanoplatelets in organic solvents," *Journal of Materials Chemistry,* vol. 17, pp. 3678-3680, 2007.

[55] C. Gómez-Navarro, R. T. Weitz, A. M. Bittner, M. Scolari, A. Mews, M. Burghard*, et al.*, "Electronic transport properties of individual chemically reduced graphene oxide sheets," *Nano letters,* vol. 7, pp. 3499-3503, 2007.

[56] X. Wang, L. Zhi, and K. Müllen, "Transparent, conductive graphene electrodes for dye-sensitized solar cells," *Nano letters,* vol. 8, pp. 323-327, 2008.

[57] L. J. Cote, F. Kim, and J. Huang, "Langmuir− Blodgett assembly of graphite oxide single layers," *Journal of the American Chemical Society,* vol. 131, pp. 1043-1049, 2008.

[58] X. Li, G. Zhang, X. Bai, X. Sun, X. Wang, E. Wang*, et al.*, "Highly conducting graphene sheets and Langmuir–Blodgett films," *Nature nanotechnology,* vol. 3, pp. 538-542, 2008.

[59] G. Eda, G. Fanchini, and M. Chhowalla, "Large-area ultrathin films of reduced graphene oxide as a transparent and flexible electronic material," *Nature nanotechnology,* vol. 3, pp. 270-274, 2008.

[60] C. Mattevi, G. Eda, S. Agnoli, S. Miller, K. A. Mkhoyan, O. Celik*, et al.*, "Evolution of electrical, chemical, and structural properties of transparent and conducting chemically derived graphene thin films," *Advanced Functional Materials,* vol. 19, pp. 2577-2583, 2009.

[61] J. T. Robinson, M. Zalalutdinov, J. W. Baldwin, E. S. Snow, Z. Wei, P. Sheehan*, et al.*, "Wafer-scale reduced graphene oxide films for nanomechanical devices," *Nano letters,* vol. 8, pp. 3441-3445, 2008.

[62] J. T. Robinson, F. K. Perkins, E. S. Snow, Z. Wei, and P. E. Sheehan, "Reduced graphene oxide molecular sensors," *Nano letters,* vol. 8, pp. 3137-3140, 2008.

[63] S. Pang, H. N. Tsao, X. Feng, and K. Müllen, "Patterned Graphene Electrodes from Solution-Processed Graphite Oxide Films for Organic Field-Effect Transistors," *Advanced Materials,* vol. 21, pp. 3488-3491, 2009.

[64] Z. Wang, H. Wang, Z. Zhang, and G. Liu, "Electrochemical determination of lead and cadmium in rice by a disposable bismuth/electrochemically reduced graphene/ionic liquid composite modified screen-printed electrode," *Sensors and Actuators B: Chemical,* vol. 199, pp. 7-14, 2014.

[65] J.-M. Jian, Y.-Y. Liu, Y.-L. Zhang, X.-S. Guo, and Q. Cai, "Fast and sensitive detection of Pb2+ in foods using disposable screen-printed electrode modified by reduced graphene oxide," *Sensors,* vol. 13, pp. 13063-13075, 2013.

[66] H. Wan, Q. Sun, H. Li, F. Sun, N. Hu, and P. Wang, "Screen-printed gold electrode with gold nanoparticles modification for simultaneous electrochemical determination of lead and copper," *Sensors and Actuators B: Chemical,* vol. 209, pp. 336-342, 2015.

[67] R. O. Kadara and I. E. Tothill, "Development of disposable bulk-modified screen-printed electrode based on bismuth oxide for stripping chronopotentiometric analysis of lead (II) and cadmium (II) in soil and water samples," *Analytica chimica acta,* vol. 623, pp. 76-81, 2008.

[68] A. Mandil, L. Idrissi, and A. Amine, "Stripping voltammetric determination of mercury (II) and lead (II) using screen-printed electrodes modified with gold films, and metal ion preconcentration with thiol-modified magnetic particles," *Microchimica Acta,* vol. 170, pp. 299-305, 2010.

[69] M. Behbahani, P. G. Hassanlou, M. M. Amini, F. Omidi, A. Esrafili, M. Farzadkia*, et al.*, "Application of solvent-assisted dispersive solid phase extraction as a new, fast, simple and reliable preconcentration and trace detection of lead and cadmium ions in fruit and water samples," *Food chemistry,* vol. 187, pp. 82-88, 2015.

[70] M. Pourabadehei and C. N. Mulligan, "Selection of an appropriate management strategy for contaminated sediment: A case study at a shallow contaminated harbour in Quebec, Canada," *Environmental Pollution,* vol. 219, pp. 846-857, 2016.

[71] X. Xuan and J. Y. Park, "A miniaturized and flexible cadmium and lead ion detection sensor based on micro-patterned reduced graphene oxide/carbon nanotube/bismuth composite electrodes," *Sensors and Actuators B: Chemical,* vol. 255, pp. 1220-1227, 2018.

[72] S.-J. Choi, T.-H. Kwon, H. Im, D.-I. Moon, D. J. Baek, M.-L. Seol*, et al.*, "A polydimethylsiloxane (PDMS) sponge for the selective absorption of oil from water," *ACS applied materials & interfaces,* vol. 3, pp. 4552-4556, 2011.

[73] Y. Bonfil, M. Brand, and E. Kirowa-Eisner, "Characteristics of subtractive anodic stripping voltammetry of Pb and Cd at silver and gold electrodes," *Analytica chimica acta,* vol. 464, pp. 99-114, 2002.

[74] W. Gao, H. Y. Y. Nyein, Z. Shahpar, H. M. Fahad, K. Chen, S. Emaminejad*, et al.*, "A Wearable Microsensor Array for Multiplexed Heavy Metal Monitoring of Body Fluids," *ACS Sensors,* 2016.

[75] W. Su, M. Cho, J.-D. Nam, W.-S. Choe, and Y. Lee, "Highly sensitive electrochemical lead ion sensor harnessing peptide probe molecules on porous gold electrodes," *Biosensors and Bioelectronics,* vol. 48, pp. 263-269, 2013.

[76] P. M. Valencia, O. C. Farokhzad, R. Karnik, and R. Langer, "Microfluidic technologies for accelerating the clinical translation of nanoparticles," *Nature nanotechnology,* vol. 7, p. 623, 2012.

[77] T. W. Phillips, I. G. Lignos, and R. M. Maceiczyk, "Nanocrystal synthesis in microfluidic reactors: where next?," *Lab on a Chip,* vol. 14, pp. 3172-3180, 2014.

[78] C. Rivet, H. Lee, A. Hirsch, S. Hamilton, and H. Lu, "Microfluidics for medical diagnostics and biosensors," *Chemical Engineering Science,* vol. 66, pp. 1490-1507, 2011.

[79] X. Mao and T. J. Huang, "Microfluidic diagnostics for the developing world," *Lab on a Chip,* vol. 12, pp. 1412-1416, 2012.

[80] S. Lutz, P. Weber, M. Focke, B. Faltin, J. Hoffmann, C. Müller*, et al.*, "Microfluidic lab-on-a-foil for nucleic acid analysis based on isothermal recombinase polymerase amplification (RPA)," *Lab on a Chip,* vol. 10, pp. 887-893, 2010.

[81] H. Chen, X. Li, L. Wang, and P. C. Li, "A rotating microfluidic array chip for staining assays," *Talanta,* vol. 81, pp. 1203-1208, 2010.

[82] D. B. Weibel, M. Kruithof, S. Potenta, S. K. Sia, A. Lee, and G. M. Whitesides, "Torque-actuated valves for microfluidics," *Analytical chemistry,* vol. 77, pp. 4726-4733, 2005.

[83] S. E. Hulme, S. S. Shevkoplyas, and G. M. Whitesides, "Incorporation of prefabricated screw, pneumatic, and solenoid valves into microfluidic devices," *Lab on a Chip,* vol. 9, pp. 79-86, 2009.

[84] V. Studer, G. Hang, A. Pandolfi, M. Ortiz, W. French Anderson, and S. R. Quake, "Scaling properties of a low-actuation pressure microfluidic valve," *Journal of applied physics,* vol. 95, pp. 393-398, 2004.

[85] W. C. Jackson, H. D. Tran, M. J. O'Brien, E. Rabinovich, and G. P. Lopez, "Rapid prototyping of active microfluidic components based on magnetically modified elastomeric materials," *Journal of Vacuum Science & Technology B: Microelectronics and Nanometer Structures Processing, Measurement, and Phenomena,* vol. 19, pp. 596-599, 2001.

[86] A. V. Desai, J. D. Tice, C. A. Apblett, and P. J. Kenis, "Design considerations for electrostatic microvalves with applications in poly (dimethylsiloxane)-based microfluidics," *Lab on a Chip,* vol. 12, pp. 1078-1088, 2012.

[87] S. R. Sershen, G. A. Mensing, M. Ng, N. J. Halas, D. J. Beebe, and J. L. West, "Independent optical control of microfluidic valves formed from optomechanically responsive nanocomposite hydrogels," *Advanced Materials,* vol. 17, pp. 1366-1368, 2005.

[88] D. J. Beebe, J. S. Moore, J. M. Bauer, Q. Yu, R. H. Liu, C. Devadoss*, et al.*, "Functional hydrogel structures for autonomous flow control inside microfluidic channels," *Nature,* vol. 404, p. 588, 2000.

[89] H. Hartshorne, C. J. Backhouse, and W. E. Lee, "Ferrofluid-based microchip pump and valve," *Sensors and Actuators B: Chemical,* vol. 99, pp. 592-600, 2004.

[90] M. Kohl, D. Dittmann, E. Quandt, and B. Winzek, "Thin film shape memory microvalves with adjustable operation temperature," *Sensors and Actuators A: Physical,* vol. 83, pp. 214-219, 2000.

[91] M. A. Unger, H.-P. Chou, T. Thorsen, A. Scherer, and S. R. Quake, "Monolithic microfabricated valves and pumps by multilayer soft lithography," *Science,* vol. 288, pp. 113-116, 2000.

[92] L. Yobas, M. A. Huff, F. J. Lisy, and D. M. Durand, "A novel bulk micromachined electrostatic microvalve with a curved-compliant structure applicable for a pneumatic tactile display," *Journal of Microelectromechanical Systems,* vol. 10, pp. 187-196, 2001.

[93] M. M. Teymoori and E. Abbaspour-Sani, "Design and simulation of a novel electrostatic peristaltic micromachined pump for drug delivery applications," *Sensors and Actuators A: Physical,* vol. 117, pp. 222-229, 2005.

[94] M. Khoo and C. Liu, "Micro magnetic silicone elastomer membrane actuator," *Sensors and Actuators A: Physical,* vol. 89, pp. 259-266, 2001.

[95] N. Pamme, "Magnetism and microfluidics," *Lab on a Chip,* vol. 6, pp. 24-38, 2006.
[96] T. Pan, S. J. McDonald, E. M. Kai, and B. Ziaie, "A magnetically driven PDMS micropump with ball check-valves," *Journal of Micromechanics and Microengineering,* vol. 15, p. 1021, 2005.
[97] J. J. Nagel, G. Mikhail, H. Noh, and J. Koo, "Magnetically actuated micropumps using an Fe-PDMS composite membrane," in *Smart Structures and Materials 2006: Smart Electronics, MEMS, BioMEMS, and Nanotechnology*, 2006, p. 617213.
[98] M. Rahbar, S. Seyfollahi, A. Khosla, B. L. Gray, and L. Shannon, "Fabrication process for electromagnetic actuators compatible with polymer based microfluidic devices," *ECS Transactions,* vol. 41, pp. 7-17, 2012.
[99] F. N. Pirmoradi, L. Cheng, and M. Chiao, "A magnetic poly (dimethylesiloxane) composite membrane incorporated with uniformly dispersed, coated iron oxide nanoparticles," *Journal of Micromechanics and Microengineering,* vol. 20, p. 015032, 2009.
[100] C.-Y. Chen, C.-H. Chen, T.-Y. Tu, C.-M. Lin, and A. M. Wo, "Electrical isolation and characteristics of permanent magnet-actuated valves for PDMS microfluidics," *Lab on a Chip,* vol. 11, pp. 733-737, 2011.
[101] A. Gholizadeh and M. Javanmard, "Magnetically actuated microfluidic transistors: Miniaturized micro-valves using magnetorheological fluids integrated with elastomeric membranes," *Journal of Microelectromechanical Systems,* vol. 25, pp. 922-928, 2016.
[102] W. Wang, Z. Yao, J. C. Chen, and J. Fang, "Composite elastic magnet films with hard magnetic feature," *Journal of Micromechanics and Microengineering,* vol. 14, p. 1321, 2004.
[103] A. N. Knaian, "Electropermanent magnetic connectors and actuators: devices and their application in programmable matter," Massachusetts Institute of Technology, 2010.
[104] N. A. Shirazee and A. Basak, "Electropermanent suspension system for acquiring large air-gaps to suspend loads," *IEEE Transactions on magnetics,* vol. 31, pp. 4193-4195, 1995.
[105] A. N. Knaian, K. C. Cheung, M. B. Lobovsky, A. J. Oines, P. Schmidt-Neilsen, and N. A. Gershenfeld, "The Milli-Motein: A self-folding chain of programmable matter with a one centimeter module pitch," in *Intelligent Robots and Systems (IROS), 2012 IEEE/RSJ International Conference on*, 2012, pp. 1447-1453.
[106] J. I. Padovani, S. S. Jeffrey, and R. T. Howe, "Electropermanent magnet actuation for droplet ferromicrofluidics," *Technology,* vol. 4, pp. 110-119, 2016.
[107] D. K. Abeywardana, A. P. Hu, and Z. Salcic, "Pulse controlled microfluidic actuators with ultra low energy consumption," *Sensors and Actuators A: Physical,* vol. 263, pp. 8-22, 2017.
[108] R. J. Laumbach, H. M. Kipen, S. Ko, K. Kelly-McNeil, C. Cepeda, A. Pettit*, et al.*, "A controlled trial of acute effects of human exposure to traffic particles on pulmonary oxidative stress and heart rate variability," *Particle and fibre toxicology,* vol. 11, p. 45, 2014.
[109] W. S. Hummers Jr and R. E. Offeman, "Preparation of graphitic oxide," *Journal of the american chemical society,* vol. 80, pp. 1339-1339, 1958.

[110] G. K. Ramesha and S. Sampath, "Electrochemical reduction of oriented graphene oxide films: an in situ Raman spectroelectrochemical study," *The Journal of Physical Chemistry C,* vol. 113, pp. 7985-7989, 2009.

[111] V. C. Tung, M. J. Allen, Y. Yang, and R. B. Kaner, "High-throughput solution processing of large-scale graphene," *Nature nanotechnology,* vol. 4, p. 25, 2009.

[112] K. Kostikas, G. Papatheodorou, K. Ganas, K. Psathakis, P. Panagou, and S. Loukides, "pH in expired breath condensate of patients with inflammatory airway diseases," *American journal of respiratory and critical care medicine,* vol. 165, pp. 1364-1370, 2002.

[113] S. Hussain, R. Laumbach, J. Coleman, H. Youseff, K. Kelly-McNeil, P. Ohman-Strickland*, et al.*, "Controlled exposure to diesel exhaust causes increased nitrite in exhaled breath condensate among subjects with asthma," *Journal of occupational and environmental medicine/American College of Occupational and Environmental Medicine,* vol. 54, p. 1186, 2012.

[114] D. Zhang, Y. Fang, Z. Miao, M. Ma, X. Du, S. Takahashi*, et al.*, "Direct electrodeposion of reduced graphene oxide and dendritic copper nanoclusters on glassy carbon electrode for electrochemical detection of nitrite," *Electrochimica Acta,* vol. 107, pp. 656-663, 2013.

[115] L. Cui, J. Zhu, X. Meng, H. Yin, X. Pan, and S. Ai, "Controlled chitosan coated Prussian blue nanoparticles with the mixture of graphene nanosheets and carbon nanoshperes as a redox mediator for the electrochemical oxidation of nitrite," *Sensors and Actuators B: Chemical,* vol. 161, pp. 641-647, 2012.

[116] A. P. Pettit, H. Kipen, R. Laumbach, P. Ohman-Strickland, K. Kelly-McNeill, C. Cepeda*, et al.*, "Disrupted nitric oxide metabolism from type II diabetes and acute exposure to particulate air pollution," *PloS one,* vol. 10, p. e0144250, 2015.

[117] A. T. Mubarak, A. A. Mohamed, K. F. Fawy, and A. S. Al-Shihry, "A novel kinetic determination of nitrite based on the perphenazine-bromate redox reaction," *Microchimica Acta,* vol. 157, pp. 99-105, 2007.

[118] X.-F. Yue, Z.-Q. Zhang, and H.-T. Yan, "Flow injection catalytic spectrophotometric simultaneous determination of nitrite and nitrate," *Talanta,* vol. 62, pp. 97-101, 2004.

[119] A. A. Ensafi and A. Kazemzadeh, "Simultaneous determination of nitrite and nitrate in various samples using flow injection with spectrophotometric detection," *Analytica chimica acta,* vol. 382, pp. 15-21, 1999.

[120] Y. Kanda and M. Taira, "Flow-injection analysis method for the determination of nitrite and nitrate in natural water samples using a chemiluminescence NOx monitor," *Analytical sciences,* vol. 19, pp. 695-699, 2003.

[121] Q. Yue and Z. Song, "Assay of femtogram level nitrite in human urine using luminol–myoglobin chemiluminescence," *Microchemical journal,* vol. 84, pp. 10-13, 2006.

[122] Z. Lin, W. Xue, H. Chen, and J.-M. Lin, "Peroxynitrous-acid-induced chemiluminescence of fluorescent carbon dots for nitrite sensing," *Analytical chemistry,* vol. 83, pp. 8245-8251, 2011.

[123] K. Zhao, H. Song, S. Zhuang, L. Dai, P. He, and Y. Fang, "Determination of nitrite with the electrocatalytic property to the oxidation of nitrite on thionine modified

aligned carbon nanotubes," *Electrochemistry Communications,* vol. 9, pp. 65-70, 2007.

[124] Y. Cui, C. Yang, W. Zeng, M. Oyama, W. Pu, and J. Zhang, "Electrochemical determination of nitrite using a gold nanoparticles-modified glassy carbon electrode prepared by the seed-mediated growth technique," *Analytical Sciences,* vol. 23, pp. 1421-1425, 2007.

[125] N. Zhu, Q. Xu, S. Li, and H. Gao, "Electrochemical determination of nitrite based on poly (amidoamine) dendrimer-modified carbon nanotubes for nitrite oxidation," *Electrochemistry Communications,* vol. 11, pp. 2308-2311, 2009.

[126] H. Li, C. J. Meininger, and G. Wu, "Rapid determination of nitrite by reversed-phase high-performance liquid chromatography with fluorescence detection," *Journal of Chromatography B: Biomedical Sciences and Applications,* vol. 746, pp. 199-207, 2000.

[127] Y. Zuo, C. Wang, and T. Van, "Simultaneous determination of nitrite and nitrate in dew, rain, snow and lake water samples by ion-pair high-performance liquid chromatography," *Talanta,* vol. 70, pp. 281-285, 2006.

[128] H. Kodamatani, S. Yamazaki, K. Saito, T. Tomiyasu, and Y. Komatsu, "Selective determination method for measurement of nitrite and nitrate in water samples using high-performance liquid chromatography with post-column photochemical reaction and chemiluminescence detection," *Journal of Chromatography A,* vol. 1216, pp. 3163-3167, 2009.

[129] N. Öztekin, M. S. Nutku, and F. B. Erim, "Simultaneous determination of nitrite and nitrate in meat products and vegetables by capillary electrophoresis," *Food chemistry,* vol. 76, pp. 103-106, 2002.

[130] X. Wang, E. Adams, and A. Van Schepdael, "A fast and sensitive method for the determination of nitrite in human plasma by capillary electrophoresis with fluorescence detection," *Talanta,* vol. 97, pp. 142-144, 2012.

[131] R. Kikura-Hanajiri, R. S. Martin, and S. M. Lunte, "Indirect measurement of nitric oxide production by monitoring nitrate and nitrite using microchip electrophoresis with electrochemical detection," *Analytical chemistry,* vol. 74, pp. 6370-6377, 2002.

[132] V. C. Tung, M. J. Allen, Y. Yang, and R. B. Kaner, "High-throughput solution processing of large-scale graphene," *Nature nanotechnology,* vol. 4, pp. 25-29, 2009.

[133] D. A. Brownson, S. A. Varey, F. Hussain, S. J. Haigh, and C. E. Banks, "Electrochemical properties of CVD grown pristine graphene: monolayer-vs. quasi-graphene," *Nanoscale,* vol. 6, pp. 1607-1621, 2014.

[134] T. V. Jayaraman, "Effect of processing of HIPERCO® 50 alloy laminates on their magnetic properties," *Journal of Electronic Materials,* vol. 44, pp. 4379-4386, 2015.